Revisiting the Turkevich Synthesis and Established New Routes to Colloidal Gold & Gold-Silver Nanoparticles

Madeeha Akram Uppal

Supervised by Professor Ivan P. Parkin

Abstract

The use of gold and silver nanoparticles has experienced a renaissance over the last 10 years and their number of uses in a variety of commercial products has dramatically increased. The first chapter of this thesis addresses the current and future uses of gold and silver nanoparticles, the methods employed in synthesising them and the theory behind their fascinating surface plasmon resonance properties.

For the remainder of this thesis we will revisit one of the most common methods for growing gold nanoparticles, the Turkevich method, and then experimentally modify this method as our basis for growing gold nanoparticles in various ways. The second chapter deals with the slow decrease in average particle size observed in gold colloids grown by the Turkevich method where we establish why this occurs based on the nanoparticle formation mechanism. In the third chapter we investigate the effect of changing reagent concentration and activation method (thermal heating, microwave-assisted heating, ultra-violet light and sonication) on the average particle size. In the fourth chapter we investigate the effect of replacing the tri-sodium citrate reducing agent used in the Turkevich method with various ketones. In the fifth chapter we investigate how the Turkevich method can be used to grow primarily silver-gold core-shell particles a one-step and how these particles interact with methylene blue dye. In the sixth chapter we investigate a two-step route to gold-silver core-shell particles by employing gold “seeds” grown by the Turkevich method and the subsequent effect of using ascorbic acid as a co-reducing agent alongside tri-sodium citrate.

Declaration

I, Madeeha Akram Uppal, confirm the work presented in this thesis as my own. Where information has been derived from other sources, I confirm that this has been indicated in this thesis.

Dedication

I would like to dedicate this work to my supervisor, Prof. Ivan Parkin, for his continued support and guidance. I would also like to thank my secondary supervisor, Prof. Mike Ewing, for his support and advice as well as my fellow researchers I worked alongside over the years, including my husband Andreas for showing me the ropes around the laboratory when I first embarked on my research journey. I would like to thank Dr. Steve Firth for his diligent help with transmission electron microscopy at UCL, Dr. Teck Lim and the Oxford team for their help with the high resolution transmission electron microscopy studies at Oxford University, Mr. Kevin Reeves for his help with scanning electron microscopy studies at UCL and Dr. Abil Aliev for his help with nuclear magnetic resonance imaging studies at UCL.

I would like to thank my parents for their love and support. I would like to extend my love and affection to Zeynab, the joy of my life.

Table of contents

1. Introduction

This thesis presents new routes for synthesising gold, silver and gold-silver/ silver-gold core-shell nanoparticles. Through investigating new pathways of forming gold and gold-silver core-shell nanoparticles we hope to gain further control of the size and shape distribution of the colloid formed and also open the door to greener and more efficient syntheses that can be tailored to their current and future applications.

1.1. Current and future uses of gold and silver nanoparticles

The use of gold and silver nanoparticles has experienced a resurgence over the last 15 years and their number of uses in a variety of commercial products has dramatically increased.[1] Given their bio-compatibility, gold nanoparticles have been used primarily as contrast agents in the imaging of biological assays.[2] They have also been applied in home pregnancy test kits under the brand *Clearblue*™ in which a thin-film of gold nanoparticles clump together and turn pink upon exposure to specific hormones that are present during pregnanancy.[3] Such thin-films of gold nanoparticles are also used to detect lone molecules and DNA in forensic analysis by surface enhanced Raman spectroscopy (SERS).[4,5] However, the two most promising future uses of gold nanoparticles in catalysis are yet to be commercialised. One promising use is in early stage cancer detection. Gold nanoparticles that are bound to cancer-specific antigens preferentially attach themselves to cancerous cells, enhancing their detectability by several orders of magnitude compared with current commercial immunoassays.[6] In addition, the gold nanoparticles efficiently convert light into localised heat, which can be exploited for selective laser photo-thermal therapy of cancer.[1] Another promising use of gold nanoparticles is in low temperature heterogeneous catalysis for the selective oxidation of numerous organic species.[7] Given the large surface area per unit volume of such nanoparticle catalysts, economical levels of gold can effectively catalyse such reactions. In one case they have been shown to catalyse the room temperature formation of carbon dioxide from carbon monoxide (CO) when supported on mesoporous silica.[8] This promises future applications in breathing apparatus, air cleaning devices and catalytic converters that remove poisonous CO gas ejections[9] as well as in methanolic fuel cell devices that inhibit the catalytic poisoning of the anodes by preferential CO adsorption.[10] In another case gold nanoparticles have been shown to act as tuneable active catalysts for efficiently oxidising olefins to epoxides in air, without the need for any sacrificial reductants.[11] With the exception of ethene, such epoxide formation reactions require harsh oxidising agents such as hydrogen peroxide, however, it is predicted that gold nanoparticles will replace these harsh chemicals in future and provide a greener route for the mass-production of epoxide groups, an important stepping stone in many pharmaceutical processes. Several alternative future applications of gold nanoparticles have also been suggested. One such application is within semiconductor thin-films for improving their optical[12,13] and functional properties.[14] Another application is in the lethal photo-sensitisation of bacteria, where the activity of photo-sensitising agents such as toluidine blue has been shown to increase dramatically when linked to gold nanoparticle light mediators.[15–17] The potential use of gold nanoparticles in targeted drug delivery[18] or the rapid colorimetric detection of toxins such as cholera[19] have also been demonstrated.

Silver nanoparticles have been applied in single molecule and DNA detection[20,21] and are commonly found medicinal application.[22] This is primarily due to their oligodynamic anti-bacterial and anti-fungal properties[23] and has been most prominently applied in topical wound dressings.[24] For similar reasons they have also been commercially applied in deodorants and anti-microbial sprays[25] as well as surface coating technologies such as *Silver Nano*.[26] With their intense light absorbing properties combined with their high susceptibility to reversible oxidation and reduction, silver nanoparticle technology has also been applied in photo-chromic glass lenses.[27] When silver chloride ions are dispersed throughout the lens, exposure to harmful UV light causes the chloride ions to release electrons, reducing the silver (I) ions present to silver metal that then cluster to form silver nanoparticles. This reduces the level of UV that can be transmitted through the lens and protects the eye from UV damage. An extension of this technology, multi-colour photochromism, was recently demonstrated by loading silver nanoparticles of highly distributed size and shape onto a titania support.[28] Upon exposure to particular portions of visible light, the silver particles of the corresponding size range absorb the light, oxidise and become transparent to this light, thus making the film identical in colour to the incident light to which it was exposed. Upon exposure to UV light, the titania support photo-generates electrons that reduce any oxidised nanoparticles back to their original coloured state. Such reversible colour changes have potential applications in smart windows and displays, re-writable colour copy paper and multi-wavelength optical memory devices.[29] In addition to this, silver nanoparticles have also been incorporated within metal oxide composite thin-films to improve the material's optical and functional properties.[30]

1.2. The surface plasmon resonance properties of gold and silver nanoparticles

The applications of gold and silver nanoparticles have principally been driven by their intense and tuneable surface plasmon resonance (SPR) properties.[31] The physical origin of the strong light absorption occurs when all free conduction band electrons coherently oscillate when interacting with an electromagnetic field (Figure 1.2.1). This resonance condition occurs when the frequency of incident light matches the natural frequency of surface electrons against the restoring

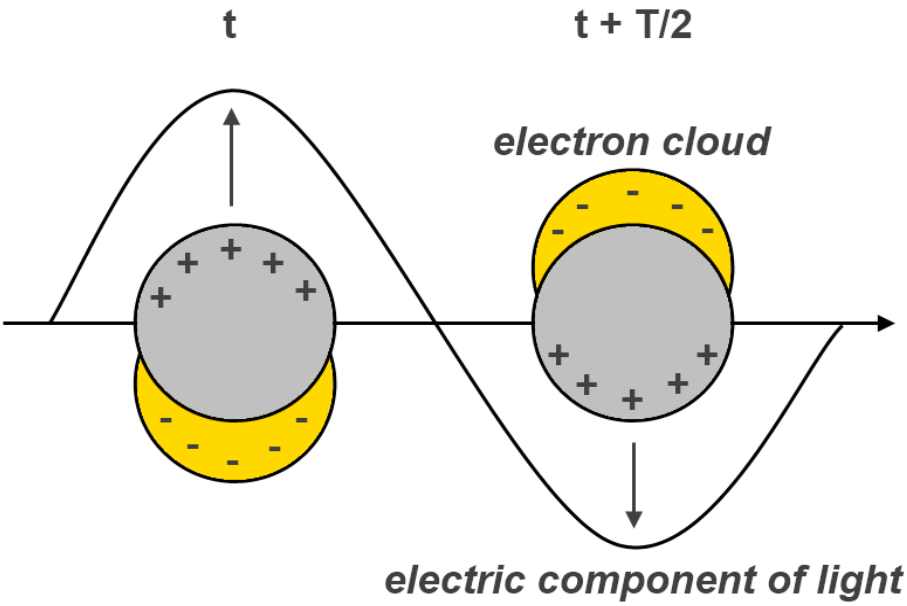

Figure 1.2.1: The interaction of spherical noble metal particles with an electric field at the resonance condition where the frequency of light matches the natural frequency of surface electrons in balance with the restoring force of positive nuclei. This induces a dipolar oscillation of the conduction band electrons with period T, causing surface plasmons to propagate in a direction parallel to the particle-solution interface. This effect is known as the surface plasmon resonance.

force of positive nuclei. In this manner a periodic dipolar oscillation (T) of the free electrons is formed.

The surface plasmons that are generated propagate in a direction parallel to the particle-solution interface. These oscillations are very sensitive to any change at this boundary, like the surface adsorption of molecules or a change in medium *i.e.* replacing the solvent in which the colloid is dispersed. Such changes form the basis of surface enhanced Raman spectroscopy (SERS), where the electric field enhancement at the surface of the nanoparticle magnifies the intensity of incident light which will excite the Raman modes of the loaded molecules being studied. This in turn increases the signal of the Raman scattering.[32]

By solving Maxwell's equations for a radiation field interacting with a spherical metal particle under the appropriate boundary conditions, Mie was the first to provide an exact solution for the strong absorption band observed in spherical gold colloids.[33] The solution leads to a series of multipole oscillations for the extinction cross-section of the nanoparticles.[34] Through a series expansion of the involved fields into partial waves, the following expressions for the extinction cross-section (σ_{ext}) and scattering cross-section (σ_{sca}) are obtained:[35]

$$\sigma_{ext} = \frac{2\pi}{|k|^2}\sum_{L=1}^{\infty}(2L+1)Re(a_L + b_L) \tag{1.1}$$

$$\sigma_{sca} = \frac{2\pi}{|k|^2}\sum_{L=1}^{\infty}(2L+1)(|a_L|^2 + |b_L|^2) \tag{1.2}$$

where

$$a_L = \frac{m\psi_L(mx).\psi_L'(x) - \psi_L'(mx).\psi_L(x)}{m\psi_L(mx).\eta_L'(x) - \psi_L'(mx).\eta_L(x)} \qquad b_L = \frac{\psi_L(mx).\psi_L'(x) - m\psi_L'(mx).\psi_L(x)}{\psi_L(mx).\eta_L'(x) - m\psi_L'(mx).\eta_L(x)}$$

Re spans only the real axis, $m = n/n_m$ where n and n_m are the complex and real parts of the refractive index of the nanoparticle and the medium respectively, $x = |k|r$ where k is the wave-vector and r the radius of the nanoparticle, ψ_L and η_L are the Riccati-Bessel cylindrical functions[36] and ψ_L' and η_L' the respective differentials and L is the summation index of the partial waves where L = 1 corresponds to the dipole oscillation as illustrated in Figure 1.2.1 while L = 2 is the quadrupole oscillation and so on.

The absorption cross-section $\sigma_{abs}$of the nanoparticle is simply derived from the following relationship:

$$\sigma_{abs} = \sigma_{ext} - \sigma_{sca} \tag{1.3}$$

For particles much smaller than the wavelength of light ($2r \ll \lambda$) only the dipole oscillation contributes significantly to the extinction cross-section and the Mie relationship can be reduced to contain solely the L = 1 term.[37] However, for larger nanoparticles that are typically 20 nm or greater in diameter, such is often the case with gold or silver colloids, the dipole approximation breaks down and the plasmon resonance depends explicitly on the particle size and dielectric medium. This is due to higher order modes (L > 1) becoming observable. As these modes require lower energy to be excited the centre of the plasmon band red-shifts with increasing particle size.

For any monodisperse colloid, the plasmon band width is primarily associated with the relaxation time of the coherent electron oscillation.[38] Larger band widths correspond to more rapid losses of the coherent electron motion. Such relaxation times are of the order of a few femtoseconds and strongly suggest that the process is due to electron – electron collisions.[39] For increasingly smaller particles the plasmon oscillation becomes increasingly broad and weak. Where particles become less than about 2 nm in diameter the surface plasmon band typically disappears altogether.[40] This is due to the number of free electrons in the “conduction” band becoming very small where the assumption that bulk-like electronic bands and optical properties associated with the electronic structure of the nanoparticles becomes questionable. In particular, the use of the bulk dielectric constant which enters the Mie equation (1.1 and 1.2) cannot be justified any longer. Reducing the size of the nanoparticle has a pronounced effect on the energy level spacing as the system becomes more confined.[41] Similar to a particle in a box, the energy separation between adjacent levels increases with decreasing dimensions. This is most pronounced for semiconductor nanoparticles where the bandgap energy increases with decreasing size and the onset of the bandgap transition is shifted to higher frequencies.[42] These quantum size effects become apparent in metallic nanoparticles when the spacing of intra-band transitions within the conduction band exceeds the thermal energy (about 26 meV). This generally coincides with the size region where the surface plasmon band is lost ($N \approx 100$ and below ≈ 2 nm in diameter).[43]

As silver and gold share near identical crystal packing[5] they readily form core-shelled colloids.[44] When the level of each metal is controlled, the optical properties of the resulting colloid can be tuned to specific wavelengths.[45] Such an exploitation of the surface plasmon resonance band has been explored for uses as optical filters,[46] photon energy transport devices,[47] more wavelength specific active surfaces for surface-enhanced Raman spectroscopy,[48] fluorescence scatterers,[49] chemical/ biological sensors[50] and catalysts.[51,52] Core-shell combinations that expose silver at the surface have even demonstrated enhanced anti-bacterial activity.[53] Therefore, by studying the various shapes and sizes of gold-silver core-shell particles and its effect on the surface plasmon resonance properties, one can tailor colloids to a specified function.

1.3. Current gold and silver nanoparticle synthetic methods

The global value of the gold nanoparticle industry was more than $204.6 million in 2006 with the expectation of steadily increasing growth.[54] As the industry continues to expand, finding “greener” and more cost efficient ways of mass-producing gold colloids as well as acquiring a better understanding of the mechanisms by which they form is of growing commercial importance.

A vast range of techniques have been used to produce gold and silver nanoparticles where preparation methods range from chemical methods to metal vapour synthesis.[55] Common to each method is the presence of some protective capping agent, generally in the form of a polymer or surfactant, which stabilise the nanoparticles that form. This allows the kinetically favoured product to form (nanoparticles) and inhibits the colloid from reaching its thermodynamically favoured state, which would eventually form the bulk metal if given enough time.

One typical synthetic method involves the use of sonolysis.[56] In the general case, a metal salt is dissolved in a suitable liquid medium in addition to a suitable reducing and/ or capping agent (as some reagents can act as both the reducing and capping agent). By propagating sonic waves throughout a liquid medium acoustic cavities form that lead to the implosive collapse of bubbles. When these bubbles collapse, a large amount of kinetic energy is released and converted to highly localised heat. As the compression of these bubbles during cavitation is more rapid than thermal transport the localised hot-spots are short-lived.[57] At these hot-spots the activation energy barrier for the reduction of the metal ions can be surpassed, which leads to the eventual formation of metal atoms that nucleate and grow. At the latter stages of nanoparticle growth an optimum size is reached that can depend strongly on the nature and concentration of the capping agent used. A similar method that is often used to form colloidal gold and silver involves the use of microwave radiation.[58,59] Quite analogous to sonolysis, localised pockets of heat form through the dielectric heating of a polar liquid medium in which the metal salt reductant and capping agents are housed. An alternative method involves the use of high energy radiation such as ultra-violet,[60,61] X-ray[62] and gamma radiation.[63] This method employs the use of free electrons and/ or radicals generated in solution through radiolysis to induce the reduction of metal salts and nanoparticle growth. A twist of this method involves using high powered light in the form of a laser to ablate a submerged metal target, releasing metal ions into solution that nucleate and grow and become encapsulated by a stabilising capping agent.[64,65] Other methods of forming metal colloids include electrolysis[66] and metal vapour synthesis.[67] In order to synthesise nanoparticles of particular shape and size the reduction of metal precursors can be conducted in constrained media such as zeolite cavities,[68] porous alumina[69] and micelles.[70] However, shape and size directing reducing and capping agents are more often employed to achieve this. A more modern emerging theme in gold and silver nanoparticle formation is green chemistry, where naturally occurring reducing agents are being more frequently used to induce nanoparticle growth such as yeasts,[71] proteins,[72] fruit[73] and plant extracts.[74]

The two most commonly applied methods in the formation of gold nanoparticles are the Brust–Schiffrin[75] and Turkevich method.[76,77] The Brust–Schiffrin method is generally used when nanoparticles of the order of 5 – 6 nm in diameter are required that are dispersed in an immiscible organic liquid medium such as toluene. This is achieved by reducing a metal salt (such as auric acid for gold nanoparticle formation or silver nitrate for silver nanoparticle formation) with sodium borohydride in the presence of a capping agent such as tetraoctylammonium bromide (TOAB). Nevertheless the most widely used method for forming gold nanoparticles is the Turkevich method.[77] This method involves the thermally aided reduction of auric acid with tri-sodium citrate in water, which acts as both the reducing and capping agent. Depending on the gold/ citrate concentration the resulting colloid produces nanoparticles with an average diameter of ≈ 10 – 30 nm in size with excellent reproducibility. A typical reaction conducted in boiling water proceeds in less than 10 mins. The mechanism by which these primarily spherical particles form has been well studied by various groups.[76,78,79]

The original studies conducted by Turkevich *et. al.* showed the nucleation of gold nanoparticles proceeds through four stages: (i) a slow induction period, (ii) a short and rapid nucleation stage followed by (iii) a slow and more constant linear nucleation stage finished up by (iv) a decay portion.[77] These nucleation stages coincide with incredibly varied changes in solution colour, changing from colourless to black and then purple during the rapid nucleation stage that is followed by a sharp transition from blue to deep red during the slow nucleation stage that continues to deepen in colour up to a maximum point.

It was clear from the overall reaction that Au^{3+} ions from auric acid were reduced to metallic Au^0 that nucleated to form gold nanoparticles. On the other hand, through investigating the chemistry of the tri-sodium citrate reducing agent it was observed that its oxidation product yields acetone dicarboxylic acid:

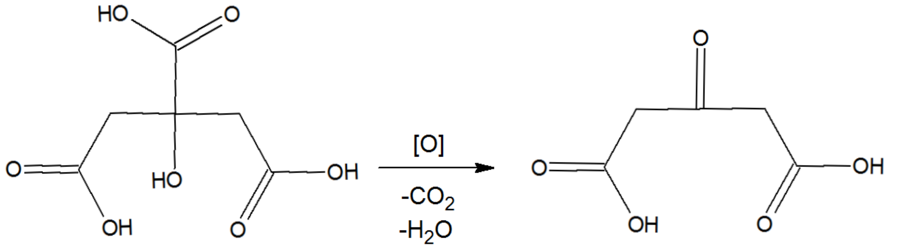

(1.4)

In replacing tri-sodium citrate for acetone dicarboxylic acid from the outset, the nanoparticle formation reaction proceeds without a slow induction period. It was thus proposed that the formation of acetone dicarboxylic acid is the first intermediate step by which the nanoparticle formation reaction may proceed. Further oxidations of acetone dicarboxylic acid formed formic acid and formaldehyde by-products.

Using both UV-visible spectroscopy and transmission electron microscopy (TEM) Chow *et. al.* monitored the nanoparticle formation reaction *in situ*.[79] They observed an initial plasmon band form in the red region (λ_{max} = 590 nm) during the rapid nucleation stage. This plasmon band steadily blue shifted over the course of the linear nucleation period whilst also increasing in intensity to a final value of (λ_{max} = 525 nm). In accordance with Mie theory,[35] this corresponded to the initial large formation of gold clusters (≈ 100 nm in diameter) that decreased in size to a uniform colloid (≈ 20 nm in diameter). TEM imaging of solution aliquots that were removed periodically from the solution during the nanoparticle formation reaction confirmed spectroscopic observations. During the rapid nucleation stage, large multi-core particles (100 – 150 nm) composed of smaller particle clusters (5 –

15 nm) were observed. These particles gradually broke apart during the linear nucleation period, decreasing in size to a monodisperse spherical colloid, 15 nm in diameter.

Through iodometric titrations it was observed that the critical tipping point where the large multi-core particles collapse corresponds to:

$$[Au^{3+}]/\,[Au^{0}]\ < 0.7 \qquad (1.5)$$

That is, the reaction accelerates when 30 % of the initial auric acid is consumed. At this point the solution suddenly turns from purple to deep red and is followed by a rapid increase in the number of smaller particles. It was therefore summarised that the nanoparticle formation mechanism proceeds by the initial reduction of Au^{3+} to Au^{0} by acetone dicarboxylic acid. Through atomic force microscopy studies it was observed that these Au^{0} atoms preferentially absorb to free auric acid and form Au^{0} clusters. Due to their low surface potential, these surface clusters aggregate and form large multi-core structures. As the auric acid to which these clusters are bound is eventually consumed, the surface potential grows to a point where the electrostatic repulsive forces drive particles out of the shallow minimum. This causes the large particles to break apart into smaller particles and the eventual formation of a uniform colloid. By performing this reaction at various temperatures the activation energy was determined ($E_a \approx 70 \pm 5$ kJ mol^{-1}). The Turkevich method for gold nanoparticle growth has been more recently studied using time-resolved methods including Small-angle X-ray scattering (SAXS) and X-ray absorption near edge structure (XANES).[80] Using these techniques, Polte *et. al.* showed how the reaction proceeded through a four step process: (i) nucleation, (ii) aggregation, (iii) slow further growth and (iv) fast final growth. Interestingly, the large multi-core structures observed by Chow *et. al.*,[79] where not observed by Polte *et. al.* This is because SAXS could only see the average gold particle crystal size and not how these small crystals aggregated. Of note, time-resolved methods showed that a similar particle growth process is observed using the Brust–Schiffrin[75] method, where the first step involves a rapid conversion of the ionic gold precursor into metallic gold nuclei followed by particle growth via coalescence of smaller entities.[81] Of note, one must also consider the pH of the nanoparticle solution when trying to understand how the reaction will proceed. For instance, Polte *et. al.* found a pH-dependent equilibrium of the formation of $AuCl_{4-x}(OH)_x$ complexes. At concentrations typical for most nanoparticle syntheses (*i.e.* below 1 mM), the pH is above 3. Therefore, other gold complexes will be present, such as $AuCl_3(OH)^-$.[82]

In the second chapter of this thesis we revisit the Turkevich method, which is the most common thermal route to forming gold nanoparticles. Although the mechanism by which a gold colloid is formed by the Turkevich method has been well established on the minutes to hours timescale,[78,79,83] the change in nanoparticle size over an extended period of storage from days to weeks has not been investigated. In this chapter we show how over an extended period of storage digestive ripening, which is effectively the inverse of Ostwald ripening, smaller particles grow at expense of the larger ones. Taking the concept of revisiting the Turkevich method further, in Chapter 3 we then demonstrate a systematic study of the effect of the type of energy used to initiate and propagate the reaction; where sonolysis, microwave and ultra-violet radiations were investigated. Moving away from the use of the tri-sodium citrate surfactant used in the Turkevich method we then studied a range of ketones and their function as both reducing and capping agents in the synthesis of colloidal gold in Chapter 4. This led to the discovery of a new room temperature self-activated synthesis of colloidal gold using cyclohexanone, where the mechanism was also established (Section 4.3). The microwave-induced reflux of common ketone alternatives was also studied (Section 4.4). Lastly, novel methods to gold-silver/ silver-gold core-shell were investigated in Chapter 5. A one-pot synthesis, analogous to the Turkevich method, led to primarily silver cored gold coated core-shell nanoparticles, where their interactions with methylene blue dye and optimum synergic light capture was studied (Section 5.3). For gold core silver shell colloids a two-step seed mediated route was investigated, where the synthesis was similar to the Turkevich method but the effect of the addition of ascorbic acid was studied (Section 5.4).

2. The extended time evolution size decrease of gold nanoparticles formed by the Turkevich method

2.1. Overview

This chapter reports on how gold nanoparticle solutions were synthesised by the Turkevich reduction method and stored in either the light or dark. All solutions were monitored on a daily basis using UV-visible absorption spectroscopy and showed surface plasmon resonance (SPR), typical of gold nanoparticle colloids. Over time, an increase in SPR intensity, a narrowing of the SPR peak and a gradual shift towards lower wavelengths were observed. This was indicative of a decrease in average nanoparticle size and the formation of a more mono-dispersed colloid. After two weeks of storage no further changes were observed by UV-visible absorption spectroscopy. A series of transmission electron micrographs (TEM) taken during this period confirmed that the plasmon resonance shifts were due to a decrease in particle size. This systematic size decrease was also observed in solutions that were centrifuged straight after the reaction to remove any excess/ unreacted tri-sodium citrate surfactant and auric acid gold source. This decreased the likelihood of the size decrease being due to an extended reaction of any remnant auric acid and surfactant that were yet to react. The gold nanoparticle evolution followed an inverse Ostwald type growth, where the size of nanoparticles decrease, an effect also known as "digestive ripening". The aging process provides a reliable route to fairly mono-dispersed gold nanoparticles of *ca* 11.5 – 12.5 nm in size *via* the Turkevich method.

2.2. Introduction

The synthesis of gold nanoparticles formed by the Turkevich reaction has previously been monitored by *in situ* UV-visible spectroscopy and transmission electron microscopy (TEM) methods in tandem.[84,85] The inter-relationship between the SPR peak and average nanoparticle diameter was derived. The reaction kinetics of gold nanoparticle formation using this method was also investigated by Kimling *et. al.* for a range of reagent concentrations.[76] The reaction was monitored by UV-visible absorption spectroscopy *in situ* where the nanoparticle diameters were predicted by Mie theory.[38] These were found to be in strong agreement with nanoparticle diameters determined using X-ray diffraction. An Ostwald ripening[83] type growth was observed, whereby particles increased in size during the reaction and levelled out at a maximum size – the whole process spanning a 50 second period. Rodriguez-Gonzalez *et. al.* also synthesised gold nanoparticles using the Turkevich method, where solutions were heated more slowly allowing for a slower reaction that was progressively monitored by UV-visible spectroscopy, electrochemistry and by TEM using sample aliquots.[78,79] The reaction took approximately 12 hours to complete, after 1 minute, large nanoparticle clusters (*ca.* 100 nm) composed of smaller particles (5 – 10 nm) initially formed. A sharp increase in the conductivity after 10 hours of heating led to the formation of nanoparticles *ca.* 15 nm in size, coupled with a shift in the SPR band to higher energy. Similar to Chow and Zukoski's conclusions on the mechanism of gold nanoparticle formation from the Turkevich method, it was surmised that in the early stages of the reduction reaction only a fraction of the gold salt was consumed and that a complex was formed between gold chloride and citrate/citrate oxidation products.[78] The absorption of $AuCl_4$ on the large clusters that formed led to a reversible aggregation, resulting in a progressive increase in the surface potential. An accelerated loss of $AuCl_4$ was seen when the $[AuCl_4]$: $[Au_0]$ ratio reached 0.7, corresponding to a rapid change in the solution colour from light purple to red, and a rapid decrease in size of the large clusters particles seen by TEM.[79] It is recognized that citrate formed Au nanoparticles are water stable for long periods of time—years in fact; however it is not documented whether changes in particle size, distribution or concentration occur in such solution solutions. Previous time evolution studies of Au nanoparticles formed in various ways have focused solely on smaller time-scales of up to a few hours.[86–88] The phenomenon of an average particle size decrease is uncommon as it opposes reductions in interfacial free energy gained by the particle from increased size.[89] However, by refluxing polydisperse Au nanoparticle solutions in the presence of surface active ligands, Prasad *et. al.* observed such a phenomenon, with an overall reduction in nanoparticle size and a conversion to monodispersity.[90–92] This inverse Ostwald ripening process, termed digestive ripening,[93] occurred over a 90 minute period of reflux.

In this chapter we present an analysis of the extended time evolution of citrate formed Au nanoparticles stored in both light and dark. By monitoring the change in SPR band shift coupled with TEM imagery, it was found that nanoparticle sizes slowly decreased from their Ostwald ripened maxima and levelled out over subsequent days of standing, regardless of being stored in the light or dark, with a decrease in average size from *ca.* 15 to 12 nm. A time evolution narrowing of the particle size distribution from the tightening of SPR bands as well as dynamic light scattering measurements was seen. Notably we show after removing the free citrate and auric acid from the solution when still purple in colour (*i.e.* the early stages of the reaction) the nanoparticles still reduce in size, forming a red solution. We believe that interactions between the larger particles that initially form can lead to the eventual re-ordering and formation of a smaller monodisperse colloid. This phenomenon of inverse-Ostwald growth can be described as digestive ripening. TEM imagery not only showed an overall decrease in particle size but also showed a narrowing of the size distribution.

2.3. Experimental

2.3.1. Synthesis

All glassware was washed with aqua regia ($3HCl : 1HNO_3$) and rinsed with copious amounts of deionised water. Stock solutions labelled X and Y were made up; solution X consisting of $HAuCl_4.3H_2O$ (170 mg) dissolved in 100 mL deionised water (5 mM) and solution Y consisting of $Na_3C_6H_5O_7$-$2H_2O$ (250 mg) dissolved in 50 mL deionised water (20 mM). A 1 mL aliquot of solution X was dissolved in 18 mL of deionised water and uniformly heated in an oil bath with constant stirring. When the solution began to boil, 1 mL of solution Y was allowed to fall drop wise through a frit over a period of 6 min. After a characteristic colour change to lilac was observed the solution was removed from the oil bath and allowed to cool to room temperature whilst being stirred. Solutions were not refluxed as this encouraged rapid digestive ripening of the colloid, pushing the reaction and evolution to completion before a thorough analysis of the phenomenon could be studied. Five repeat Au nanoparticle solutions were synthesized in this manner, labelled Solutions A – E.

2.3.2. Analysis

Solutions A – D were divided into two portions: one was stored in the light and the other in the dark. Changes in SPR and colour were monitored daily by UV-visible spectroscopy using a PerkinElmer Lambda 25 UV/VIS spectrometer and digital images taken using a Kodak C813 digital camera, respectively, over three weeks. Particle diameters of all four solutions stored in the light were calculated *via* dynamic light scattering (DLS) on a Zetasizer 3000 (Malvern, UK). Particle diameters of light stored Solution A were also directly measured on Days 1, 4, 7 and 12 to progressively monitor the digestive ripening process using a Jeol 4000EX HRTEM, where samples were prepared by evaporating solution droplets on lacey carbon coated copper grids. Solution E, pre-ripening (Day 1), was also divided into two 9 mL portions and both centrifuged on a Beckman Coulter Avanti Centrifuge J-26 XP at 20,000 rpm (≈ 48,000 g) causing the nanoparticles to rest at the bottom of the solution. Most of the excess un-reacted citrate was removed from one solution and replaced with distilled water. This process was repeated thrice. Solutions were vortexed in order to re-disperse the nanoparticles at rest, once more forming homogenous light pink coloured solutions where their subsequent evolution was monitored by UV-visible spectroscopy.

2.4. Results and discussion

Gold colloid solutions were prepared by the addition of sodium citrate solution to heated auric acid solutions. Upon addition of citrate all solutions initially displayed a colour change from colourless to lilac. After allowing them to cool with stirring, a relatively fast colour change to light red was observed after ≈ 3 mins. Although the oil bath that completely encapsulated the reaction flask was heated homogenously using a temperature controlled resistance wire and the citrate added at a consistent rate, the rate of transition from colourless to lilac to red and the depth of final colour differed slightly for each repeat synthesis. Over time the red solutions deepened in colour regardless of light or dark storage. This was tracked by UV-visible spectroscopy, where an increase in the intensity of the SPR band was observed. The deepening in colour was suggestive of a post-reaction that took place over several days that was due to either: (i) an incomplete initial reduction of auric acid during the heating stage where a subsequent post-reaction occurs with the excess citrate that is present in solution, or (ii) a greater number of smaller nanoparticles are formed from larger nanoparticles due to the digestive ripening of the colloid. A visual example for both light and dark stored solutions of this colour deepening is shown in Figure 2.4.1 for Solution A.

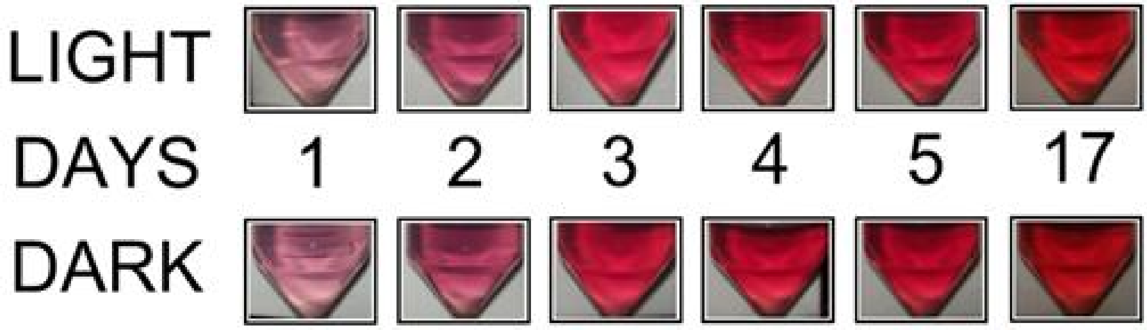

Figure 2.4.1: Chronological images of Solution A, a gold nanoparticle solution produce by the method removed from the heat whilst still purple in colour and allowed to age in both light and dark conditions.

2.4.1. Time Evolution Studies

In the first week, a systematic shift of the SPR band to lower wavelengths was observed for Solutions A–D (light or dark), demonstrating an average size decrease and digestive ripening of nanoparticles in solution. SPR band maxima increased in absorbance intensity, corresponding to the deeper colour seen by eye (Figure 2.4.1). An eventual narrowing of the SPR bands was also observed, indicative of a reduced size distribution of nanoparticles in solution. All these phenomena are clearly seen in Figure 2.4.2(a) from stacked UV-visible absorption spectra taken from Solution A.

Integrating the SPR peaks over the 460–720 nm range quantified the initial increase and levelling of the depth in colour for all solutions. A plot of the SPR peak integrals as well as the SPR band centres for both light and dark stored solutions over a 17 day analysis period is shown for Solution A in Figure 2.4.2(b). The SPR centre decreases systematically from 540 – 526 nm and

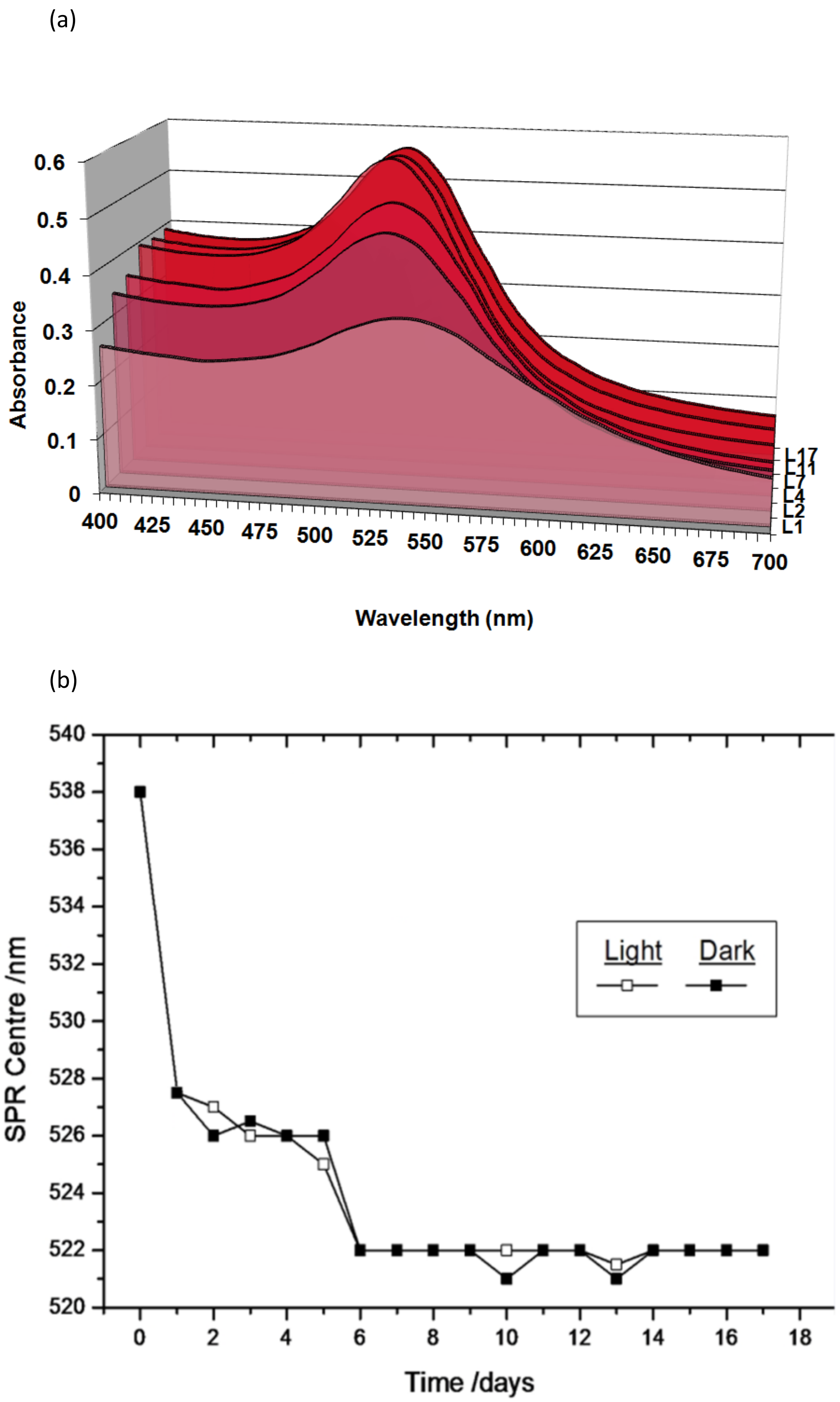

Figure 2.4.2: (a) 3D UV-visible absorption spectra for Solution A stored in the light at select days 1, 2, 4, 7 & 17 and (b) A daily plot of SPR band centre for both light and dark stored solutions of Solution A - Au nanoparticle solutions produced by the Turkevich method and removed from heat whilst still purple in colour.

subsequently levels out at 522–523 nm for Solutions A – D, regardless of light or dark storage, clearly demonstrating the mechanism for this digestive ripening process is not a light activated/ dependent process.

Although on Day 1, there were deviations in the position in SPR band centre, after an extended time period of digestive ripening, all SPR bands maxima fell within 1 nm of each other. Although best efforts were made to conduct the syntheses in the most reproducible way, these initial differences in SPR band position were always seen. Nevertheless, the subsequent ripening process causes an eventual movement of all SPR bands to approximate equivalence in monodispersity (SPR broadness) and size (SPR centre). After a further month of storage in both light and dark samples, partial precipitation of colloidal gold occurred in some samples; however, SPR centres only deviated by ± 1 nm (if at all), consistent with what was previously seen.

Table 2.4.1: Table of information collected from UV-visible absorption spectroscopy, *calculated particle diameters (using the Haiss formula[84]) , dynamic light scattering (DLS) and transmission electron microscopy (TEM) for light stored Solutions A–D; Au nanoparticle solutions produced *via* the Turkevich method and removed from heat whilst still purple in colour.

	Day								
	1	21	1	21	21	1	4	7	12
	UV-visible spectroscopy		<particle diameter> ± standard deviation (nm)						
	SPR centre (nm)		Calculated*		PCS	TEM			
A	538	522	64	6	19 ± 3	19.4 ± 7.3	13.1 ± 3.7	12.2 ± 2.5	11.4 ± 1.5
B	535	522	57	10	23 ± 2	-	-	-	-
C	526	522	35	9	20 ± 2	-	-	-	-
D	540	523	67	10	17 ± 1	-	-	-	13.4 ± 2.1

The hydrodynamic diameters of all four light stored Au nanoparticle Solutions A – D were measured from dynamic light scattering (DLS). The experiment was carried out three times and the values reported in Table 2.4.1 are averages of the central position of the peak maxima. Insufficient correlations in PCS measurements made on Day 1 did not allow the nanoparticle diameters to be accurately determined, and were thus omitted. This was attributed to the wide size distributions indicated by the wide SPR band observed on Day 1 (Figure 2.4.2(a)). The measurements demonstrate the hydrodynamic diameters of the nanoparticles (*i.e.* the gold nanoparticle plus its surfactant and water solvation shell) and were thus approximately double in size compared with particle diameters measured by TEM.

Transmission electron microscopy (TEM) was carried out on light stored Solution A at Days 1, 4, 7 and 12 (Figure 2.4.3). Au nanoparticle diameters were calculated from the resulting images, whereby an average particle size and associated standard deviation were extracted (Table 2.4.1). Au nanoparticles of significantly different average size and distribution were observed for Solution A at Day 1 (Figure 2.4.3(a)) and Day 12 (Figure 2.4.3(d)). An ≈ 20 % decrease in nanoparticle diameter over the ripening period from an average of 15 ± 6 nm to 12 ± 2 nm was in line with the digestive ripening process observed by shifts in the SPR band (Figure 2.4.2(b)). A Welch's t-test demonstrated the high probability that the nanoparticle diameters were significantly different. A decrease in the nanoparticle size distribution, indicated by a sizeable reduction in the standard deviation of sizes, demonstrated a time evolution towards monodispersity and correlated with the narrowing of the SPR band also seen sprectroscopically (Figure 2.4.2(a)). In order to assess whether the inverse-Ostwald nanoparticle growth was dependent upon the presence of excess un-reacted citrate, Solution E was separated in two equal volumes and vigorously centrifuged to force the Au nanoparticles to the bottom of a clear solution. The excess citrate dispersed in aqueous solution above the resting gold was replaced with distilled water in one of the samples. The process of centrifugation was repeated a further two times to make Solution E^{-}. After re-dispersion of the nanoparticles by rapid vortex, causing the solution to become purple once more, the time evolution of both Solutions E and E^{-} was monitored by UV-visible spectroscopy; the changes in SPR centres are shown in Figure 2.4.4(a). A systematic shift and levelling in the SPR centre to lower wavelengths was indicative of an equivalent digestive ripening process occurring in both Solutions E and E^{-}, analogous to non-centrifuged Solutions A – D. TEM images of Solution E^{-} at Day 1 and 12 are shown in Figure 2.4.4(b) and Figure 2.4.4(c) respectively. A similar pattern of size decrease and distribution narrowing to Solution A is observed, with the average size decreasing from 14 – 11 nm. This demonstrated the independence of digestive ripening to the presence of excess citrate and un-

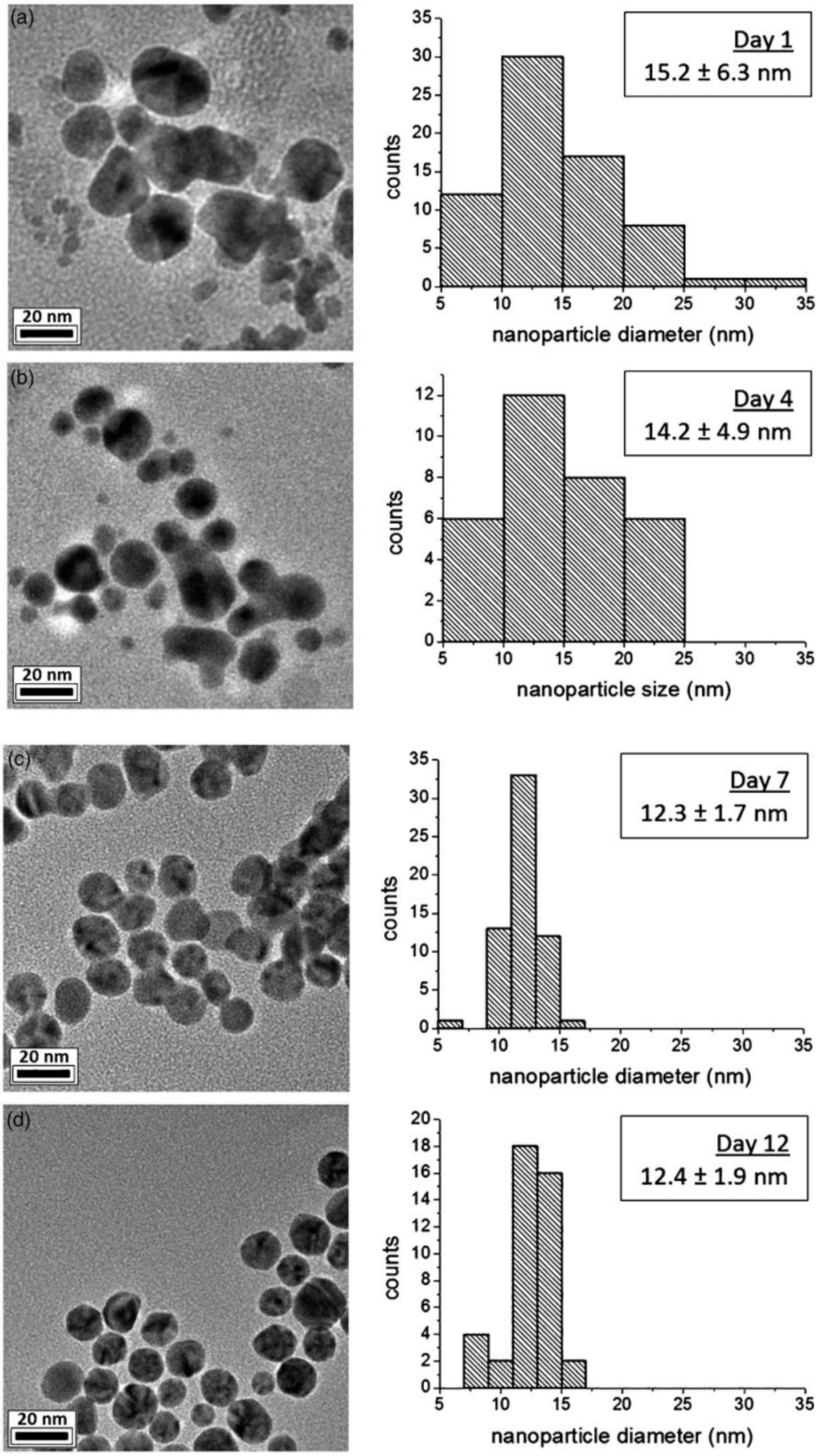

Figure 2.4.3: TEM images of light stored Sample A; a gold nanoparticle solution produced by the Turkevich method and removed from heat whilst still purple in colour, at (a) Day 1 and (b) Day 4 (c) Day 7 and (d) Day 12 with a histogram plot of the size distribution.

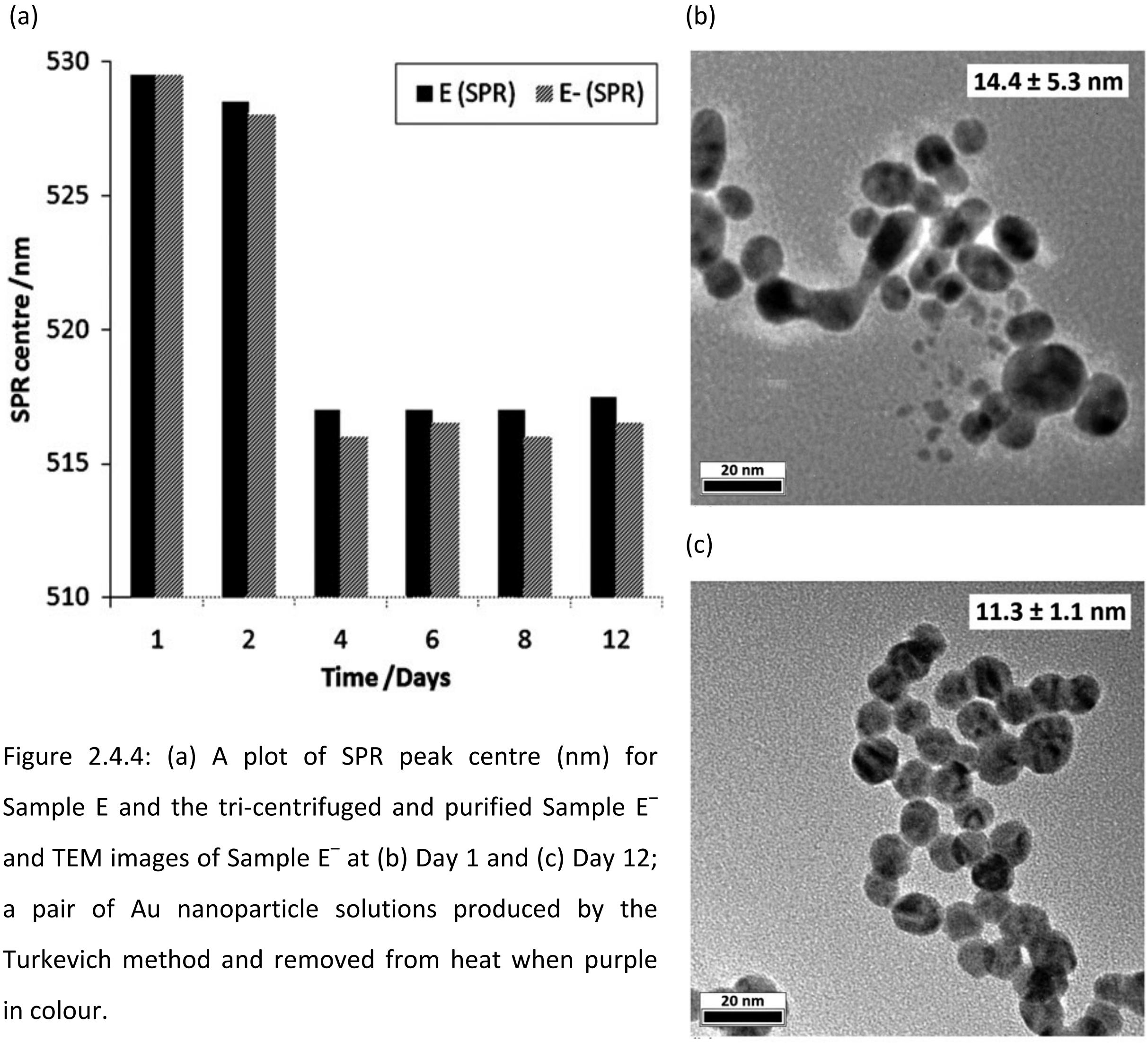

Figure 2.4.4: (a) A plot of SPR peak centre (nm) for Sample E and the tri-centrifuged and purified Sample E^- and TEM images of Sample E^- at (b) Day 1 and (c) Day 12; a pair of Au nanoparticle solutions produced by the Turkevich method and removed from heat when purple in colour.

reacted auric acid and indicated that the inverse-Ostwald growth was likely due to interactions between the gold clusters that initially formed in solution.

Although the Au nanoparticle diameters, derived from the Haiss formula[84] of SPR band centres, were approximately double what was seen in TEM images pre-ripening (Day 1), the difference between prediction and observation post-ripening was minimal (Table 2.4.1). This would indicate that the nanoparticles initially formed in solution tended to agglomerate, as indicated in TEM images (Figure 2.4.3(a)). Even though nanoparticle diameters calculated from UV-visible absorption data post-ripening were of the same order to what was seen from TEM images, they tended to under predict the size. In addition, when predicting larger Au nanoparticle diameters, the equation seemingly breaks down altogether and can only be treated as a rough guide. While post-ripened Au nanoparticle diameters predictions were in line with what was seen in TEM images, they were significantly different from those determined by PCS, which seemingly over-represents Au nanoparticle size given that a hydrodynamic size is measured.

It was evident that initial SPR band position attained from UV-visible spectroscopy did not directly correlate and furthermore demonstrated that the degree of initial Au nanoparticle formation, which differed quite substantially between samples, had no effect on the final nanoparticle size achieved after allowing particles to sufficiently digestively ripen. However, if the solutions are allowed to sufficiently age, near monodisperse nanoparticles are obtained. Notably this synthesis did not give rise to rod-shape nanoparticles. After allowances for aging most of the particles were near spherical in shape although the occasional triangular facet was noted.

Collective assessment of UV-visible, PCS and TEM data clearly shows that a gradual nanoparticle size decrease to an optimum as well as an increase in the monodispersity of sizes occurred for all five Solutions A – E. The rarity of this phenomenon is unsurprising given the process avoids the reduction of interfacial free energy gained from particle aggregation; however by considering the electrostatic interactions between particles computational models have accounted for this behaviour for systems under reflux.[89] Some groups have exploited this process in creating monodisperse Au nanoparticle solutions by refluxing polydisperse colloids with a series of alkylthiols invoking digestive ripening.

The works of Chow and Zukowski[79] and Rodriguez-Gonzalez,[78] discussed in Section 1.3, gave strong insight into the formation mechanism of colloidal gold from the Turkevich method. In both works the reactions were heated until completion (*i.e.* a deep red coloured solution was formed). In this investigation, solutions were removed from reflux as soon as a purple coloured solution was observed – previously established by Rodriguez-Gonzalez as the tipping point where inverse-Ostwald growth begins.[78] By cutting the reaction short at this point, we were able to monitor the inverse-Ostwald growth process over an extended period of time at room temperature. Moreover, by removing any unreacted reagent sources by centrifugation, we were able to demonstrate how this process was due to interactions between gold clusters alone – a conclusion that was in line with those found previously whilst heating over shorter time-scales.

2.5. Conclusion

A simple Turkevich method was used to produce five Au nanoparticle solutions that were stored either in the light or dark. Daily monitoring of the solutions with UV-visible absorption spectroscopy identified a gradual time evolutionary shift in the SPR centre of solutions to lower wavelengths, indicating a decrease in particle size. An eventual stabilization of SPR centres at approximately 522 nm for all samples, both light and dark, demonstrated the independence of lighting conditions upon the mechanism of this inverse-Ostwald growth (*i.e.* digestive ripening). A size decrease from roughly 15 nm at synthesis to around 11 – 12 nm at stabilization was confirmed by TEM imaging. An overall increase in the monodispersity of sizes after the ripening period was indicated by a tightening of the SPR bands alongside particle size analysis of TEM images. In removing reaction by-products and excess reagents we were able to prove that this process was not an extended chemical reaction but rather a physical process of re-ordering. Further examination showed that this long term process of particle re-ordering (from days – weeks at room temperature) could be dramatically sped up by thoroughly refluxing the colloid (in a matter of minutes). This study has shown that Au nanoparticles of increasingly consistent size can be obtained the Turkevich method by either harvesting for a pre-determined time period or heating reaction solutions for a prolonged period of reflux.

In the next chapter we explore the effect of changing the way in which Turkevich gold nanoparticle formation reactions are initiated and propagated on the size, shape and monodispersity of the colloid produced. This was investigated for the standard thermally heated reactions in addition to microwave, ultra-violet and sonolysis activation for a range of solution concentrations. In varying the initiation method we found that the size, shape and monodispersity of the colloidal gold would distinctively change, thus allowing the surface plasmon resonance properties of gold nanoparticles to be tuned, simply by changing the method of activation.

3. The effect of activation method on the size, monodispersity and shape of gold nanoparticles formed by the Turkevich method

3.1. Overview

This chapter describes the growth of gold nanoparticle colloids using heat, sonolysis, microwave (MWA) or UV light (254 nm). The solutions were formulated analogous to Turkevich *et. al.* and contained an auric acid gold source and different amounts of sodium tri-citrate reductant and stabiliser. The effect of activation method was studied, showing marked differences in the monodispersity, size and shape of particles formed – elucidated by transmission electron microscopy (TEM) imaging. Properties such as average particle size and shape were directly related to changes in the surface plasmon resonance (SPR) band from UV-visible absorption spectra.

We show how a variety of basic activation methods can be used to synthesise near monodisperse gold colloids. More importantly, demonstrate how the activation method is fundamental to the eventual size of the particles formed; with sizes ranging from 11.0 – 11.9 nm in thermal reactions, 16.9 – 18.0 nm in sonolysis reactions, 11.3 – 17.2 nm in MWA reactions and 8.0 – 11.2 nm in UV initiated reactions. Possible reaction pathways and mechanisms are put forward to explain these marked differences.

3.2. Introduction

In order to investigate the effect of activation method on the resultant properties of the colloid, a single system that is versatile to several activation methods was employed. As discussed earlier in Chapters 1 and 2, the most commonly observed system for gold nanoparticle growth is the thermal tri-citrate reduction of auric acid in water, devised by Turkevich *et. al*.[76,77] The mechanism by which the predominantly spherical particles are formed has been studied by several groups[78,79,83] and by ourselves (Chapter 2). In addition, the effect on the reaction kinetics, monodispersity and eventual size of particles formed in accordance to varying the sodium tri-citrate to auric acid ratio, heating rate and temperature have also been comprehensively studied; where gold nanoparticles ranging from ≈ 10 – 100 nm in median size can be grown.[76,78,79,83]

In this chapter, we investigate the effect of activation method in the formation of gold colloids from the reduction of auric acid by tri-sodium citrate (*i.e.* the Turkevich method). We believe this to be the first instance in which UV light has been shown to initiate gold nanoparticle growth in this system, this is to our knowledge the first comparative study of activation methods for gold nanoparticle formation by the Turkevich method. Surprisingly near monodisperse particles could be made with a median size and distribution of sizes governed by the activation method used.

3.3. Experimental

All reagents were purchased from Sigma-Aldrich UK unless otherwise stated. All glassware was washed with aqua regia and rinsed with copious amounts of deionised water before use. Four solutions of differing tri-sodium citrate ($Na_3C_6H_5O_7.2H_2O$) concentrations and constant auric acid ($HAuCl_4.3H_2O$) concentration were made up for each activation method tested; labelled as Solutions A – D. Solutions were made up to a volume of 10 ml in distilled water, with masses and concentrations of reagents shown in Table 3.3.1.

Table 3.3.1: Mass and concentration of auric acid (gold source) and tri-sodium citrate (reducing agent/ surfactant) in 10 ml of distilled water in solutions labelled A - D. Solutions A - D were made up each time and the reduction reaction initiated by either (i) thermal heating (ii) sonication (iii) microwave and (iv) UV light (254 nm).

Solution Identifier	Auric acid	Tri-sodium citrate
A	0.85 mg, 0.28 mM	0 mg, 0 mM
B	0.85 mg, 0.28 mM	2.5 mg, 0.96 mM
C	0.85 mg, 0.28 mM	5.0 mg, 1.94 mM
D	0.85 mg, 0.28 mM	10 mg, 3.88 mM

A set of Solutions A – D were made up each time for each activation method tested; thermal heating, sonolysis, microwave (MWA) or UV light. A table of the reaction protocol for each type of synthesis is shown in Table 3.3.2.

3.4. Results and discussion

A range of activation methods was used to form gold nanoparticles from reaction of auric acid with tri-sodium citrate. This enabled a comparative study of how the size, shape, monodispersity and surface plasmon resonance (SPR) properties of the nanoparticles formed varied with thermal, sonolysis, microwaves and UV irradiation.

Colour changes characteristic for the formation of gold nanoparticles by citrate reduction of auric acid were observed in Solutions B - D for all activation methods tested; with final colours ranging from light lilac to deep red (Figure 3.4.5). No colour changes were seen in Solution A, regardless of the activation method used. Solution A differed from Solutions B - D, as it did not contain any tri-sodium citrate reducing agent. The results showed the importance of the reducing agent in the formation of gold nanoparticles; regardless of the activation method used.

Table 3.3.2: A list of the protocol undertaken for initiating the reduction reaction of auric acid in tri-sodium citrate in Solutions A - D for the formation of gold nanoparticles. Solutions were activated by either (i) thermal heating (ii) sonication (iii) microwave or (iv) UV light (254 nm).

Activation Method	Protocol
Thermal heating	Heated homogenously in an oil bath with a temperature controlled resistance wire (Banstead Electrothermal 230V/200 W) from room temperature to 100 ˚C. Removed from the heat after boiling for approximately 10 mins and then allowed to cool to room temperature.
Sonolysis	Sonicated (Fischer Scientific; 35 W – 1.5 L capacity) in a distilled water bath at room temperature for 60 mins at 60 Hz and then left to stand for 24 hr at room temperature.
Microwave	Microwave heated (Proline MicroChef ST22 750 W) for 3 mins under reflux and allowed to cool to room temperature.
Hard UV light	Photo-irradiated with hard UV light (254nm - Vilber Lourmat 2 x 8W VL-208G) in shallow glass dishes (7 cm diameter) for 60 mins. Lamp to sample distance was ≈ 10 cm.

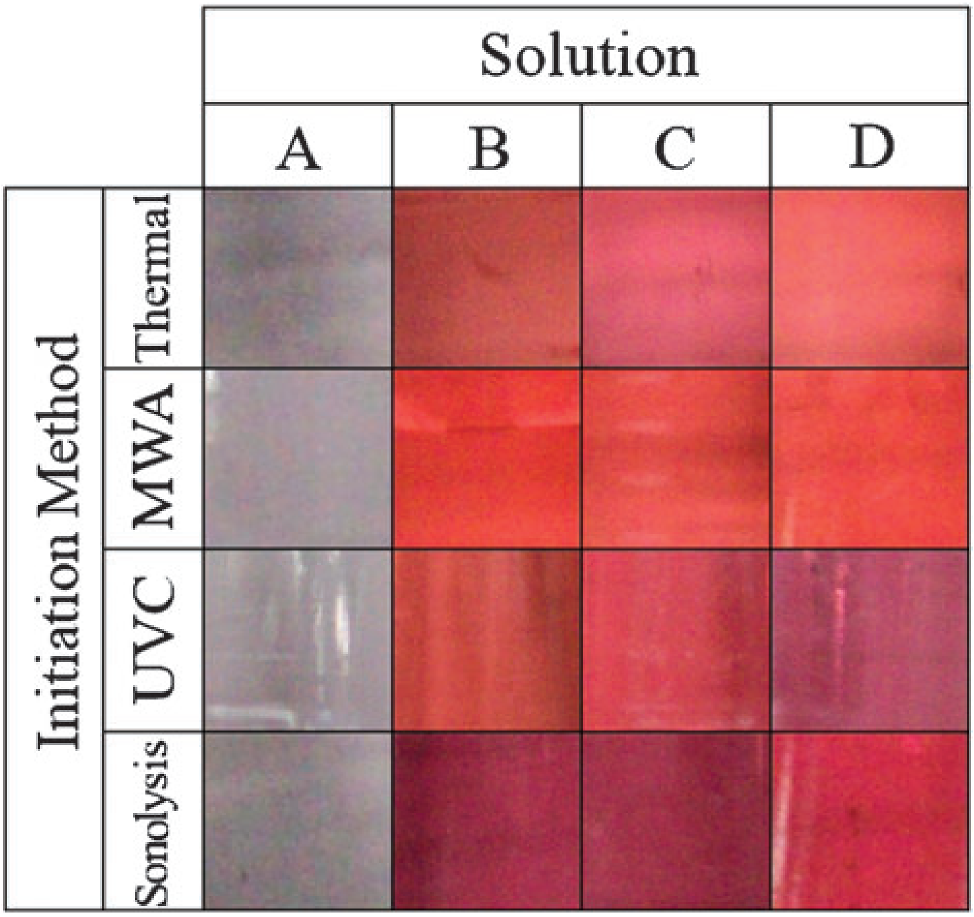

Figure 3.4.1: The colour observed after 24 hrs storage of Solutions A–D; aqueous auric acid solutions with varying tri-sodium citrate concentrations after reaction by each activation method tested (thermal heating, sonication, microwave and UV light).

Bright ruby-red coloured solutions were formed in MWA reactions; with more pink-purple coloured solutions formed by thermal heating and UV activated reactions. Initially, colourless solutions were observed in sonolysis reactions after 60 mins of sonication; however, colour began to show after leaving the solutions to stand (≈ 3 – 6 hrs) and deepened to a final dark red-purple colour after ≈ 24 hrs.

The resultant gold nanoparticle solutions from each reaction of auric acid and tri-sodium citrate (B - D for each activation method tested) were analysed by UV-visible spectroscopy 24 hrs after activation, as shown in Figure 3.4.2. SPR bands centred between *ca* 519 – 530 nm, characteristic of gold nanoparticle growth, were observed in solutions B - D for all methods of activation. Changes in the SPR band heights and centres ranged from 0.28 – 0.59 Abs units and 519 – 529.5 nm respectively (Table 3.4.1). This corresponds with variation in colloidal properties; such as the average nanoparticle size, monodispersity, shape and degree of agglomeration. All solutions showed a weak additional absorption band at ≈ 260 nm. This peak corresponded to the presence of some un-reacted auric acid, the gold source in the nanoparticle formation reactions.[36] Solutions activated by MWA showed a more prominent absorbance at this position than any other reaction type (Figure 3.4.2). Although this indicated the MWA reactions were less complete than others, their average SPR band absorption height (0.47 Abs units) was of the same order as other activation methods (0.50, 0.43, 0.51 – thermal, UV, sonolysis respectively); with values of individual solutions shown in Table 3.4.1.

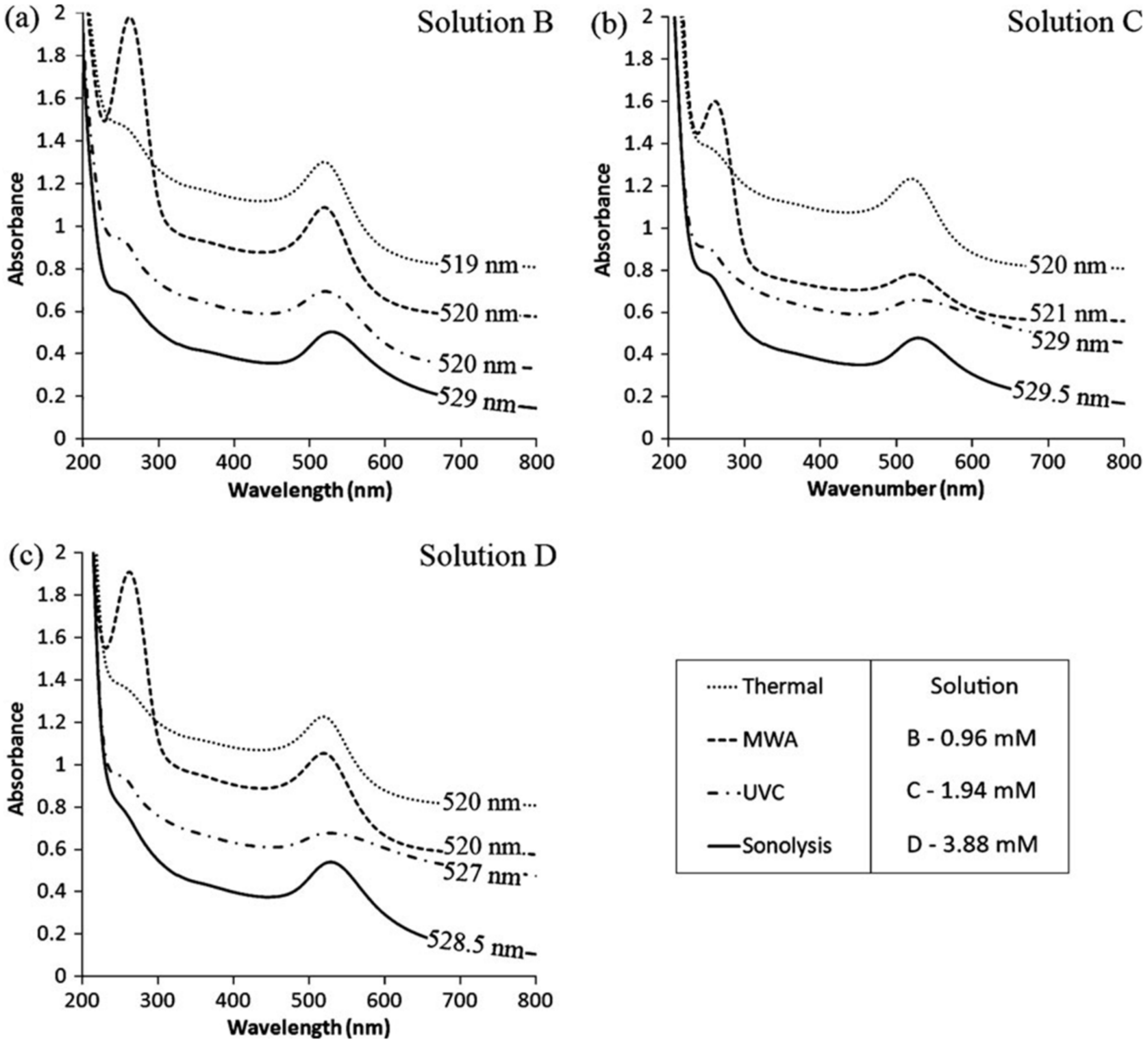

Figure 3.4.2: Stacked UV-visible absorption spectra for gold nanoparticle solutions formed by the reduction reaction of auric acid (0.28 mM) by tri-sodium citrate of varying concentration (Solutions B – D, 0.96 – 3.88 mM) where the reactions were activated by either thermal heating, sonication, MWA or UV light. Numbers on each profile show the position of the SPR band centre.

Table 3.4.1: Table of SPR band centres and absorption maxima from UV-visible absorption spectroscopy studies in addition to the average nanoparticle size and standard deviation error of sizes from TEM imaging of Solutions B - D (tri-sodium citrate 0.96, 1.94, 3.88 mM in B-D respectively, auric acid consistently 0.28 mM) activated by either thermal, MWA, UV or sonolysis.

		TEM	Surface Plasmon Band	
		Median particle size ± deviation (nm)	Centre (nm)	Absorbance Maximum
Solution B	Thermal	11.4 ± 2.2	519.0 (5)	0.55 (1)
	MWA	17.2 ± 2.4	520.0 (5)	0.59 (1)
	UV	8.0 ± 1.4	520.0 (5)	0.44 (1)
	Sonolysis	16.9 ± 2.1	529.0 (5)	0.50 (1)
Solution C	Thermal	11.0 ± 1.9	520.0 (5)	0.48 (1)
	MWA	11.6 ± 0.9	521.0 (5)	0.28 (1)
	UV	10.8 ± 2.4	529.0 (5)	0.41 (1)
	Sonolysis	18.0 ± 5.0	529.5 (5)	0.48 (1)
Solution D	Thermal	11.9 ± 2.0	520.0 (5)	0.48 (1)
	MWA	11.3 ± 1.6	520.0 (5)	0.56 (1)
	UV	10.9 ± 2.3	527.0 (5)	0.43 (1)
	Sonolysis	17.9 ± 6.1	528.5 (5)	0.54 (1)

It had been previously reported by Rodriguez-Gonzalez *et. al.* that the gold nanoparticle formation mechanism in the thermal reduction of auric acid proceeds *via* the formation of tiny gold clusters (≈ 1 – 2 nm in diameter) that bind together to form large grape like structures up to 100 nm in diameter, which subsequently break apart to form the resultant colloid consisting of Au particles ≈ 10 nm in diameter.[78] It was also shown using titrations and electrode potential measurements that the concentration of Au(III) ions in solution decreased steadily upon boiling until complete reduction occurred.[83] These $AuCl_4^-$ ions are initially reduced by electron transfer from citrate ions to $AuCl_2^-$, which preferentially absorb excess chloride ions present in solution over citrate.[94] Excess $AuCl_4^-$ ions present in solution were continually absorbed on the surface of Au (I) particles and subsequently reduced by further electron transfer from citrate. Au (I) particles continued to grow to ≈ 1 – 2 nm in diameter, whilst stabilised by surrounding chloride ions. Due to their almost zero net charge, flocculation was induced and large particle clusters formed that were ≈ 100 nm in diameter. When a saturation limit of $AuCl_2^-$ was reached, further citrate reduction produced Au atoms that ejected the surrounding chloride ions and chemisorbed with lightly bound surrounding citrate ions. This peptization process occurs rapidly, forming many smaller particles that are ≈ 10 nm in diameter. Although the final colloid contains a majority of medium sized nanoparticles of around 10 nm in diameter some of the smaller gold clusters (≈ 1 – 2 nm in diameter) remain. As the 1 – 2 nm gold clusters do not show SPR properties, being below the SPR limit, they are not detectable by UV-visible spectroscopy but can be seen in low concentration using transmission electron microscopy (TEM).

In this study, gold colloids were grown from the analogous reaction of auric acid and tri-sodium citrate by various activation methods. For reactions activated by MWA radiation, the height, width and position of the resulting SPR bands were similar to those formed by thermal heating (with the exception of solution C, see Table 3.4.1). This was a strong indication that the final concentrations of gold nanoparticles formed were similar using both methods. However, a significantly larger presence of un-reacted auric acid was observed by UV-visible spectroscopy (peak at ≈ 260 nm) in reactions activated by MWA radiation. If we assume that both methods produced solutions of equal gold nanoparticle concentration, this demonstrated two possible differences where either: (i) MWA reactions were more efficient at converting auric acid to gold nanoparticles or (ii) the MWA had a lower propensity to form tiny gold clusters (≈ 1 – 2 nm in diameter) that do not show SPR properties, assuming the mechanism proceeded analogously to thermal reactions.[78]

If we assume that the nanoparticle formation mechanism in MWA reactions proceeded analogously to thermal reactions, we can guess that a more highly efficient conversion of the large multi-core particle intermediates to the resultant colloid occurred. However, the lower propensity for consumption of the auric acid source is not easily explained. It is well known that MWA heating causes *in situ* rapid heating of solution pockets to occur, which may have induced the localised growth of nanoparticles, elsewhere leaving un-reacted auric acid in cooler solution packets.

In UV light reactions, comparatively broader SPR bands were observed (Figure 3.4.2). This indicated a number of possibilities such as decreased monodispersity, increased particle agglomeration or changes in nanoparticle shape.[84,85,95] A significant red-shift in the SPR band centre from 520 nm (Solution B) to 529 nm (Solution C) was also observed. The effect was attributed to the two-fold increase in the tri-sodium citrate concentration from Solution B to C. A small blue-shift to 527 nm was seen upon further increase in the tri-sodium citrate concentration in Solution D. The change in particle size observed when increasing reductant concentration could not explain the subsequent red and blue shifts in the SPR band. TEM imaging studies later confirmed the presence of elliptical particles with varying degrees of aspect ratios, which provided an explanation for the changes in SPR properties (Figure 3.4.3).

Solutions activated by sonolysis remained colourless after 1 hr of sonication. A slow nanoparticle formation reaction proceeded upon leaving the solutions to stand. Initial signs of colour were observed after 6 hrs, which deepened in colour to a plateau after 24 hrs. SPR bands of the resultant colloids were red-shifted with respect to thermally activated reactions, ranging relatively invariantly from 528.5 – 529.5 nm. This implied the presence of significantly larger nanoparticles, which was later confirmed in TEM studies (Figure 3.4.3). It is well documented how sonication can agitate H_2O and generate $\dot{H}$ and $\dot{OH}$ radicals. However, Nagata *et. al.* found that H radicals readily combine with atmospheric O_2 forming $H\dot{O}2$ radicals that compete with auric acid reduction.[96] The competition reaction provides an adequate explanation as to why Solution A of this study did not show any evidence of colloidal gold formation, given tri-sodium citrate was not added (Table 3.3.1). Gold colloids were similarly grown by Su *et. al.* by sonicating auric acid and tri-sodium citrate solutions.[97] The presence of the tri-sodium citrate reducing agent was found to be fundamental to the formation of gold nanoparticles. H^1 NMR evidence indicated the reduction mechanism proceeded from the removal of the OH group from tri-sodium citrate – scavenged by $\dot{H}$ radicals generated in water by sonication. These tri-sodium citrate radicals subsequently reduced Au^{3+} species in solution to Au^0. Subsequent nucleation of the Au^0 atoms into larger particles is followed by capping with tri-sodium citrate surfactant. In this study, the red coloration showing colloidal gold formation appeared several hours after sonication. Examination of the sonolysis reduction mechanism indicates a two-step process whereby the initial sonication energy induces the formation of Au^0 particles that require significant periods of time (≈ 1 day) to fully nucleate and cap to form a stabilised colloid.

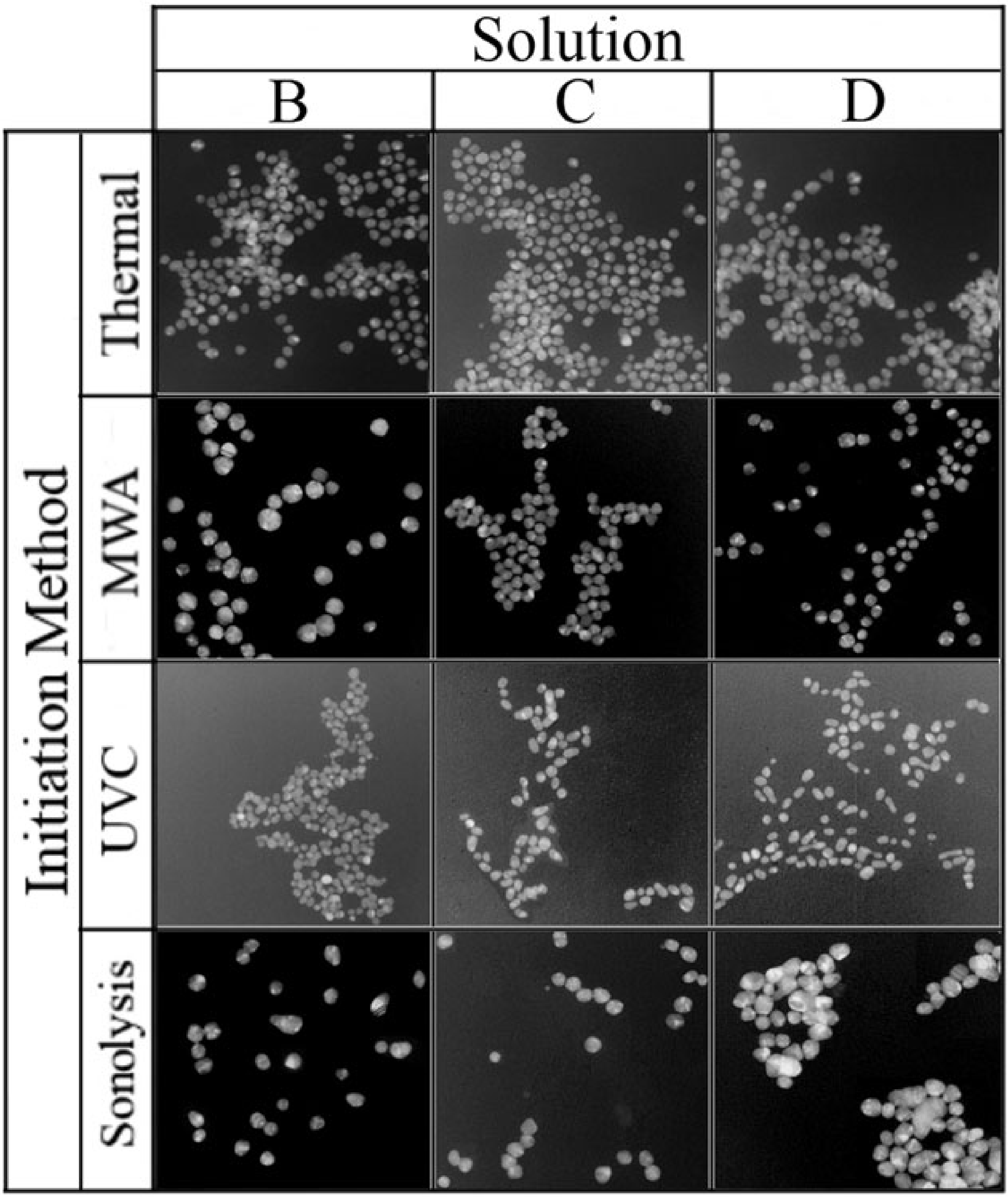

Figure 3.4.3: TEM images of gold nanoparticle solutions formed by the reduction reaction of auric acid (0.28 mM) by tri-sodium citrate in differing concentrations (0.96, 1.94, 3.88 mM in Solutions B – D respectively) where the reaction was activated by either thermal heating, sonication, microwave (MWA) or UV light (254 nm). All images were taken at 100,000x magnification, where the width of each image represents a distance of 300 nm.

The gold nanoparticles formed in Solutions B - D by each activation method were investigated by TEM. Solution droplets were cast onto lacey carbon-coated copper grids and air-dried before analysis. All reactions of Solution A showed no sign of nanoparticle growth; this corresponded with the absence of a colour indicating no SPR band (Figure 3.4.2). This verified the importance of the tri-sodium citrate reducing agent for inducing nanoparticle growth, irrespective of the activation source used in this study. Representative images of all colloids formed are shown in Figure 3.4.3. Median and standard deviations in the measured nanoparticle diameters, from sets of at least 70 - 100+ measured particles are listed in Table 3.4.1.

Thermally activated reactions showed almost invariant average particle size (11.0 – 11.9 nm) and monodispersity (1.9 – 2.2 nm standard deviations) with an increased tri-sodium citrate concentration from 0.96 mM in Solution B to 3.88 mM in Solution D. This supported the UV-visible absorption studies, where no significant change in position, width or height of the SPR band was observed (Table 3.4.1). For thermally activated reactions, Student t-tests showed that the average nanoparticle size in Solution B (11.4 nm) had little chance of being significantly different from either Solutions C (11.0 nm) or D (11.9 nm); indicating equivalence (less than 1 %). Within the tri-sodium citrate concentration range tested, little effect on the resulting colloid was observed (0.96 – 3.88 mM).

Contrary to thermal reactions, TEM images of Solutions B - D activated by MWA radiation showed a transition from larger nanoparticles formed in Solution B from 17.2 nm diameter on average to significantly smaller particles in Solutions C and D with 11.6 and 11.3 nm in average diameter. The monodispersity of all solutions was high, with relatively low standard deviations ranging from 0.9 – 2.4 nm. In contrast to what was seen in thermally activated reactions, a concentration dependence of the tri-sodium citrate reductant was observed; where doubling the tri-sodium citrate concentration from 0.96 mM to 1.94 mM yielded smaller particles. A further increase in the reductant concentration from 1.94 mM (Solution C) to 3.88 mM (Solution D) did not form smaller particles. Student t-tests showed that the probability that nanoparticles formed in Solution B was different from Solutions C and D was 99.9 %; verifying the differences observed statistically (Table 3.4.1) and by eye (Figure 3.4.3). The t-tests also showed that Solutions C and D were most likely equivalent.

Solutions activated by UV light were not only relatively monodisperse but showed lower average particle sizes; with the lowest average size seen in Solution B at 8.0 nm. However, the colloids became increasingly more elliptical in shape with increased tri-sodium citrate concentration as seen in Figure 3.4.4.

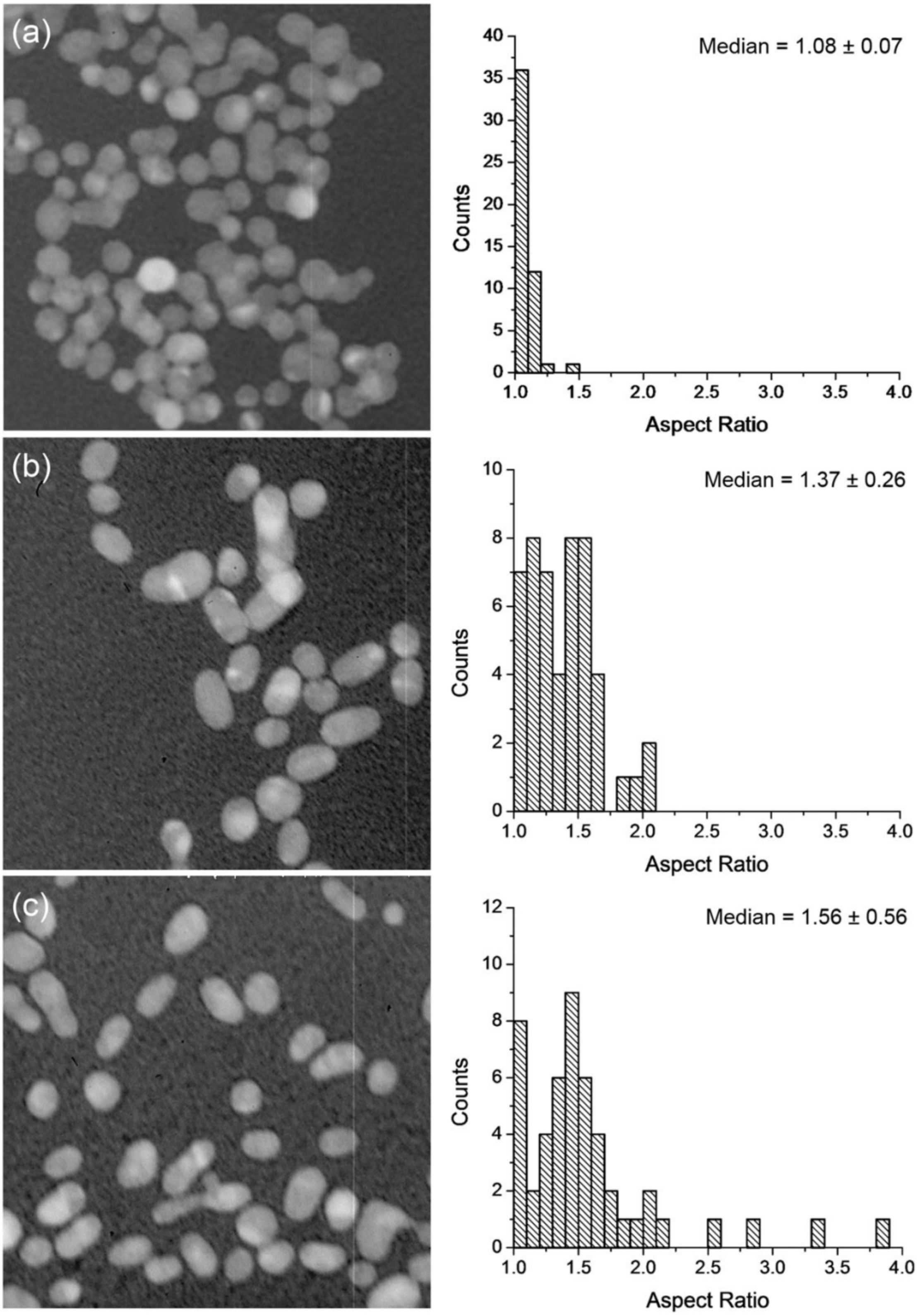

Figure 3.4.4: TEM images of gold nanoparticle solutions formed by the reduction reaction of 0.28 mM auric acid with tri-sodium citrate of varying concentration (a) 0.96 mM, (b) 1.94 mM and (c) 3.88 mM activated by UV light (254 nm). All images were taken at 100,000x magnification, where the width of each image represents a distance of 130 nm. Histogram plots of the variation in aspect ratio of the elliptical nanoparticles are plotted adjacently; median and standard deviations are quoted.

Measurement of the size aspect ratios of particles quantified the differences observed. Solution B, containing the lowest tri-sodium citrate concentration, yielded the most spherical particles with an average size aspect ratio of 1.08 ± 0.07. Increases in citrate concentration caused an increase in the elliptical nature of the particles formed, with 1.96 mM Solution C and 3.88 mM Solution D showing size aspect ratios of 1.37 ± 0.26 and 1.56 ± 0.56 respectively. These disparities in shape might explain the unconventionally large shifts in the SPR band with little change in average nanoparticle size (Figure 3.4.2).[95] Student t-tests showed that Solutions C (10.8 ± 2.4 nm) and D (10.9 ± 2.3 nm) could not be said to be significantly different from all other solutions made in this study; however it was 99.9 % probable that Solution B (8.0 ± 1.4 nm) was significantly smaller in average nanoparticle size than all other colloids.

Nanoparticle syntheses activated by sonolysis were significantly larger than particles formed by thermal, MWA and UV light. Average particle sizes ranged from 16.9 to 18.0 nm. Although the colloids showed generally lower degrees of monodispersity (Table 3.4.1), Student t-tests confirmed that they were significantly different (by > 98 % chance) than all other colloids formed, bar one, MWA - Solution B. The average red-shift in the SPR band (by ≈ 9 nm on average) of sonicated solutions compared with thermally activated solutions was complemented by an average increase in particle size by ≈ 6 nm in diameter. This was in contrast with UV and MWA activated solutions where little correlation between the SPR band centre and average nanoparticle size was observed.

Previous work by Turkevich *et. al.*[77] not only established the nucleation and growth process of colloidal gold by thermal reduction of auric acid with tri-sodium citrate, but also investigated the effect of adjusting reductant concentration, gold concentration and temperature. With the auric acid concentration kept constant at 0.25 mM, a range of tri-citrate concentrations of 0.20, 0.38 and 1.96 mM were investigated forming average nanoparticle sizes of 25 ± 5, 18 ± 4 and 14 ± 2 nm respectively (Table 3.4.2).

In our work the solutions were of almost equivalent concentration to one of those formulated by Turkevich *et. al.*, with Solution C consisting of 0.28 mM auric acid and 1.96 mM tri-sodium citrate. In the thermal reduction reaction in this study, Solution C formed gold nanoparticles 11 ± 2 nm in size, whilst the almost analogous reaction by Turkevich *et. al.* quite similarly formed nanoparticles 14 ± 2 nm in size. The slight variation in average size could be attributed to a number of differences in experimental procedure. For instance, Turkevich *et. al.* boiled their solutions for half the time (5 mins). In addition, Turkevich *et. al.* added tri-sodium citrate to a boiling auric acid solution whereas we added the tri-sodium citrate to a room temperature auric acid solution that was then heated to the boil.

Table 3.4.2: A table comparing the synthetic conditions and resulting average particle diameters of gold colloids prepared by other groups who have similarly produced gold nanoparticles from the reduction of aqueous auric acid solutions by tri-sodium citrate using thermal heating, microwave (MWA), soft UV light (365 nm) or sonication.

Activation Method	Concentrations (mM)		Average particle diameter ± error (nm)	Reference
	Auric acid	Tri-sodium citrate		
Thermal (100 °C, 5 mins)	0.25	0.20, 0.38, 1.96	25 ± 5, 18 ± 4, 14 ± 2	Turkevich *et. al.*[77]
MWA (125 °C, 80 °C min^{-1}, 600 W, 15 mins)	1.0	0.9, 2.2, 3.5, 6.0, 7.5	75 ± 8, 22 ± 2, 20 ± 2, 18 ± 1.5, 25 ± 5	Liu *et. al.*[58]
Sonolysis (4 °C, 20 kHz, 15 – 30 mins)	0.49	1.9, 2.9, 3.9	18.9 – 19.4, 18.4 – 20.9, 16.9 – 22.0	Su *et. al.*[97]
UVA (365 nm, 1 mW cm^{-2}, 2 hrs)	2.0	2.0	30 – 70 (median ≈ 60)	Kimling *et. al.*[76]

The colloids made by Turkevich *et. al.*[77] were spherical and relatively monodisperse, analogous to gold nanoparticles formed by thermal heating in this study. Yet Turkevich *et. al.* witnessed significant changes in average nanoparticle size upon varying the tri-sodium citrate concentration. The average nanoparticle size increased in their solutions from 14 to 25 nm on increasing the tri-sodium citrate concentration from 1.96 mM to 0.20 mM (≈ a factor of 10 decrease in reducing agent concentration). In this study, the tri-sodium citrate concentration was varied merely by a factor of 2 and did not yield significant changes for thermally activated reactions.

Gold nanoparticles formed by the tri-sodium citrate reduction of auric acid were also activated by MWA radiation in the work reported by Liu *et. al.*[58] A wide range of tri-sodium citrate concentrations were examined; from 0.9 mM to 7.5 mM solutions with the auric acid solution kept consistent at 1 mM; almost four times more concentrated than in solutions formulated in this study. The average nanoparticle size of the resulting colloid was dependent upon the tri-sodium citrate concentration with a similar trend to results from this study. Liu *et. al.* observed a sharp decrease in average nanoparticle size from 70 ± 8 nm to 20 ± 2 nm upon increasing the citrate concentration from 0.9 mM to 2.2 mM. Further increases in the reducing agent concentration from 2.2 mM to 6.0

mM yielded no further change in colloidal particle size. A similar dependency was observed in this study, where an increase in tri-sodium citrate concentration from 0.96 mM to 1.96 mM yielded an initial decrease in average nanoparticle size from 17 ± 2 nm to 12 ± 1 nm with a further increase in reducing agent concentration causing no significant change (3.88 mM, 11 ± 2 nm). Although both sets of colloids formed by MWA activation were highly monodisperse and spherical, contrasting differences in average nanoparticle size were observed and could be attributed to a number of factors; for instance the microwave used by Liu *et. al.* was 25 % less powerful and solutions were irradiated for only 3 mins in our study compared to the 15 mins by Liu *et. al.*[58] In light of the work conducted by Turkevich *et. al.*[77] that established the high dependency of the tri-sodium citrate/ auric acid concentration on the resultant average nanoparticle size, the contrasting size differences between MWA activated reactions in our study and that of Liu *et. al.*[58] could be attributed to the consistent factor of four difference in the auric acid concentration; with 0.28 mM used in our study and 1 mM used in their work.

Work conducted by Su *et. al.*[97] utilised sonication to induce nanoparticle formation form auric acid and tri-sodium citrate. A range of citrate concentrations from 0.49 mM to 3.9 mM were examined with the auric acid concentration kept constant at 0.49 mM. Lower levels of tri-sodium citrate from 0.49 mM to 1.5 mM caused large nanoparticle clumps to form upon sonication, ranging in size from 100 – 400 nm. Increasing levels of sonication lead to the formation of spherical and monodisperse colloids 17 – 22 nm in average diameter with a small size deviation of 1 – 2 nm. Although no particle clumping was seen in colloids formed by sonolysis in our study, there were several differences in experimental procedure. For instance, Su *et. al.* used ice-cooled solutions (≈ 4 °C) and sonicated at a frequency of 20,000 Hz whereas reactions in this study were conducted at room temperature at a much lower sonication frequency of 60 Hz. Additionally, solutions formulated by Su *et. al.* contained approximately double the gold content compared with our work. In comparing the effect of the tri-sodium citrate: auric acid ratio upon the resultant average nanoparticle size, Su *et. al.* demonstrated little change over the 3: 1 to 8: 1 citrate: auric acid regime with particles formed 17 – 22 nm in average size.[18] In our study, a 3.5: 1 to 14: 1 citrate: auric acid regime was investigated with particles ranging quite similarly in average size from 17 – 18 nm. Although a sonication frequency orders of magnitude more powerful was used by Su *et. al.* and a length of activation up to four times longer was used in this study, the resultant particle sizes compared well.

Hard UV irradiation was used to initiate the formation of colloidal gold from solutions of auric acid with a tri-sodium citrate reductant. We believe this to be the first instance in which UV light (254 nm) has induced nanoparticle formation from this set of reagents, however, Kimling *et. al.* demonstrated this process could be also induced by UVA (365 nm light) irradiation.[76] A comparatively larger auric acid concentration of 2.0 mM with a similar level of tri-sodium citrate was used by Kimling *et. al.*, which lead to the formation of colloidal gold with a larger size distribution ranging from 30 – 70 nm and nanoparticles ≈ 60 nm in average diameter. Far smaller and more monodisperse colloids were formed in this study ranging 8 – 11 nm in average size with deviations of 1 – 2 nm. The elliptical nature of nanoparticles formed in this study was not observed by Kimling *et. al*. Higher tri-sodium citrate: auric acid ratios were used in this study ranging from 3.5: 1 to 14: 1 compared with a 1: 1 ratio used by Kimling *et. al.* Interestingly, we found that higher tri-sodium citrate: auric acid ratios increased the deviation from spherical to elliptical from an aspect ratio of 1.08 at 3.5: 1 to 1.56 at 14: 1. As such, we believe that the increase in elliptical nature is not due to a harder UV light source being used herein but rather an effect of using UV light to activate reactions in conjunction with a high tri-sodium citrate: auric acid ratio.

Although several groups have individually investigated the thermal, sonolysis, MWA and UV activated formation of colloidal gold from auric acid and tri-sodium citrate, we believe this is the first complete study that has investigated the effect of all sources together. By testing equivalent sets of solutions over a range of tri-sodium citrate concentrations we were able to observe the contrasting differences the activation method had upon the resulting colloid.

3.5. Conclusion

Near monodisperse gold nanoparticle colloids were formed by a variety of activation methods (thermal, microwave assisted, hard ultra-violet light and sonication) for a range of solutions that contained a constant concentration of auric acid (0.28 mM) and varied concentrations of tri-sodium citrate (0 – 3.88 mM). Gold nanoparticle solutions did not form unless tri-sodium citrate was present, regardless of the activation method used. When the reducing agent was present, monodisperse gold nanoparticle formation occurred in every case. Nanoparticle solutions formed in the presence of the reducing agent by the tradition thermal method devised by Turkevich *et. al.* were unaffected by increases in the citrate concentration and formed spherical particles 11.0 – 11.9 nm in average diameter. Gold nanoparticles formed in sonolysis reactions were also unaffected by increases in the citrate concentration and formed larger spherical particles 16.9 – 18.0 nm in average diameter. MWA reactions were concentration dependent at 0.96 mM, forming spherical nanoparticles 17.2 nm in average diameter and smaller nanoparticles at higher citrate concentrations that were 11.3 – 11.6 nm in average diameter. UV light activated reactions typically formed smaller nanoparticles, 8.0 – 10.9 nm in average diameter, where particles were more elliptical in nature. In this study, an independence to changes in the citrate concentration was observed over the 0.96 mM to 3.88 mM range; barring one exception. In simply changing the activation method, one can create monodisperse gold nanoparticle colloids of significantly variable average diameter (8.0 – 18.0 nm).

In the next chapter we investigate new routes to the formation of gold nanoparticles from reactions with ketones with auric acid. We investigate four ketones; cyclohexanone, acetone, 3-pentanone and acetylacetone. The first part of the chapter (Section 4.3) deals with the room temperature reaction of cyclohexanone and auric acid. The second part of the chapter (Section 4.4) deals with the MWA reflux of acetone, 3-pentanone or acetylacetone with auric acid. The effect of each ketone on the resulting particle size and shape is assessed and compared. In addition, a viable mechanistic route to the formation of gold from the reaction of each ketone with auric acid is suggested; where the mechanism for the reaction of cyclohexanone and auric acid (Section 4.3) is established in greatest detail.

4. New routes to the formation of gold nanoparticles from reactions with ketones

4.1. Overview

Gold nanoparticles have been synthesised by heating auric acid solutions with a variety of fruit extracts.[73] These fruit extracts contained several ketone functional groups and it may be that these functional groups mediate the formation of multi-shaped nanoparticles. Such multi-shaped gold nanoparticles have been used to investigate the biological toxicity of gold nanoparticles in zebrafish embryos[98] and mammalian cells[99] but are yet to be applied in a functional material. Silver nanoparticles of different shapes and sizes have also been found to induce multi-colour photochromism when bound to TiO_2 surfaces.[28]

The use of ketones in precious metal nanoparticle synthesis has been reported – however, all reported routes required heating and no formation mechanism was proposed. Huang *et. al.* demonstrated how truncated gold nanocubes could be produced using an electrochemical approach and an acetone injection stage.[100,101] Multi-core nanoparticle structures comprised of Pd have been synthesised by Tong *et. al.*[102] This involved the reaction of the Pd acetate salt mixed with ethylene glycol and KOH in a methyl isobutyl ketone solvent and was activated by microwave heating and formed multi-core structures that were ≈ 50 nm wide. The formation of large 2D triangular and hexagonal nanoplates have also been observed. [103–105] By mixing gold seeds with a mixture of CTAB, PEG and the ketone polymer PVP a slow room temperature reaction over 8 hours produced platelet-type particles that were typically ≈ 5 nm thick and ≈ 200 - 500 nm wide. It was also shown by Tsuji *et. al.* that microwave heating (85 °C) of aqueous solutions of auric acid with long-chained PVPs yielded similar structures.[106] Mixing aqueous auric acid solutions with a lemongrass plant extract (*cymbopogon flexuosus*) at room temperature produced nanoplate mixtures with lengths on the micrometer scale, where the directional growth was related largely to the ketone groups present in the extract.[107] In this chapter we will investigate novel routes to gold nanoparticles from reactions of ketones and auric acid, where the ketone will act as both the reducing agent and surfactant.

4.2. Introduction

To our knowledge, the simple reaction (either at room temperature or at reflux) of a common ketone with aqueous auric acid has not been studied. In this chapter four common ketones were investigated including cyclohexanone, acetone, 3-pentanone and acetylacetone. We found that in all cases gold nanoparticles were formed. In the case of cyclohexanone, no heating was required for the reaction to initiate. However, in the case of the remaining three ketones, heating under reflux was necessary to activate the reaction. The chapter is thus separated into two parts. Section

4.3 deals with the room temperature reaction of cyclohexanone and auric acid. Section 4.4 deals with the microwave induced reflux of acetone, 3-pentanone or acetylacetone with auric acid. The effect of each ketone on the resulting particle size and shape is assessed and compared. In addition, viable mechanistic routes are suggested.

4.3. The reaction of cyclohexanone and auric acid at room temperature

4.3.1. Overview

A new method for the synthesis of gold nanoparticles from the addition of cyclohexanone to aqueous solutions of auric acid at room temperature is presented. By understanding this process we have discovered new organic chemistry for the transformation of cyclic ketones to α-chloro ketones. Contrary to conventional gold nanoparticle syntheses, the reaction "self-activates" at room temperature and forms an increasingly red solution over ≈ 60 mins. By studying the gold colloid's formation using transmission electron microscopy we saw how large multi-core (63 ± 21 nm diameter) structures made of clustered particles (6.4 ± 1.3 nm) were initially formed. These multi-core structures then compacted into an array of denser shapes that slowly increased in size until the reaction was complete. The most prominent shapes formed were primarily spherical (43 ± 6.8 nm); other more distinct shapes included dodecahedra (39 ± 10 nm), triangular (≈ 50 nm in height) and hexagonal (≈ 70 nm wide) nanoplates. The solution was stable to precipitation for over 3 months. During this period the nanoplate structures substantially increased in size (triangular ≈ 250 nm, hexagonal ≈ 320 nm) whereas other structures showed no further growth. X-ray diffraction studies demonstrated that the gold nanoparticles were crystalline. The formation of the 2-chlorocyclohexanone by-product was observed in solution phase ^{13}C NMR, gas phase chromatography and IR spectroscopy. A mechanism was suggested to account for this by-product and the reduction of auric acid to gold.

4.3.2. Introduction

To our knowledge, the use of cyclohexanone in initiating a self-propagating gold nanoparticle formation reaction has not previously been reported. Nevertheless, Biswas *et. al.* did use cyclohexanone/ water/ isopropanol mixtures in synthesising a range of copper based nanoparticles[108] and Sarkhosh *et. al.* used cyclohexanone as solvent and capping agent for forming gold nanoparticles through laser ablation of a submerged gold target.[109] Marin *et. al.* demonstrated how aryl ketones can photocatalytically reduce solutions containing Au^{3+} to Au^{0}.[110] The growth mechanisms for traditional gold nanoparticle formation methods have been investigated using *in situ* monitoring methods such as UV-visible spectroscopy, dynamic light scattering, electrode potential measurements or by TEM imaging sample aliquots at set times during the reaction.[78,79]

In this section we will show how cyclohexanone reacts with auric acid and causes a "self-activated" room temperature nanoparticle formation reaction to commence. During this reaction the particles undergo several shape changes. Initially, large multi-core structures composed of smaller aggregates form that later compact primarily into spherical particles and alternative 3D structures such as triangular prisms and dodecahedrons and large flat 2D hexagonal and triangular nanoplates. We also provide an insight into the reaction mechanism through determination of reactions by-products. This new method of multi-shaped nanoparticle synthesis is reproducible and, to our knowledge, one of the simplest ever reported in that it involves no heating/ external activation, occurs at room temperature and requires just one step (simply mixing aqueous auric acid with cyclohexanone). Furthermore, the nanoparticles formed (unlike some methods) do not precipitate from solution and appear to be indefinitely stable as stored at room temperature.

4.3.3. Experimental

All reagents were purchased from Sigma-Aldrich UK. All glassware was washed with aqua regia and rinsed with copious amounts of deionised water before use. All reactions were performed in beakers.

4.3.3.1. Synthesis

The nanoparticle solution was made by mixing auric acid ($HAuCl_4.3H_2O$ - 0.85 mg, 0.28 mM) in distilled water (9.5 ml) with cyclohexanone ($(CH_2)_5CO$ – 0.50 ml, 0.47 g, 0.48 M). This solution did not require thermal activation (or any alternative energy source). This “self-activated” led to the formation of gold nanoparticles throughout the solution when conducted under room light or in a dark cupboard, as indicated by its colour change to a red-coloured solution. A further experiment was conducted where the cyclohexanone was added gently onto the surface of the aqueous auric acid solution, forming a separate organic layer due to immiscibility of the two solvents. In this case, the nanoparticle formation reaction occurred only at the interface of the two solvent layers as judged by the diffusive change in colour (from red at the interface spreading down into the solution with time). The effect of temperature on the reaction was investigated by mixing auric acid (2.6 mg, 0.28 mM) in distilled water (28.5 ml) with cyclohexanone (1.5 ml, 1.4 g, 0.48 M) at ≈ 20, 30, 40, 50 and 60 °C. After heating the aqueous auric acid solution to the desired temperature, the cyclohexanone reducing agent was injected, causing a thorough mixing of the two immiscible solutions forming an emulsion. The rate of consumption of auric acid in the reaction was determined by titrating solution aliquots during the reaction.[111] This was achieved by scaling the reaction up by a factor of 5 and taking 2 ml aliquots out every 5 mins for analysis. The nanoparticle formation reaction was quenched as soon as the aliquots were extracted by addition of excess KI (0.02 g). This caused all auric acid present within the aliquot to be consumed to AuI, forming an I_2 side-product. The level of I_2 formed, and thus the amount of auric acid originally present, was measured by titration against $K_2S_2O_3$ (1 mM) using potato starch indicator (0.02 g), where the disappearance of blue-black colour indicated a complete reaction of $K_2S_2O_3$ with I_2.

4.3.3.2. Analysis

The size and shape of nanoparticles formed at room temperature by rapid mixing of the solution were investigated using transmission electron microscopy (TEM) using a Jeol 4000EX HRTEM device. Solution aliquots were taken out from the nanoparticle reaction after 5, 20 and 65 mins of reaction and placed onto lacey carbon-coated copper grids and allowed to air dry before being investigated by TEM.

Nanoparticles solutions formed at room temperature by rapid mixing were freeze dried to remove the aqueous solvent and any excess cyclohexanone to form a nanoparticle powder. The powder was analysed by X-ray diffraction (XRD) using a micro-focus Bruker GADDS powder XRD with a monochromated CuK_α (1.5406 Å) source and CCD area detector. After mixing the powder within a pressed KBr disc, the infrared (IR) spectrum of the solid was taken using a Perkin Elmer RX-I instrument.

Nanoparticle solutions were centrifuged on a Beckman Coulter Avanti Centrifuge J-26 XP at 20,000 rpm (≈ 48,000 g) causing the gold particles to rest at the bottom of the solution. The liquid layer above was removed and passed through a gas chromatograph (Clarus 500, PerkinElmer) equipped with flame ionisation detector and 30 m capillary column (Ellite-1, cross-bond 100% dimethyl polysiloxane) and compared with standards to elucidate the reaction by-products. The gases released from the nanoparticle reaction were analysed by IR spectroscopy and compared with the pure gas phase spectra of cyclohexanone and 2-chlorocyclohexanone. This was done by casting 1 mL of the nanoparticle reaction solution at the base of an IR gas cell, and then gently placing under vacuum. Three samples were examined by both ^{1}H and ^{13}C nuclear magnetic resonance (NMR) spectroscopy using a Bruker AV600 (600 MHz) instrument: (i) a gold nanoparticle solution (diluted by a factor of 100) formed from the reaction of auric acid and cyclohexanone in D_2O at room temperature, (ii) cyclohexanone in D_2O and (iii) 2-chlorocyclohexanone in D_2O.

4.3.4. Results and discussion

The self-activated formation of gold nanoparticles was induced by reacting a thousand fold excess of cyclohexanone with aqueous solutions of auric acid at room temperature. Several photographs were taken at set time intervals during the self-activated nanoparticle formation reaction, as displayed in Figure 4.3.4.1. Two reactions were studied; (i) the mixing of cyclohexanone with auric acid and (ii) the layering of cyclohexanone on top of the aqueous auric acid layer. In the case of thorough pre-mixing of the cyclohexanone reducing agent with the auric acid solution (Figure 4.3.4.1(a)) no colour change was observed until after ≈ 10 mins when the solution turned a slight pink. This colouration became more intense as the reaction proceeded. After ≈ 40 mins of reaction

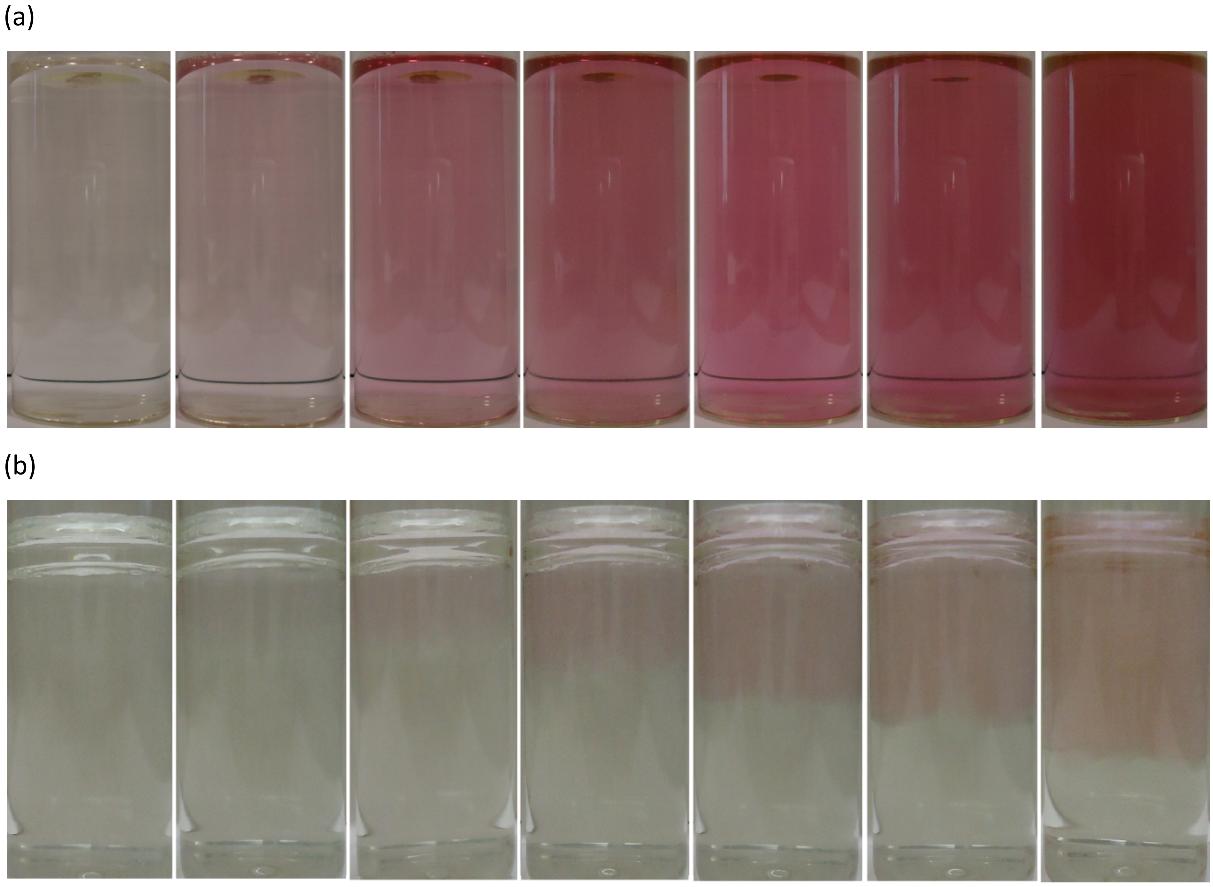

Figure 4.3.4.1: A series of images of the same solution taken at time intervals of 0, 10, 20, 30, 40, 50 and 60 mins reaction time (from left to right) in the self-activated gold nanoparticle formation reaction of auric acid solution with cyclohexanone that was (a) shaken into the solution or (b) layered gently on top of the aqueous layer.

the solution appeared purple and was more strongly coloured. After ≈ 60 mins of reaction, the solution did not further deepen in colour, signifying the end of the gold nanoparticle formation reaction. When the solution was viewed off-angle, a two-tone effect was revealed where the solution showed a more orange tone when viewed at high angles and a more purple tone when looked at directly.

In the case of the gentle layering of cyclohexanone at the surface of the aqueous auric acid solution, an emulsion layer was formed at the interface in which the colour-change and hence nanoparticle formation reaction occurred solely at the cyclohexanone-water interface. Figure 4.3.4.1(b) shows that just after addition of the reducing agent (0 mins), two separate immiscible layers can be observed. Approximately 20 mins into the reaction a pink layer began to form within the aqueous layer at the interface. As the reaction progressed, the pink layer deepened in colour and penetrated deeper into the aqueous layer as the nanoparticles diffused. After 60 mins of reaction, almost half of the aqueous layer had turned pink. On comparing the two reactions, one can see by eye that the nanoparticle formation is more rapid in the solution that was thoroughly mixed. However, one can also infer the importance of the partial miscibility of the cyclohexanone on the mechanism of nanoparticle formation.

The nanoparticle formation reaction, where the cyclohexanone initiator was well-mixed, was also followed using UV-visible spectroscopy over the 190 – 1100 nm range, as shown in Figure 4.3.4.2. The spectra showed the formation of a band at 540 – 575 nm corresponding to the surface plasmon resonance (SPR) of Au nanoparticles. The UV-visible spectrum was taken every ≈ 70 seconds until the SPR band stopped increasing. Approximately 10 mins after the cyclohexanone was added a SPR band started to appear. This continued to increase at a relative steady rate until after ≈ 65 mins after cyclohexanone addition, when the SPR band suddenly stopped increasing in magnitude. The overall baseline also increased its absorbance during the process – this stopped its upward shift at the same time as the SPR band showed no further increase in magnitude.

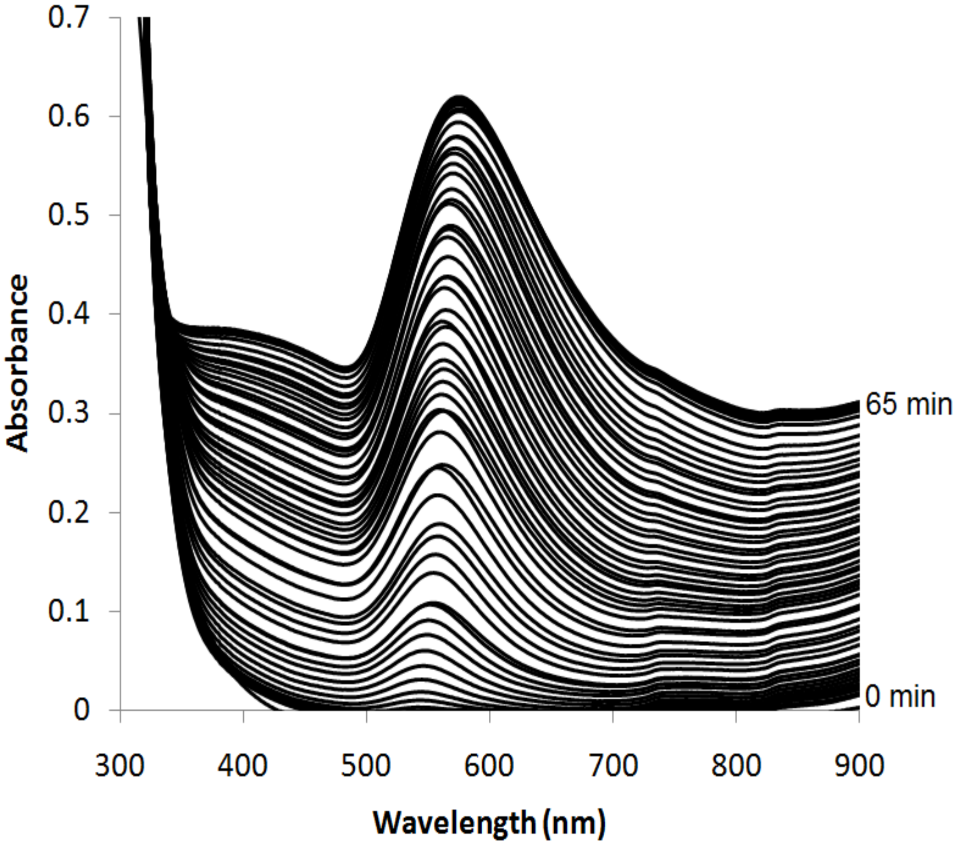

Figure 4.3.4.2: UV-visible spectrum monitoring the growth of gold nanoparticles *in situ* during their self-activated formation from the reaction of an aqueous auric acid solution with cyclohexanone. Each spectrum was taken every 70 seconds where the plasmon band appeared ≈ 10 mins after the addition of cyclohexanone. The spectra are shown as recorded and no shift was applied to the baseline.

The centre (nm) and height (absorbance) of each progressively growing SPR band was extracted and plotted against reaction time (minutes), as shown in Figure 4.3.4.3. As observed in UV-visible absorbance spectra, an SPR band (543 nm, 0.01 absorbance units) first appeared 10 mins after the addition of cyclohexanone. The SPR band then grew in height at a relatively steady rate of roughly 0.012 absorbance units per minute. The centre of the SPR also shifted to longer wavelengths. These two properties continued to increase until exactly 64 mins after the addition of cyclohexanone, where they both reached a plateau. From 64 to 75 mins reaction time both the SPR centre and height did not change significantly. Over the reaction period the SPR height increased from 0 to 0.61 absorbance units. In addition, the SPR centre shifted from 543 to 576 nm. The solutions were highly stable to precipitation and altered little after being stored for 3 months, although the SPR centre decreased to 563 nm and the absorbance dropped to 0.59.

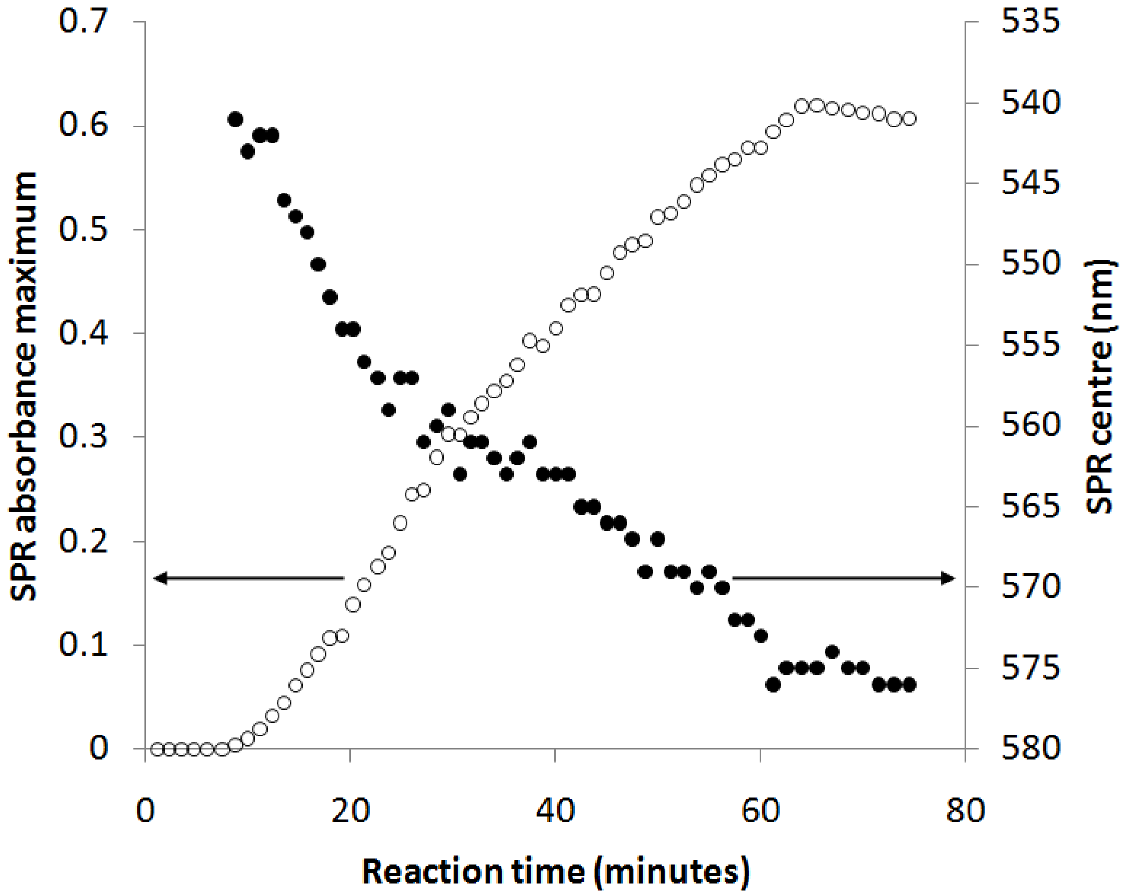

Figure 4.3.4.3: A plot of the centre (nm) and height (absorbance) of the progressively growing surface plasmon resonance band extracted from UV-visible spectra monitoring the growth of gold nanoparticles *in situ* during their self-activated formation reaction from auric acid solution and cyclohexanone.

It is well known that an increase in SPR centre wavelength signifies an increase in average nanoparticle size.[77] Using the relationship derived by Haiss *et. al.*,[112] the increase in SPR centre from 543 to 576 nm signifies an average increase in nanoparticle diameter of ≈ 34 nm, assuming the particles are predominantly spherical.

The rate of consumption of auric acid in the reaction was determined by titrating solution aliquots during the nanoparticle formation reaction.[111] The level of auric acid was found to decrease linearly over the time period (Figure 4.3.4.4); decreasing from 0.26 mM at the start of the reaction (0 minutes) at a rate of 6.2 µM.min^{-1} to there being no presence of auric acid after 45 mins of reaction. This was in contrast with nanoparticles formed by the reaction of auric acid and citric acid (the Turkevich method), where during the reaction a sharp change in auric acid concentration is observed at a critical point.[79] From our spectroscopic studies it was observed that surface plasmon band formation, indicating the formation of gold nanoparticles, terminated after ≈ 65 mins of reaction, whereas our titrations showed that the auric acid was depleted after 45 mins. This showed that there was a 20 minute lag between the complete reduction of gold ions and their subsequent growth to form nanoparticles at room temperature.

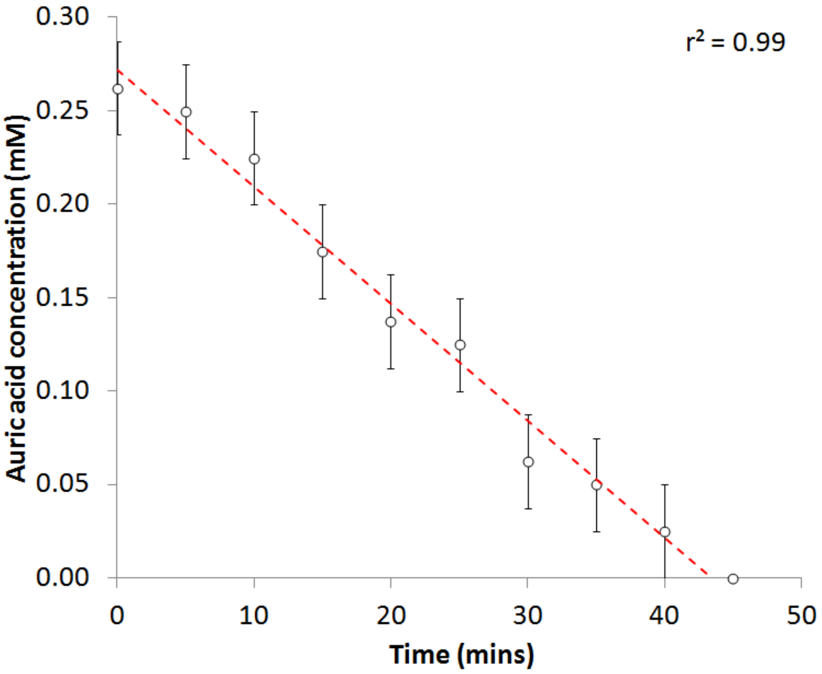

Figure 4.3.4.4: Auric acid (mM) depletion in the self-activated gold nanoparticle formation reaction of auric acid (0.28 mM) with cyclohexanone (0.48M). This was measured by quenching the reaction in sample aliquots with iodide salt and measuring the level of I_2 side-product by titration with thiosulphate using starch indicator. The decrease in auric acid concentration was strongly linear (r^2 = 0.99).

The gold nanoparticle formation reaction was repeated with solution aliquots being extracted 5, 20 and 65 mins after the addition of cyclohexanone and placed on lacey carbon-coated copper grids for TEM analysis. Representative TEM images are shown in Figure 4.3.4.5. Figure 4.3.4.5(a) shows that after 5 mins of reaction multi-core structures had formed, which ranged in size from 20 to 93 nm in diameter. The average diameter and standard deviation of these multi-core structures was 63 ± 21 nm. On closer inspection it can be seen that these multi-core structures are composed of clusters of smaller particles. These particles were predominantly spherical and ranged in size from 4.0 to 10 nm. The average diameter and standard deviation of the spherical particles of which the multi-core structures were composed was 6.4 ± 1.3 nm. Figure 4.3.4.5(b) shows a less magnified image of the same sample. Some well formed gold nanoparticles had formed alongside the multi-core structures. Mainly spherical shapes (11 ± 6.7 nm) were observed, however dodecahedral (21 ± 2.1 nm) and rod-like (33 ± 17 nm in length) gold nanoparticle shapes were also present. Intriguingly, large nanoplates (flat structures) were also observed that were mainly triangular in shape (29 ± 12 nm in height). Figure 4.3.4.5(c) shows that after 20 mins of reaction these large multi-core structures had disappeared and only more compact looking and more regularly shaped gold nanoparticles were present. Spherical nanoparticles were still the most abundant shape, but had more than doubled in average size from 11 ± 6.7 nm after 5 mins of reaction to 25 ± 6.4 nm after 20 mins of reaction. Dodecahedral (28 ± 4.7 nm), rod-like (49 ± 23 nm in length) and triangular nanoplate (29 ± 5.3 nm in height) structures were also still present. However, some extra shapes, not previously observed after 5 mins of reaction were now observed, such as decahedra (31 ± 3.9 nm), trigonal bipyramids (35 ± 5.6 nm) and triangular prisms (30 ± 5.2 nm). Figure 4.3.4.5(d) shows the final state of the nanoparticles after they had been allowed to react completely (65 mins total reaction time). Interestingly the size of each shape increased by ≈ 20 nm on average from 20 to 65 mins of reaction. Spheres were still the most predominant shape, increasing in size from 25 ± 6.4 nm to 43 ± 6.8 nm.

The colloids were stable to precipitation on prolonged storage (at least 3 months). A TEM image size analysis of such a solution after 3 months of storage demonstrated how little the predominantly spherical nanoparticles changed in size (49.8 ± 9.5 nm). However, the primarily flat nanoplate structures showed an almost 5-fold increased in size (Figures 4.3.4.5(e) and 4.3.4.5(f)). These nanoplates were similar in size and shape to those formed by Tsuji *et. al.* from the microwave heating (85 °C) of aqueous solutions of auric acid with long-chained PVPs.[106]

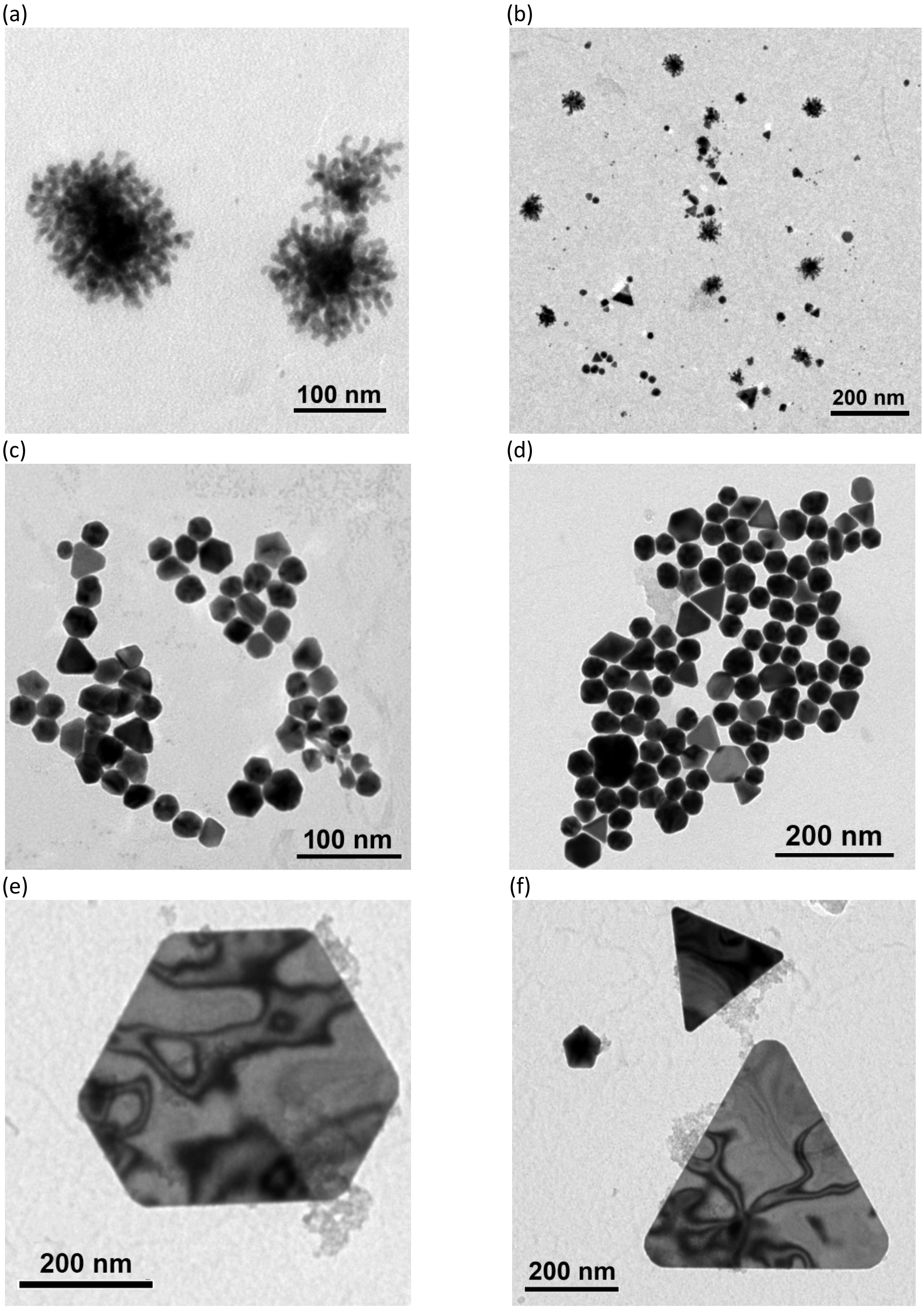

Figure 4.3.4.5: TEM images of solution aliquots taken from the self-activated gold nanoparticle formation reaction of auric acid solution and cyclohexanone after (a & b) 5 mins, (c) 20 mins and (d) 65 mins of reaction. After 3 months storage larger (e) hexagonal and (f) triangular nanoplate structures were also present.

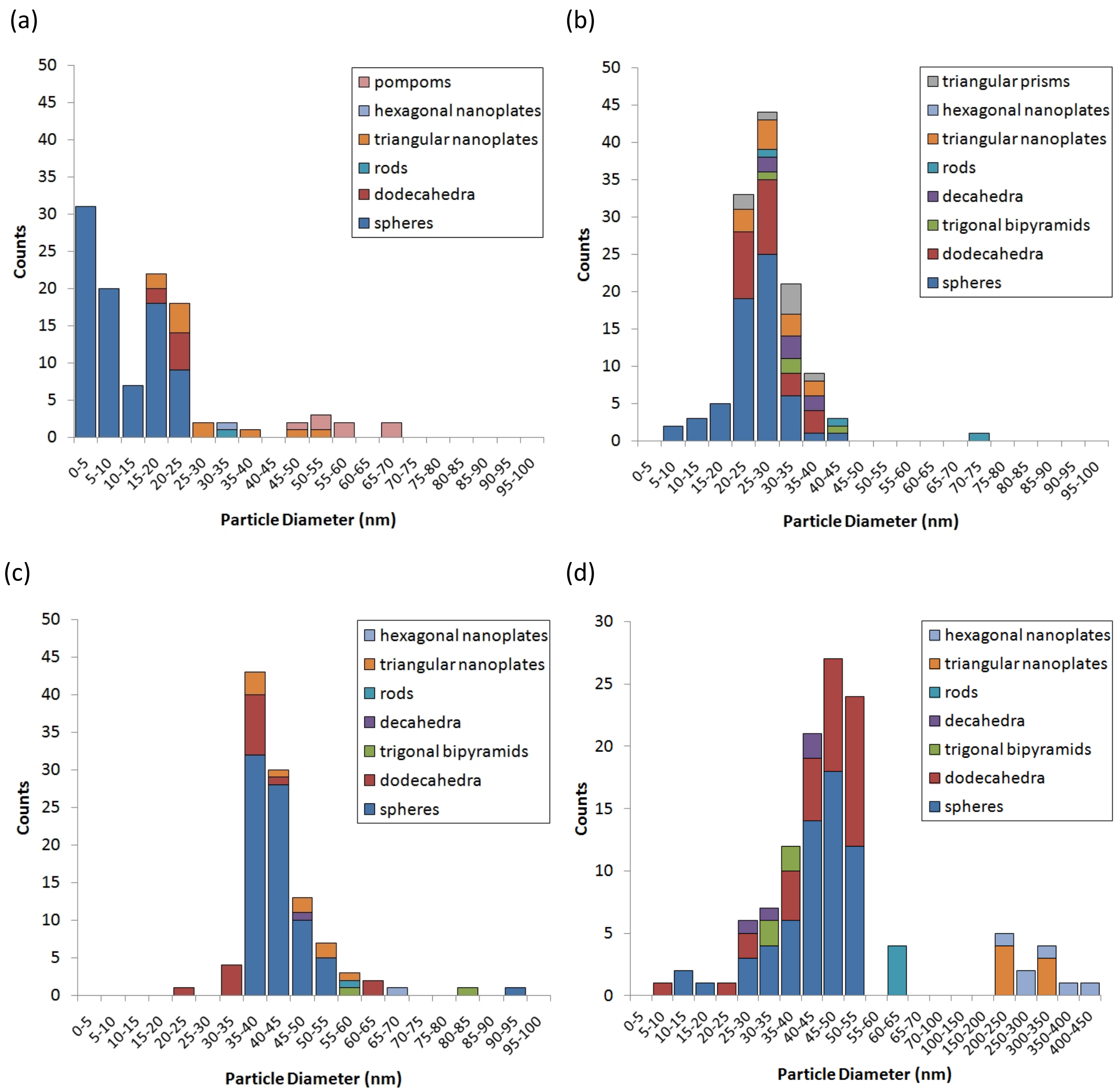

Figure 4.3.4.6: Histogram plots of nanoparticle size (nm) and count for the various nanostructures observed after (a) 5 mins, (b) 20 mins and (c) 65 mins of reaction from the self-activated gold nanoparticle formation reaction of auric acid solution and cyclohexanone and (d) after 3 months storage.

The distribution of nanoparticle shapes and sizes is summarised in the histograms shown in Figure 4.3.4.6. The histogram plots for the nanostructures observed after 20 and 65 mins of reaction and 3 months storage were approximately Gaussian in distribution. The histogram after 5 minutes reaction was very much skewed to the left due to the large number of tiny spherical particles that were present within the large multi-core structures that initially formed. The overall average diameter of all nanostructures increased during the reaction period from ≈ 15 nm after 5 mins, to ≈ 25 nm after 20 mins, to ≈ 40 nm after 65 mins of reaction. After 3 months in storage the average nanoparticle size did not change much, showing how the nanoparticle formation reaction was complete after 65 mins of reaction. Although a multitude of 3D shapes and flat nanoplate structures were observed, spherically shaped nanoparticles were present in majority (70 % presence on average) throughout the reaction. For the duration of the reaction it was observed that the SPR band centre shifted from 543 to 576 nm (Figure 4.3.4.3), denoting an average increase in size of ≈ 34 nm.[112] From TEM studies, a similar size change was observed for the spherical particles that were present in majority, increasing in average size from 11 ± 6.7 nm after 5 mins of reaction to 43 ± 6.8 nm after 65 mins of reaction. This corresponded to a 32 nm average increase in size, correlating well with shifts in SPR band centre (Figure 4.3.4.2).

A gold nanoparticle solution that had been allowed to react to completion (≥ 65 mins) was freeze dried to form a powder for XRD analysis. The pattern, shown in Figure 4.3.4.7, was phase equivalent to that of bulk gold showing face-centred cubic (FCC) symmetry (FM$\overline{3}$M, a = 4.0781 Å).[113] Through fitting the pattern to a Le Bail refined model, a slightly larger unit cell than bulk gold was observed (a = 4.1031 Å), which equated to an average unit cell expansion of 1.5 %. In measuring the relative heights of each diffraction peak, slight preferred growth was observed in the (200) plane. Through applying the Scherrer equation to each diffraction peak, an average crystallite size of 14 nm with a standard deviation of 1.4 nm was observed. This indicates that the particles observed by TEM with average size *ca* 40 nm are in fact on average composed of multiple crystal grains.

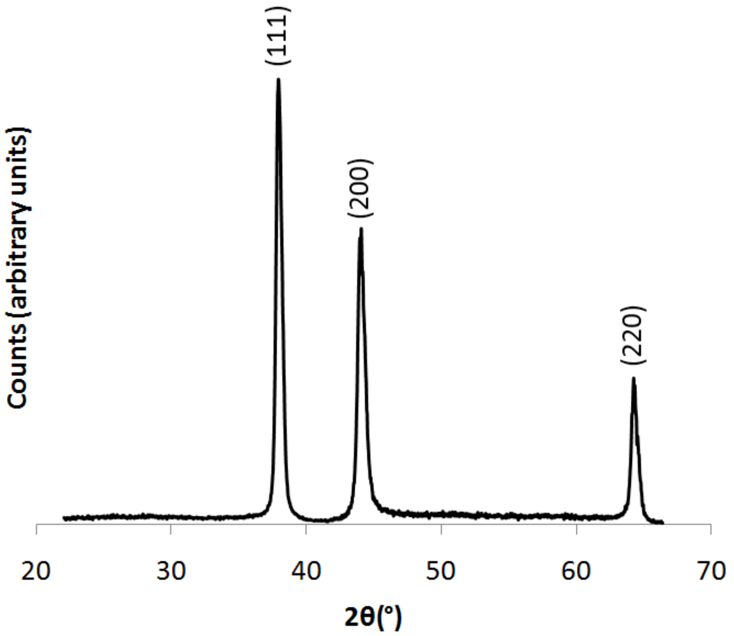

Figure 4.3.4.7: X-ray diffraction pattern of a colloidal powder suspension. The powder was acquired through freeze-drying a gold nanoparticle solution, formed from the self-activated reaction of auric acid solution and cyclohexanone that was allowed to react to completion (> 65 mins).

The freeze dried powder was also investigated using IR spectroscopy within a pressed KBr disc. Cyclohexanone solution was investigated as a standard for comparison. The presence of no organic compound other than cyclohexanone was observed in both spectra. This indicated that cyclohexanone not only acts as a reducing agent in the self-activated formation of gold nanoparticles from auric acid, but also seems to play a surfactant-type role for stabilising these particles. In addition, the carbonyl C=O dimer bond stretch did not shift within error in the gold nanoparticle powder (1714 cm^{-1}) compared with that of pure cyclohexanone (1715 cm^{-1}). In Sarkosh *et. al.*'s IR study of gold nanoparticles formed by ablating a gold target submerged in cyclohexanone solution an ≈ 24 cm^{-1} decrease in this C=O stretch was observed and was attributed to the capping of cyclohexanone molecules to the gold nanoparticles through their C=O bond at oxygen. In comparison, this indicates that either cyclohexanone did not preferentially bind through this functional group to gold in the colloid reported in this paper or that a number of cyclohexanone layers were present, stacking randomly around each nanoparticle.

4.3.5. Mechanistic studies

Gold nanoparticles were formed by simply mixing cyclohexanone with an aqueous solution of auric acid. The reaction took place at room temperature, unlike typical gold nanoparticle syntheses, without the need for any activation *i.e.* thermal activation, sonication, photo-activation *etc*. This ruled out the photocatalytic mechanism observed by Marin *et. al.* with aryl ketones in the reduction of auric acid (Au^{3+}) to gold (Au^0).[110] For our reactions, three components were present in the solution: water, auric acid and cyclohexanone.

The reaction was repeated in D_2O so that any by-products could be examined using and ^{13}C NMR. Several peaks not relating to the presence of the excess reducing agent, cyclohexanone [^{13}C NMR (600 MHz, D_2O) δ(ppm) 25.1, 27.2, 41.8, 128.2, 209.2 {Appendix 1(a)}], were observed. These peaks [^{13}C NMR (600 MHz, D_2O) δ 22.7, 23.9, 33.8, 36.8, 39.2, 41.2, 65.2, 67.0, 95.2, 210.2, 216.3 {Appendix 2}] well-matched a pure spectrum of 2-chlorocyclohexanone [^{13}C NMR (600 MHz, D_2O) δ(ppm) 22.6, 24.7, 27.7, 30.9, 33.8, 37.4, 39.1, 41.2, 65.9, 67.0, 94.9, 210.1, 216.0 {Appendix 1(b)}]. The two missing peaks at δ(ppm) 27.7 and 30.9 of 2-chlorocyclohexanone were masked by the large presence of cyclohexanone in this region. Additional peaks of lower intensity were observed but not identified. Nevertheless, the majority by-product was identified as 2-chlorocyclohexanone. This was supported by gas chromatography measurements. Gas chromatography of the nanoparticle solution (containing the by-product) and clean measurements of pure 2-chlorocyclohexanone were performed. Two matching peaks at the same retention time of 17.9 mins were observed. Further clarification of 2-chlorocyclohexanone being formed was found by IR spectroscopy. Measurements of the gas phase taken during the nanoparticle formation reaction in a gas-tight vacuum-pumped cell showed the progressive release of 2-chlorocyclohexanone (Figure 4.3.4.7). A maximum concentration of 2-chlorocyclohexanone was reached after approximately 30 mins, in line with titrations that indicated the complete reduction of auric acid in a similar time-frame (Figure 4.3.4.4). Although cyclohexanone possesses a higher vapour pressure (4.5 mmHg, 25 °C) than 2-chlorocyclohexanone (0.28 mmHg, 25 °C), the far poorer solubility of 2-chlorocyclohexanone in water (0.02 $g.L^{-1}$) compared with cyclohexanone (87 $g.L^{-1}$) was perhaps the over-riding factor that led to its observation in the gas phase. Assuming the 1: 1 formation of 2-chlorocyclohexanone from auric acid, 0.32 mg would have formed during the reaction (0.16 mg above the solubility limit in 10 ml of water thus encouraging vaporisation). On the other hand, when mixed thoroughly, cyclohexanone (0.47 g) was fully soluble, being 0.4 g under the solubility limit.

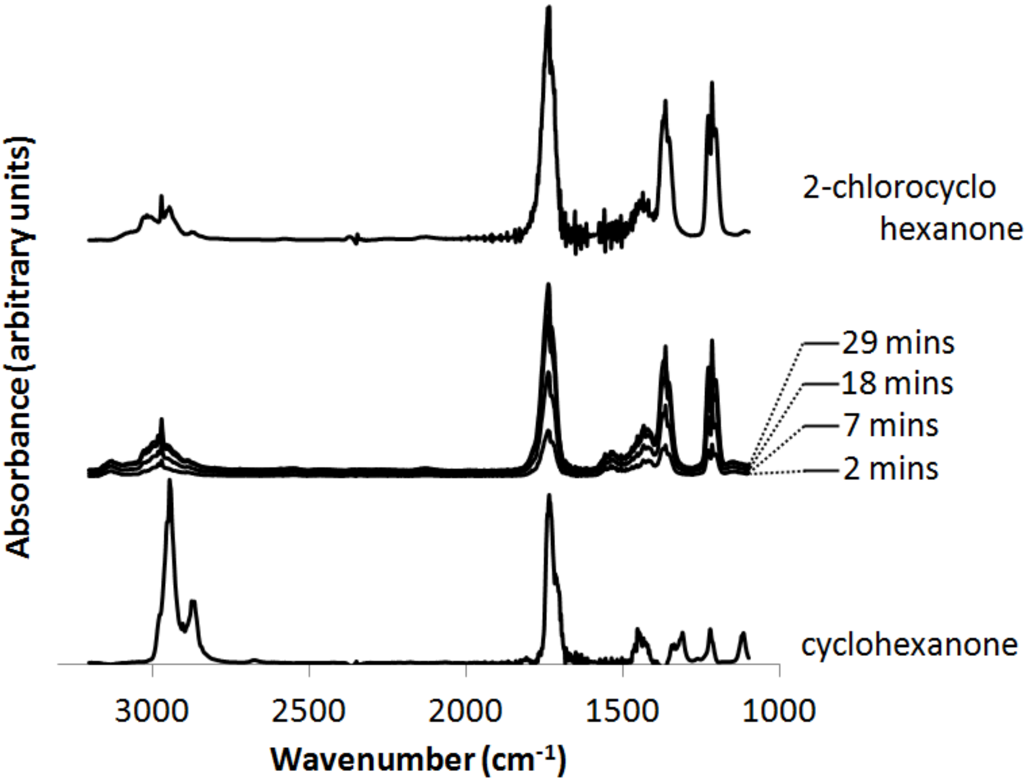

Figure 4.3.4.8: IR spectra of the gas phase above the solution taken during the self-activated gold nanoparticle formation reaction of auric acid (0.28 mM) with cyclohexanone (0.48M). Gas phase measurements of 2-chlorocyclohexanone and cyclohexanone are shown for reference.

The tautomerism of secondary ketones such as cyclohexanone is well known, forming an enol functional group with greater capacity for oxidation.[114] The presence of this tautomer was indicated in this study as aqueous solutions of cyclohexanone discoloured bromine water (indicating an alkene group was present) and turned an acidified solution of $K_2Cr_2O_7$ from orange to green upon slight heating (primary/ secondary hydroxyl group present). In fact, a slight difference in the UV-visible absorption spectrum of aqueous cyclohexanone compared with pure cyclohexanone was observed, when the peak at 913 nm in pure cyclohexanone disappeared in the aqueous mixture.

With the reaction by-product (2-chlorocyclohexanone) and keto-enol chemistry in mind, a mechanism by which Au^{3+} could be reduced to Au^0 is presented (Equation 4.1). The mechanism was based in part on the similar chemistry observed between the pentavalent bismuth salt of $Ph_3Bi(V)Cl_2$ with cyclohexanone that leads to chlorine addition at the α-position on cyclohexanone in a $2e^-$ process forming 2-phenylcyclohexanone.[115] Furthermore, Kochi demonstrated the reaction of $CuCl_2$ with acetone in forming α-chloro ketones, again a $2e^-$ transfer process.[116] To our knowledge, the comparable reaction of auric acid ($HAuCl_4$) and cyclohexanone has not been reported.

Auric acid can release HCl freely in solution, leaving $AuCl_3$ (Equation 4.1a). The acid can tautomerise cyclohexanone to the enol catalytically (Equation 4.1b). Trigonal planar $AuCl_3$ is then nucleophilically attacked by the lone pair on the enol leading to the S_N2 release of Cl^- (Equation 4.1c). The locality of the Cl-Au-O bond to the carbon α-position induces a cyclic nucleophilic attack starting from the alkene bond. This leads to the reduction of gold from Au^{3+} ($AuCl_3$) to Au^{1+} ($AuCl_2^-$) and the formation of 2-chlorocyclohexanone.

$$HAuCl_4 \leftrightharpoons AuCl_3 + HCl \tag{4.1a}$$

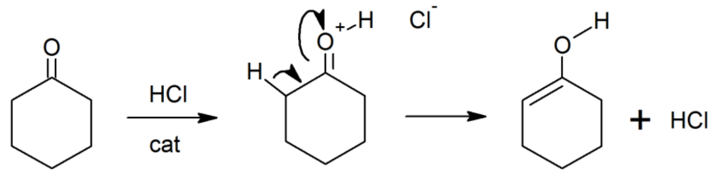

(4.1b)

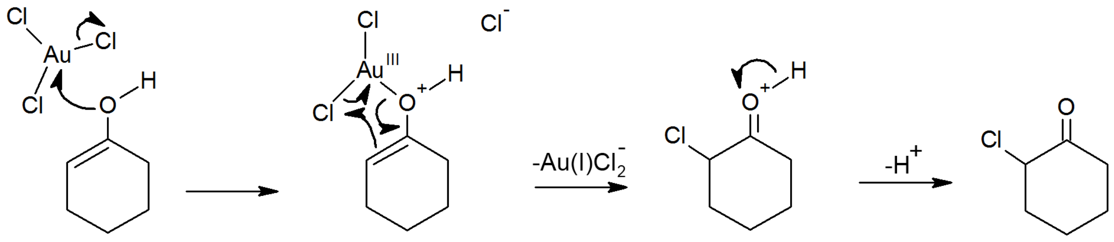

(4.1c)

As the reduction of a metal chloride by a ketone is a $2e^-$ transfer process,[115,116] the direct reduction of $AuCl_2^-$ to Au^0 by cyclohexanone was not possible. Therefore, the disproportionation of $AuCl_2^-$ to Au^0 was the only viable route to Au^0

$$3AuCl_2^- \rightarrow 2Au^0 + AuCl_4^- + 2Cl^- \tag{4.2}$$

According to Gammons *et. al.*, the disproportionation of $AuCl_2^-$ to Au^0 takes place at room temperature.[117] However, the rate of disproportionation increases rapidly with $AuCl_2^-$ concentration and temperature. Moreover, the reaction is catalysed in the presence of Au foil.[117] The fact that Au^0 catalyses the disproportionation of $AuCl_2^-$ to Au^0 indicates that Au^0 growth at Au^0 sites will be favoured, leading to the nucleation and growth of nanoparticles through the continued absorption and disproportionation of $AuCl_2^-$.The sequential steps can be summarised as:

$$3C_5H_{10}CO + 3HAuCl_4 \xrightarrow{-3C_5H_9COCl} 3H^+ + 3HCl + 3AuCl_2^- \rightarrow 2Au^0 + HAuCl_4 + 5HCl \quad (4.3a)$$

and the overall reaction as:

$$3C_5H_{10}CO + 2HAuCl_4 \xrightarrow{-3C_5H_9COCl} 2Au^0 + 5HCl \quad (4.3b)$$

Our TEM studies showed that large multi-core structures initially formed 5 mins into the nanoparticle formation reaction. These structures then collapsed into smaller and denser particles with a variety of shapes. A similar growth mechanism to the formation of gold nanoparticles from auric acid and tri-sodium citrate at 70 – 100 °C observed by Chow *et. al.*[79] Large multi-core particles that were ≈ 100 nm in diameter initially formed that collapsed over the course of the reaction into predominantly spherical shaped nanoparticles that were ≈ 20 nm in size. Such a similarity in growth mechanism demonstrates the similar behaviour of the surfactants in these processes. The gold nanoparticles formed in the reaction of auric acid and cyclohexanone were relatively monodisperse. It was therefore evident that the gold atoms nucleated after the collapse of the multi-core structures to a critical energetically favourable size; with the average diameter of the spherical particles formed being 43 ± 6.8 nm.

4.3.6. Conclusion

A new and perhaps one of the simplest ever method for the synthesis of multi-shaped colloidal gold is presented. By simply adding cyclohexanone to aqueous solutions of auric acid at room temperature a self-activated and self-propagating reaction results in the formation of a gold colloid. Such room temperature self-activated reactions are unique compared with traditional methods (*i.e.* the Turkevich method), where solutions require near boiling temperatures to react. Large multi-core structures initially formed at early stages in the reaction that collapsed into denser particles of a variety of shape and size (though most prominently spheres). The particles were highly crystalline and were stabilised by the presence of cyclohexanone that dually acted as a reducing agent and a surfactant. By identifying the majority by-product, 2-chlorocyclohexanone, a mechanism was proposed. Furthermore, a new method of converting cyclic ketones to α-chloro ketones was discovered. This new synthetic route to colloidal gold is straightforward and fast, forming nanoparticles with a range of shapes. The resulting nanoparticle solution is indefinitely stable to precipitation at room temperature.

In the next chapter we will examine three alternative ketones: acetone, 3-pentanone and acetylacetone. As these ketones did not react at room temperature with auric acid, each reaction was induced by microwave-assisted reflux. The effect of each ketone on the resulting particle size and shape is assessed and compared. Viable mechanistic routes are also suggested.

4.4. The reactions of acetone, acetylacetone or 3-pentanone and auric acid at reflux

4.4.1. Overview

Gold nanoparticles were synthesised from the reaction of auric acid and a ketone at microwave induced reflux. The three ketones examined were acetone, 3-pentanone and acetylacetone. Contrary to the reaction of auric acid and cyclohexanone, these reactions showed no visible sign of reaction when kept at room temperature for several hours; thus the reactions were instigated by thermal stimulation for a brief period of time (between 1.5 to 6.0 mins by microwave-assisted reflux). Reactions with acetone were not complete after the initial reflux period and took several days to complete when stored at room temperature thereafter. These progressive changes were assessed using UV-visible spectroscopy and transmission electron microscopy (TEM). Reactions with acetylacetone and 3-pentanone were primarily complete after the initial reflux period (6 mins).

4.4.2. Introduction

The use of ketones in the synthesis of nanoparticles is uncommon. However, some examples include the use of acetone in the formation of truncated gold nanocubes,[100,101] methyl isobutyl ketone in the formation of multi-core Pd nanoparticles[102] and the ketone polymer poly-vinyl-pyrrolidone (PVP) in the formation of triangular gold nanoplates.[103–105]

In this chapter the use of three common ketones in the formation of gold nanoparticles from auric acid after microwave induced reflux including: acetone, 3-pentanone and acetylacetone is investigated. For reactions with acetone in low concentration we saw several transformations in the particle shape and size before the final product was reached. These transformations were analogous to those underwent by cyclohexanone in Section 4.3. This involved the initial formation of large multi-core structures composed of smaller aggregates (Day 1) that later broke apart and compacted into dense gold particles of varied shape and size (Day 8). Given the similarity in growth mechanism to reactions of auric acid and cyclohexanone (covered in Section 4.3), we propose an analogous pathway to gold. Moreover, the different effect of each ketone on the resulting particle size and shape is assessed and compared. Interestingly, reactions of auric acid with 3-pentanone were complete after 6 mins of reflux, reactions with acetylacetone were almost complete and reactions with acetone were hardly complete taking several days thereafter to end.

4.4.3. Experimental

All reagents were purchased form Sigma-Aldrich UK unless otherwise stated. All glassware was cleaned with aqua regia (3HCl: 1HNO_3) and rinsed with copious amounts of deionised water prior to use.

4.4.3.1. Synthesis

Au nanoparticles were formed from reacting aqueous auric acid (0.28 mM) solutions with a ketone compound under reflux using microwave energy (Proline MicroChef ST22 – 750 W). In each case, the ketone acted as a reducing agent in forming Au nanoparticles (Au^0) from the auric acid (Au^{3+}). Three ketones were studied: acetone, 3-pentanone and acetylacetone (Figure 4.4.3.1).

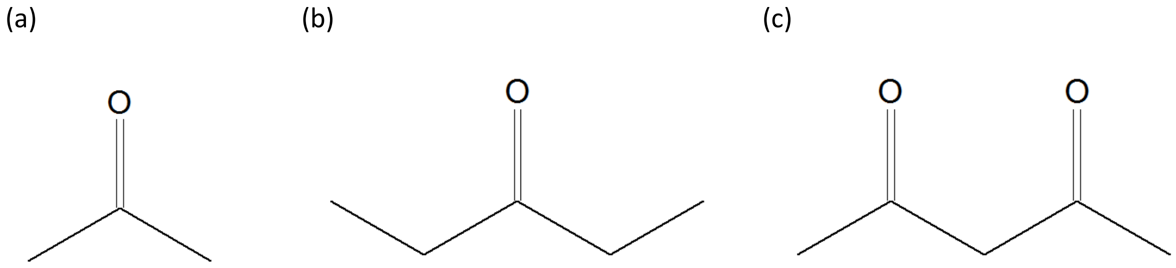

Figure 4.4.3.1: The ketones used as reducing agents in the synthesis of Au nanoparticles from aqueous auric acid solution (0.28 mM) under microwave radiation; (a) acetone, (b) 3-pentanone and (c) acetylacetone.

Table 4.4.3.1: The type of ketone used, volume added, irradiation time (mins) and solution label for a range of aqueous solutions in auric acid (0.28 mM, 10 ml total volume) used to form gold colloids.

	Ketone						
	Acetone					3-Pentanone	Acetylacetone
Volume (ml)	0.5	0.5	0.5	0.5	2.0	0.5	0.5
Irradiation time (mins)	1.5	3.0	4.5	6.0	6.0	6.0	6.0
Solution label	A – 1.5	A – 3.0	A – 4.5	A – 6.0	A* – 6.0	P – 6.0	AA – 6.0

A more in depth study of reactions involving acetone was conducted. This entailed the systematic investigation of microwave time (1.5, 3.0, 4.5 and 6.0 mins) and acetone volume (0.5 or 2.0 ml) in aqueous auric acid (0.28 mM). The total volume of each solution was kept at 10 ml. For reactions involving 3-pentanone and acetylacetone a single reaction was studied which each involved 0.5 ml of the ketone for a microwave time of 6.0 mins. After approximately 45 seconds of microwave radiation the solutions started to reflux, where an almost instantaneous transition from a colourless to bright ruby red solution occurred; indicating the formation of Au nanoparticles. The solutions were continually refluxed using microwave energy for a set period of time. The microwave energy was then turned off and the solution was allowed to cool to room temperature under ambient conditions. The constituents of each solution, microwave time and solution label are listed in Table 4.4.3.1.

4.4.3.2. Analysis

The UV-visible absorption spectrum of each solution was assessed using a PerkinElmer Lambda 25 UV/VIS spectrometer. The size and shape of the particles formed were investigated using a Jeol 4000EX HRTEM microscope. Samples for TEM analysis were prepared by evaporating purified solution droplets onto lacey carbon film coated copper grids.

4.4.4. Results and discussion

Au nanoparticle solutions were synthesised in a one-step process from the reaction of a selected ketone and auric acid under microwave induced reflux. The ketone acted as both the reducing agent and surfactant for stabilising the Au nanoparticles that formed.

4.4.4.1. Acetone as a reducing agent in the synthesis of gold colloids

The UV-visible absorption spectra for the colloids grown using acetone are shown in Figure 1. The effect of leaving the solutions to age under ambient conditions (in the dark) was investigated. Spectra were taken on the day that the nanoparticles were synthesised (Day 1 – Figure 4.4.4.1(a)), 2 days (Day 3 – Figure 4.4.4.1(b)) and 7 days (Day 8 – Figure 4.4.4.1(c)) thereafter. The most distinct changes were observed in Solution A – 1.5.

On Day 1 almost no SPR band was observed (λ = 544 nm, Abs = 0.0034), however, by Day 8 a prominent SPR band was present (λ = 561 nm, Abs = 0.3167). This demonstrated that a post nanoparticle formation reaction took place; an effect similar to the digestive ripening phenomenon observed in our gold nanoparticles formed by the Turkevich method (discussed in Chapter 2). Similarly, the SPR bands of Solutions A – 3.0, A – 4.5 and A – 6.0 also increased in height, but to a lesser degree. This was also attributed to an extended nanoparticle growth reaction. What this showed is that a reaction time between 1.5 to 6.0 mins was insufficient to induce complete nanoparticle growth when 0.5 ml of acetone was used. However, a reaction was instigated that continued at room temperature over several days (something that did not occur in non-refluxed samples). On the other hand, when 2.0 ml of acetone was used in a 6.0 minute reaction we see little change in the SPR band after the first 2 days. This showed how the reaction went to completion when higher concentrations of acetone were used. Interestingly, the SPR absorption maximum began to fall by Day 8, which indicated that the nanoparticles where not wholly stable.

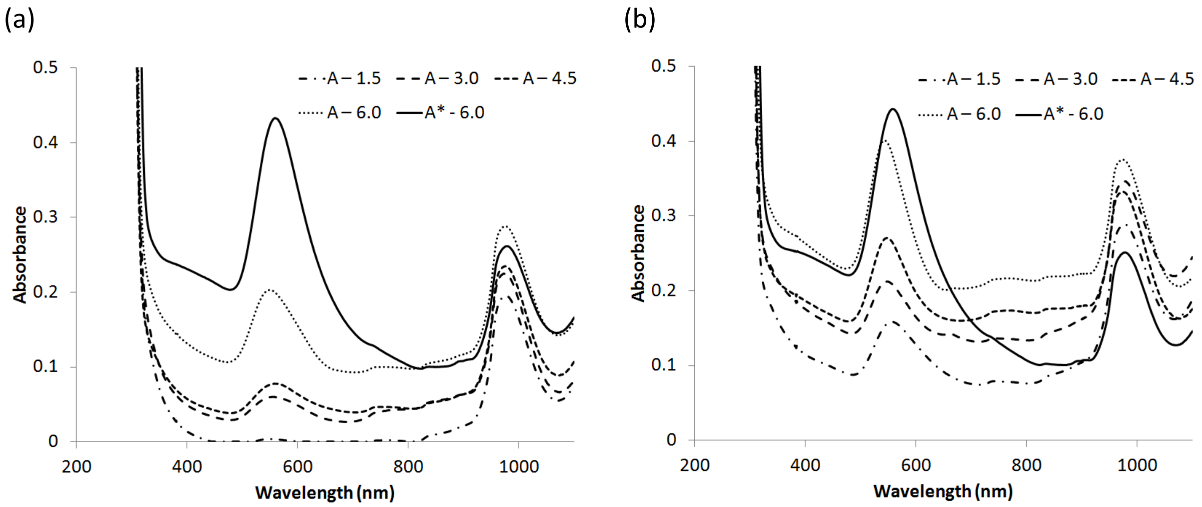

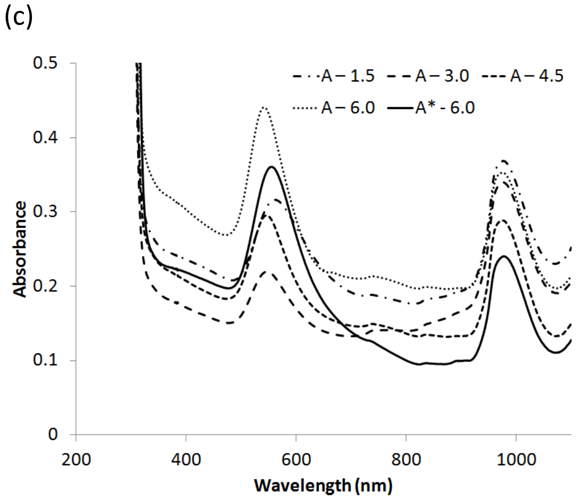

Figure 4.4.4.1: UV-visible spectra at (a) Day 1, (b) Day 3 and (c) Day 8 of gold nanoparticle solutions formed by refluxing auric acid (0.28 mM, 10 ml total volume) with acetone (A = 0.5 ml, A* = 2.0 ml) using microwave energy for 1.5, 3.0, 4.5 and 6.0 mins.

A summary of the changes in SPR centre and absorption are shown in Figure 4.4.4.2. Interestingly little correlation between the SPR band centre and microwave-assisted reflux time was observed over the 7 day storage period (Figure 4.4.4.2(b)). Where the SPR band centre increases from λ = 544 nm (Day 1) to λ = 561 nm (Day 8) for Solution A – 1.5, the SPR band centre decreased by varying degrees for all other solutions. This showed how nanoparticles in Solution A – 1.5 grew in size over the 7 day storage period whereas nanoparticles shrunk in size in the remaining solutions (*i.e.* digestive ripening). The behaviours of Solutions A – 3.0 and A – 4.5 were similar, decreasing from λ ≈ 557 nm to λ ≈ 547 nm over the storage period. The SPR band centres of Solutions A – 6.0 and A* – 6.0 differed quite substantially, irrespective of their shared reflux time, where A – 6.0 ended at λ = 541 nm and A*– 6.0 ended at λ = 555 nm. The change in SPR band centre was minimal in Solution A* – 6.0, decreasing by only ≈ 3 nm over the 7 day storage period.

(a)

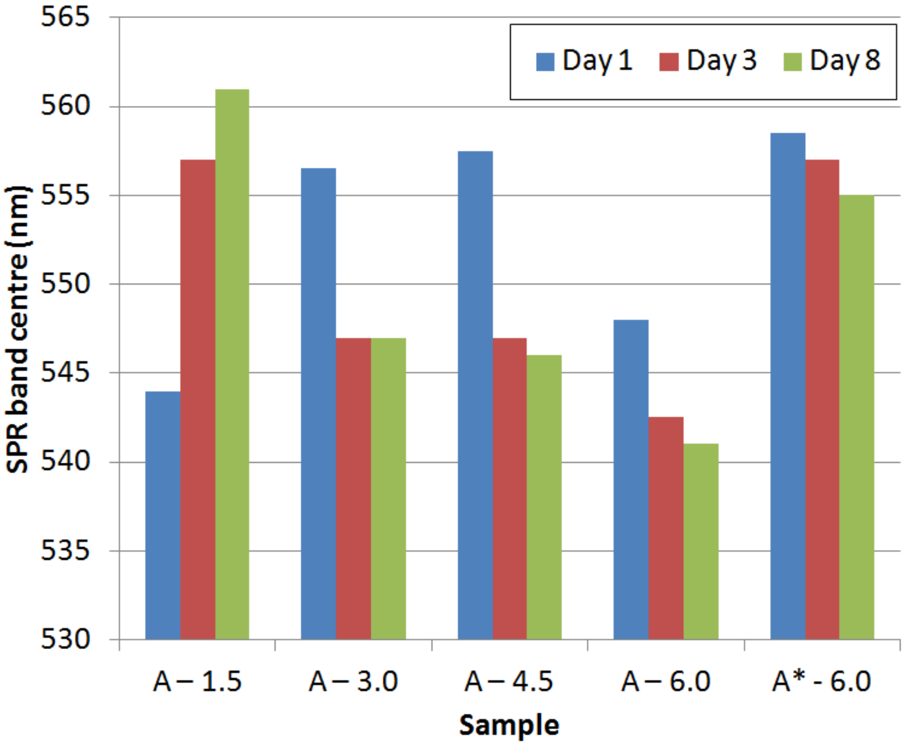

(b)

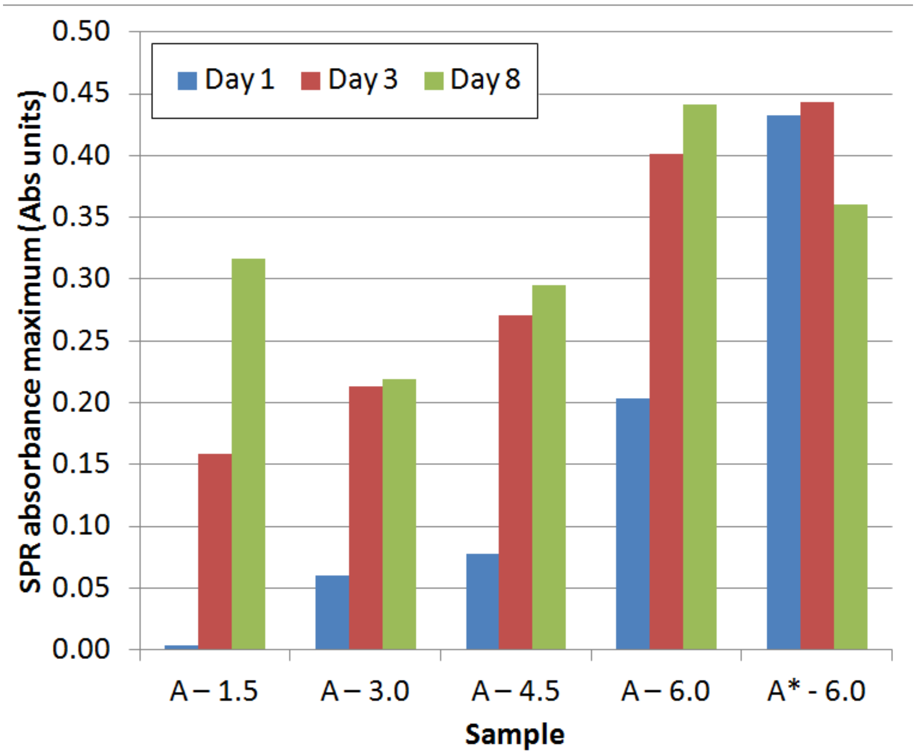

Figure 4.4.4.2: A summary of the changes in the SPR band (a) centre and (b) absorption for the gold nanoparticle solutions formed by refluxing auric acid (0.28 mM, 10 ml total volume) with acetone (A = 0.5 ml, A* = 2.0 ml) using microwave energy for 1.5, 3.0, 4.5 and 6.0 mins.

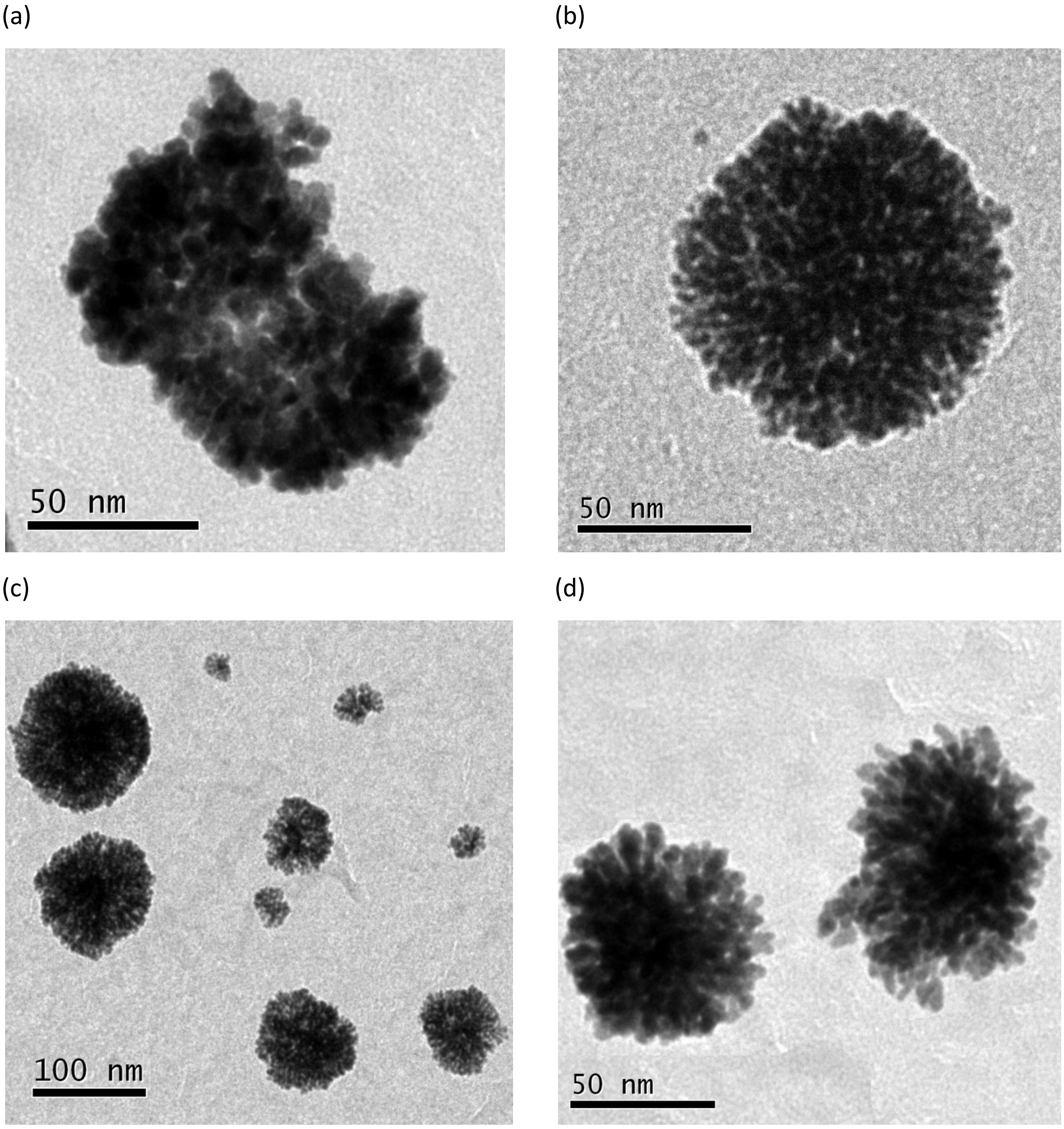

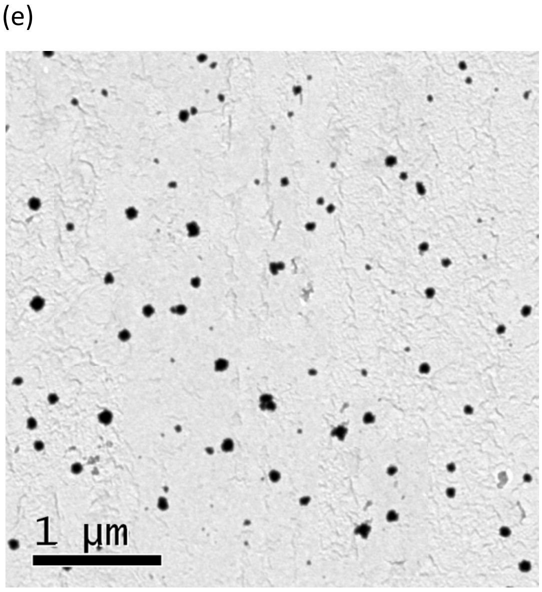

Figure 4.4.4.4: TEM images of gold nanoparticles formed from the reaction of auric acid (0.28 mM, 10 ml total volume) and acetone (0.5 ml) under microwave-assisted reflux for 3.0 (a = A – 3.0), 4.5 (b & c = A – 4.5) or 6.0 mins (d & e = A – 6.0) at Day 1.

The size and shape of the gold nanoparticles formed from reactions with acetone were investigated by TEM at Day 1 and after several weeks of storage in the dark for comparison. Selected images from samples A – 3.0, A – 4.5 and A – 6.0 are shown at various magnifications in Figure 4.4.4.4.

In Solutions A – 3.0, A – 4.5 and A – 6.0 we see a similar formation of large multi-core structures made up of smaller particles. The average diameter of the multi-core structures and the smaller particles were measured (Table 4.4.4.2).

Table 4.4.4.2: Average diameters (nm) of the multi-core nanoparticles and the tiny spherical particles within them. The error is taken as the standard deviation of the measured dataset (N > 50). The SPR band centre is stated for comparison.

	Sample		
	A - 3.0	A - 4.5	A - 6.0
spheres	12.9 ± 6.1	23.0 ± 6.5	11.1 ± 7.5
multi-core (made of spheres)	47.2 ± 28.7	94.3 ± 34.2	69.4 ± 17.2
SPR band centre	557	558	548

By extending the reflux time from 3.0 (A – 3.0) to 4.5 mins (A – 4.5), an increase in average particle size was observed in both the multi-core structures (47.2 ± 28.7 nm to 94.3 ± 34.2 nm) and the smaller spherical particles that they were composed of (12.9 ± 6.1 nm to 23.0 ± 6.5 nm). However, this did not correlate with a substantial shift in the SPR band (557 *vs.* 558 nm). A further increase in the reflux time from 4.5 (A – 4.5) to 6.0 mins (A – 6.0) led to a decrease in average particle size in both the multi-core structures (94.3 ± 34.2 nm to 69.4 ± 17.2 nm) and spheres (23.0 ± 6.5 nm to 11.1 ± 7.5 nm). This decrease in size correlated with a decrease in the SPR centre (558 to 548 nm), as band centres at lower wavelength represent particles of smaller diameter.[112] We see in Figure 4.4.4.4(a), particles in Solution A – 3.0 were far less defined and more elliptical in shape than the particles formed in Solutions A – 4.0 and A – 6.0 (Figure 4.4.4.4). As such, it was assumed that this change in definition (*i.e. crystallinity*) may have altered the relationship between particle size and SPR shift between Solutions A – 3.0 and A – 4.5.

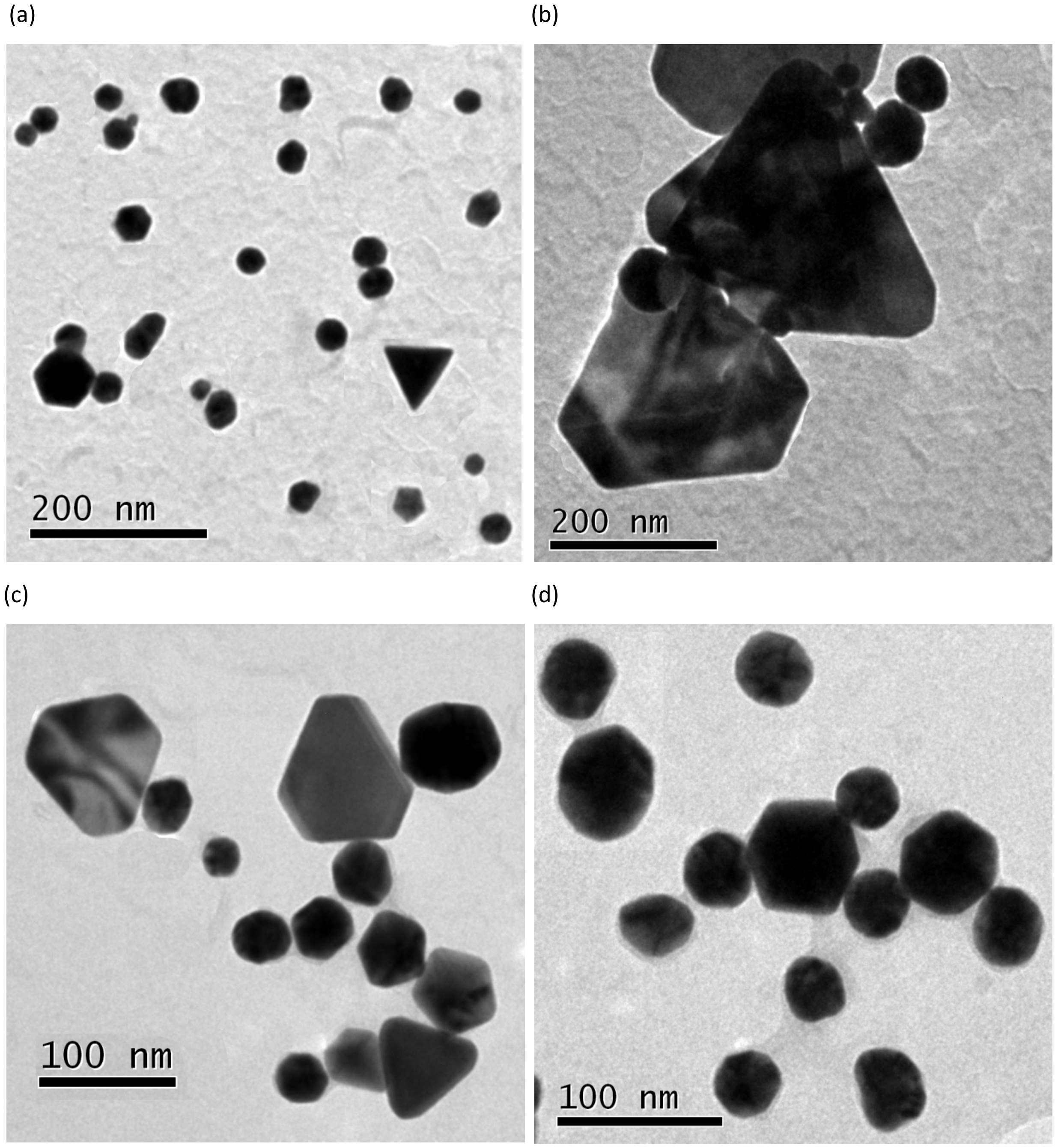

Figure 4.4.4.5: TEM images of gold nanoparticles formed from the reaction of auric acid (0.28 mM, 10 ml total volume) and acetone (0.5 ml) under microwave induced reflux for 3.0 (a & b = A – 3.0) and 6.0 (c & d = A – 6.0) mins at Day 8.

When these particles were stored in the dark, UV-visible spectroscopy revealed a time dependent change in SPR band centre and height. For example, in Solution A – 3.0 the SPR band centre decreased from 557 nm (Day 1) to 547 nm (Day 8) and the SPR band height increased nearly four-fold from 0.06 Abs units (Day 1) to 0.22 Abs units (Day 8). Similarly, in Solution A – 6.0 the SPR band centre decreased from 548 nm (Day 1) to 541 nm (Day 8) and the SPR height more than doubled from 0.20 Abs units (Day 1) to 0.44 Abs units (Day 8). These changes indicated that the

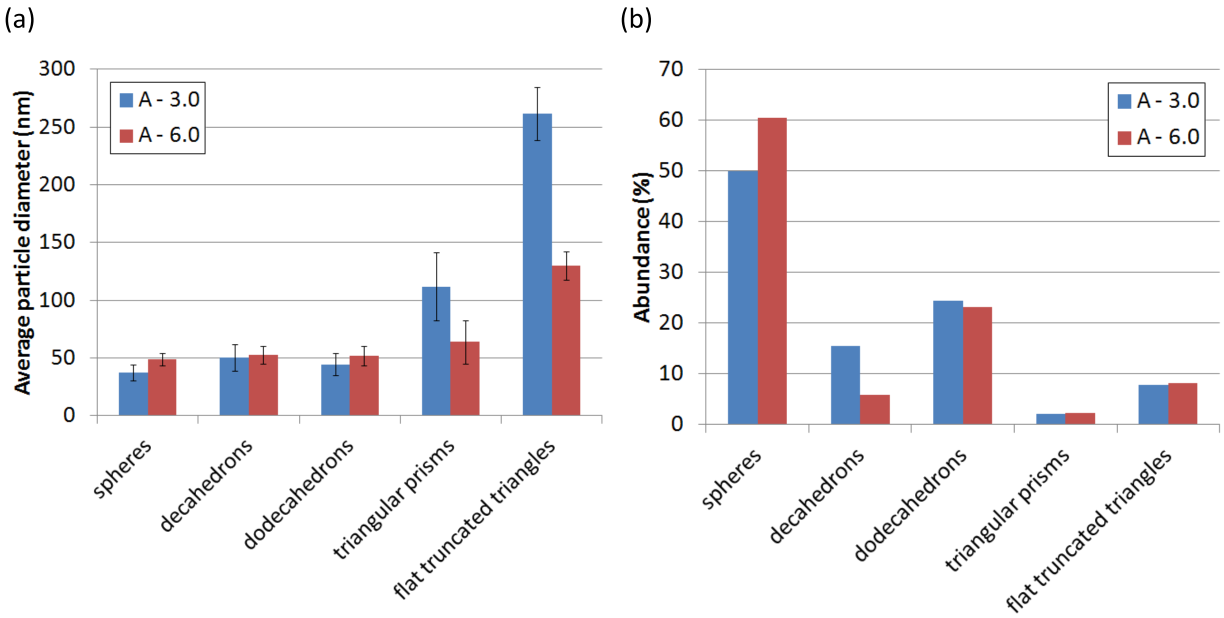

Figure 4.4.4.6: (a) Average particle diameter (nm) and (b) their relative abundances (%) for Solutions A – 3.0 and A – 6.0 at Day 8 (N > 80); gold nanoparticles formed from the reaction of auric acid (0.28 mM, 10 ml total volume) and acetone (0.5 ml) under microwave induced reflux for 3.0 or 6.0 mins respectively.

average particle size decreased in both solutions over the period (inferred from decreases in SPR band centre). Likewise these changes also indicated that the concentration of the colloid was increasing (inferred from increases in SPR band absorbance) and that the nanoparticle formation reaction continued for several days after the short period of reflux. These changes were investigated in more depth by TEM (Figure 4.4.4.5). At day 8, wide-ranging nanoparticle shapes and sizes were observed including spheres, triangular prisms, decahedrons, dodecahedrons and flat truncated triangular structures. This was in stark contrast to the multi-core structures initially observed at Day 1 (Figure 4). The average particle diameter (Figure 4.4.4.6(a)) and abundance (Figure 4.4.4.6(b)) was determined for each solution.

A similar population of each nanoparticle shape was seen across both samples (Figure 4.4.4.6). The most prominent were spheres (50 – 60 %), then dodecahedrons (≈ 25 %), decahedrons (≈ 10 %) and the two types of triangular structure; flat truncated triangles (≈ 8 %) and the triangular prisms (≈ 2 %). This revealed a trend, where particle shapes with a higher number of faces were more abundantly formed. This indicated that multi-faceted structures were more energetically favourable in this system, irrespective of total reflux time (for the range of times investigated). A wide distribution of average particle sizes was observed across both solutions (Figure 4.4.4.5(a)). Comparing the two solutions, the average diameter of spheres, decahedrons and dodecahedrons were similar. However, the average diameter of the triangular prisms and flat truncated triangles

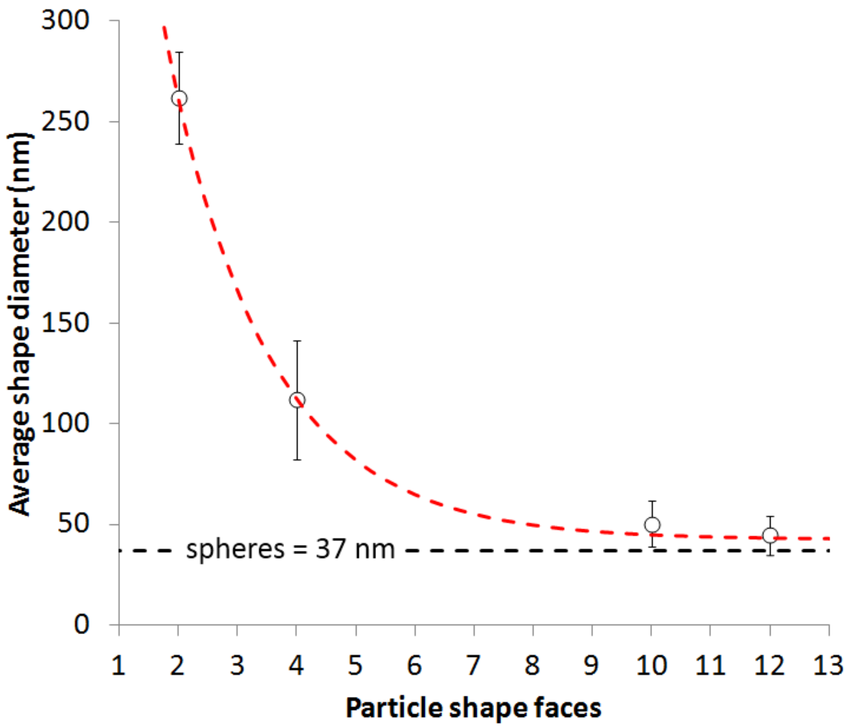

Figure 4.4.4.7: The exponential decay relationship between the number of shape faces for a given particle and its average diameter (nm) for the gold nanoparticles formed in Solution A – 3.0 at Day 8 (r^2 = 0.99); formed from the reaction of auric acid (0.28 mM, 10 ml total volume) and acetone (0.5 ml) under microwave induced reflux for 3.0 mins.

differed substantially, almost halving in size from Solution A – 3.0 to A – 6.0. The spheres were smallest on average in both samples, although marginally larger in Solution A – 6.0 (49 ± 5 nm *versus* 37 ± 7 nm). The next smallest shape was the dodecahedrons (≈ 45 nm) and then the decahedrons (≈ 50 nm). The triangular structures were substantially larger; the prisms ranging in size between ≈ 60 – 120 nm and the flat truncated triangles between ≈ 130 – 260 nm. Interestingly, this revealed another trend, where the average particle diameter increased with a lower number of particle shape faces. This relationship is shown diagrammatically in Figure 4.4.4.7 for Solution A – 3.0.

A first order exponential decay relationship was revealed with good correlation (r^2 = 0.99) where:

$$< diameter\ (nm) > = \ 686\ e^{\frac{-n^{\circ}\ faces}{1.75}} + 42.8 \qquad \text{(Eq 4.4)}$$

The relationship between the number of shape faces and the eventual size was most likely controlled by the particle formation mechanism. At Day 1 large multi-core nanostructures (≈ 50 – 100 nm in diameter) composed of smaller spherical units (≈ 10 – 20 nm in diameter) were formed. These were formed during microwave-assisted reflux for a set period of time (between 1.5 – 6.0

mins). When stored for 1 week in the dark, the particles evolved, changing dramatically in size and shape in forming a range of structures from dense spheres to flat truncated triangles. This was only observed when the solutions had been refluxed, where solutions kept at room temperature showed no observable reaction. The initial period of reflux instigated a chain reaction that continued over a period of several days, which demonstrated the requirement of an activation energy barrier to be surpassed before the reaction could proceed. This was averse to reactions with cyclohexanone (Section 4.3), which proceed at room temperature.

In order to see if the nanoparticle formation reaction with acetone was dependent on the ketone concentration, the experiment was repeated for a 6 minute reflux with 4 times the amount of acetone (Solution A* – 6.0). The SPR absorbance maximum increased over the period of 1 week storage for the solutions of lower concentration. However, in Solution A* – 6.0 the SPR absorbance reached its maximum at Day 1. This showed that the reaction was complete immediately after reflux; in contrast to the other solutions that required aging to complete. The size and shape of the particles formed immediately after reflux was investigated by TEM (Figure 4.4.4.8). The particles observed at Day 1 in Solution A* – 6.0 were similar to those observed at Day 8 in Solution A. The large multi-core structures observed at Day 1 in Solution A were not observed. This showed that when the acetone concentration was quadrupled the nanoparticle formation reaction progressed far more rapidly, reacting to completion during the period of microwave-assisted reflux. The shapes and sizes of the nanoparticles formed in Solution A* were very similar to those formed in Solution A.

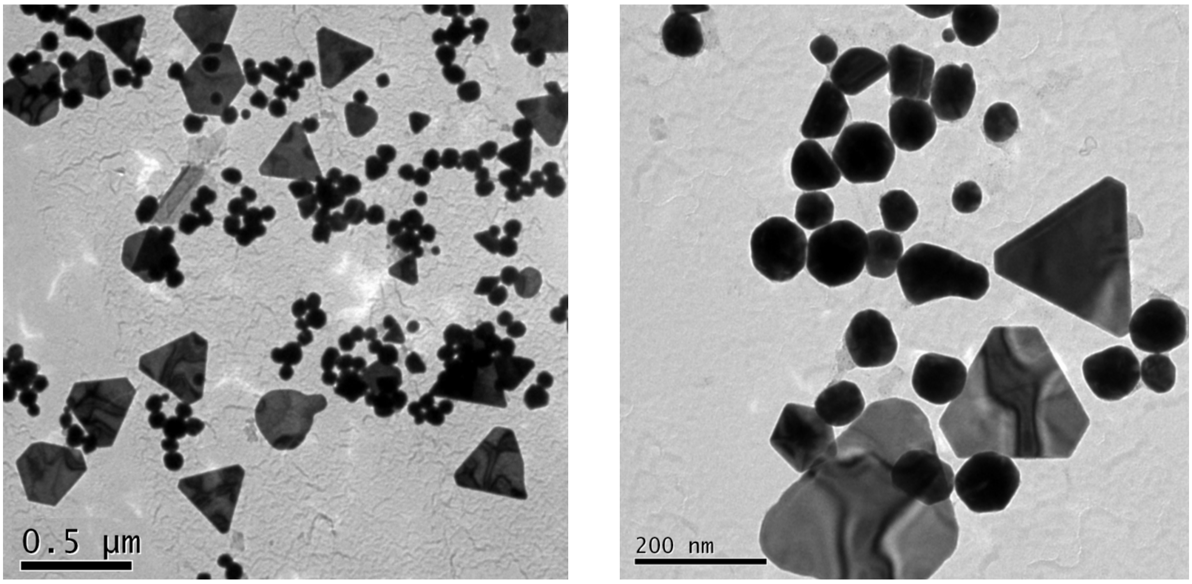

Figure 4.4.4.8: TEM images of gold nanoparticles formed from the reaction of auric acid (0.28 mM, 10 ml total volume) and acetone (2.0 ml) under microwave induced reflux for 6.0 mins (Solution A* – 6.0) at Day 1 immediately after reflux.

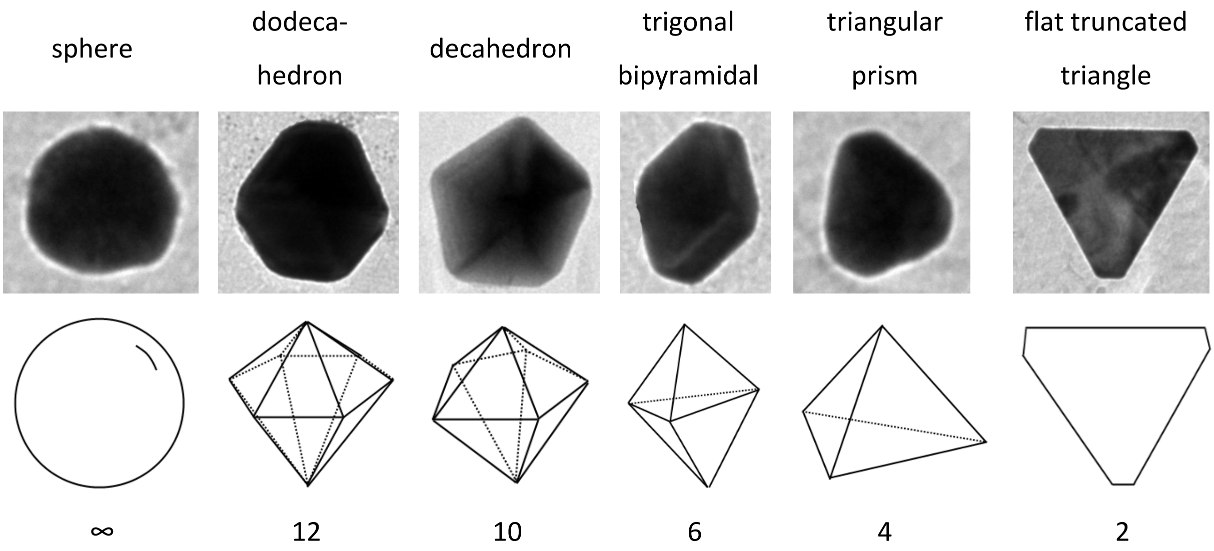

Figure 4.4.4.9: The spectrum of shapes observed in Solution A* – 6.0 at Day 1; a gold nanoparticle solution formed from the reaction of auric acid (0.28 mM, 10 ml total volume) and acetone (2.0 ml) under microwave induced reflux for 6.0 mins. From the top row to the bottom row we have the name of the shape, a representative TEM images, a 3D graphical representation and the number of shape faces.

The various shapes observed by TEM are shown in Figure 4.4.4.9. The average size and shape of each particle were measured for comparison [N = 140] (Figure 4.4.4.10). Similar trends to Solution A at Day 8 were observed in Solution A* at Day 1. For instance, the abundance of a shape increased with the number of shape faces. In addition, the average particle diameter decreased with the number of shape faces in an exponential manner as previously observed (Figure 4.4.4.7). However, there were some clear differences. For instance, the average particle diameters of the spheres, dodecahedrons and decahedrons were significantly larger (by ≈ 20 nm). The flat truncated triangular structures (195 nm) were also larger than those observed in Solution A – 6.0 at Day 8 (130 nm) but smaller than those observed in Solution A – 3.0 at Day 8 (262 nm). In addition, the populations were more lop-sided to shapes with higher numbers of faces, where the formation of spheres was more dominant (75 % abundance).

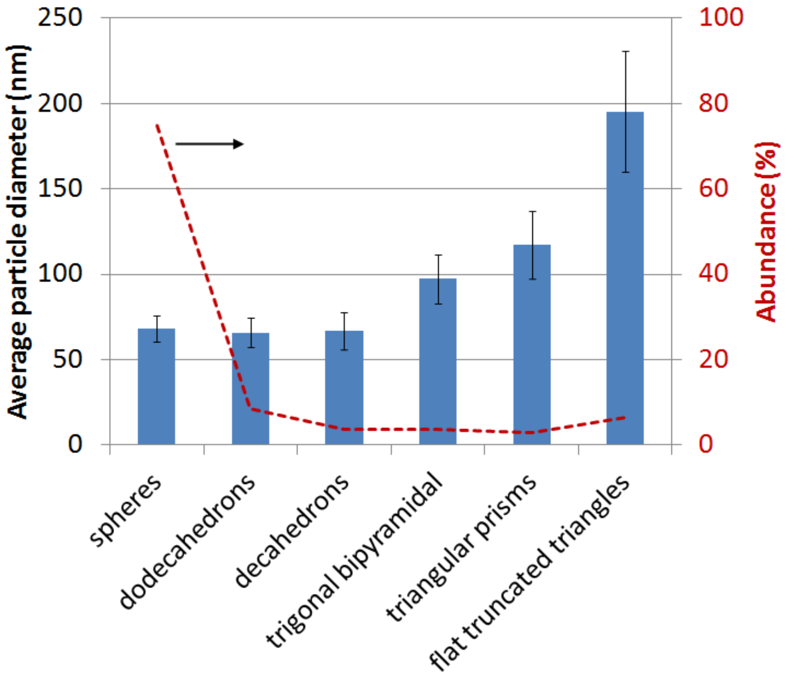

Figure 4.4.4.10: Average particle diameter (nm) [left axis] and their relative abundance (%) [right axis] for Solution A* – 6.0 at Day 1 (N = 140); a gold colloid formed from the reaction of auric acid (0.28 mM, 10 ml total volume) and acetone (2.0 ml) under microwave induced reflux for 6.0 mins.

Comparing the two solutions of equal reflux time (6.0 mins) but differing acetone volume (0.5 and 2.0 ml) we see several differences when quadrupling the acetone concentration:

(i) A dramatic increase in reaction rate (*i.e. the* SPR absorbance maximum is doubled at Day 1 and the nanoparticle formation reaction does not require ageing to complete)

(ii) An ≈ 40 % increase in the average diameter of the spherical particles formed (from 49 nm in Solution A – 6.0 to 69 nm in Solution A* – 6.0)

(iii) An increasing presence of spherical shapes, a similar presence of large flat truncated triangles and a lower presence of decahedral structures.

(iv) A decrease in the SPR absorbance maximum with time (≈ 17 % reduction over 1 week of storage in the dark)

What was of particular interest was how the SPR absorbance maximum decreased over 1 week. This indicated that the nanoparticles were not indefinitely stable in solution when a higher concentration of acetone was present. Moreover, a prolonged storage led to nanoparticle precipitation, where a small gold-coloured was observed at the bottom of the Solution A* – 6.0 after two weeks.

One of the key benefits of making colloidal gold with a higher acetone concentration (2.0 ml over 0.5 ml) was the complete formation of the nanoparticles after the 6 minute reflux period. However, their instability in solution begs the question of how they can be made more stable? The high solubility of acetone in water makes it difficult to remove. We propose that by increasing the reflux time of solutions with low levels of acetone may yield a quicker formation of gold nanoparticles (*i.e.* at Day 1) with better long term stability.

In the Solution A series, it was generally observed that the SPR absorbance maximum increased with the initial microwave induced reflux time (Figure 4.4.4.2(b)). An example of this trend at Day 3 is shown in Figure 4.4.4.11 revealing a shallow first order exponential relationship of strong correlation ($r^2 = 0.99$)

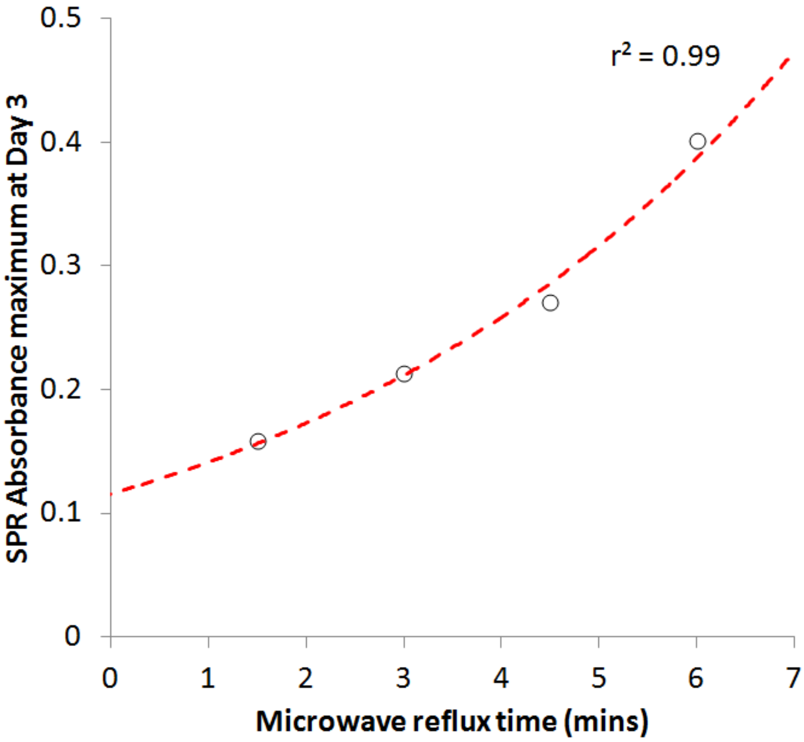

Figure 4.4.4.11: The relationship between the initial microwave induced reflux time (mins) and the SPR absorbance maximum at Day 3 for the Solution A series; a set of gold colloids formed from the reaction of auric acid (0.28 mM, 10 ml total volume) and acetone (0.5 ml) under microwave induced reflux for 1.5, 3.0, 4.5 or 6.0 mins.

4.4.4.1.1. Possible reaction mechanism

With the exception of Solution A – 1.5, the SPR absorbance maxima had reached a plateau by Day 8. The final point of plateau was higher with a longer initial microwave induced reflux time. This showed how the final concentration of the gold nanoparticles formed was limited by the initial reflux time – giving insight into the formation mechanism. This shows that heat is required to initiate the reaction but is not completely self-propagating. Rather, the period of reflux is what controls the eventual concentration of gold formed. TEM analysis of the solutions at Day 1 (Figure 4.4.4.4) and Day 8 (Figure 4.4.4.5) shed further light on the reaction mechanism:

(i) Reflux/ heat initiates the reduction of auric acid (Au^{3+}) by acetone to metallic gold (Au^0)

(ii) Further reduction of auric acid occurs at Au^0 sites or Au^0 atoms aggregate to form small, non-dense and spherical-like Au^0 particles (≈ 12 – 20 nm in diameter [Figure 4.4.4.4 & Table 4.4.4.2])

(iii) These non-dense Au^0 particles either encourage the formation of more non-dense Au^0 particles at their surface or aggregate to form large multi-core structures (≈ 50 – 100 nm in diameter [Figure 4.4.4.4 & Table 4.4.4.2])

(iv) Once these large multi-core structures are present, their collapse to dense Au^0 of defined shape and size is imminent; taking several days to do so when a low concentration of acetone is used (0.5 ml in the Solution A series [Figure 4.4.4.5]) or immediately when a high concentration of acetone is used (2.0 ml in Solution A* – 6.0 [Figure 4.4.4.8])

(v) The final size and concentration of the dense nanoparticles formed increase with reflux time. In addition, the fraction of spherically shaped particles increases with reflux time and acetone concentration.

At first glance, the collapse of the large multi-core structures to the dense nanoparticles of well-defined shape seems to be the rate limiting step. This is because their collapse took place over several days in the Solution A series. The use of a higher concentration of acetone seems to increase the speed at which this occurs. However, we suggest that this could be due to two plausible phenomena: (i) a greater presence of acetone facilitates the break-up of these particles to dense structures or (ii) increases the rate at which Au^{3+} is reduced to Au^0 and thus the rate at which the multi-core structures reach a critical size and break apart.

The mechanism of the Turkevich reaction (the aqueous reaction of auric acid with tri-sodium citrate) has been studied in great detail.[78,79] Through TEM studies Rodriguez-Gonzalez *et. al.* showed that large multi-core structures (*ca.* 100 nm in diameter) composed of smaller particles (5 – 10 nm in diameter) were initially formed.[78] A sharp increase in the conductivity after prolonged heating led to the formation of dense nanoparticle structures *ca.* 15 nm in diameter. Chow and Zukowski showed that only a fraction of the gold salt was consumed in the early stages of the reaction, forming a complex between gold chloride and citrate/citrate oxidation products.[79] The absorption of $AuCl_4$ led to reversible aggregation resulting in a progressive increase in the surface potential. An accelerated loss of auric acid was seen when the Au^{3+}/Au^0 ratio fell below 0.7 corresponding to a rapid change in the colour from light purple to red and the break-up of the large multi-core structures.[79] It is therefore the rate at which this critical ratio between Au^{3+} and Au^0 that facilitates the break-up of the multi-core structures.

Given the similarities in the two reaction mechanisms (*i.e.* auric acid reduced by acetone/ tri-sodium citrate) we suggest that the increase in acetone concentration merely increases the rate at which Au^{3+} is reduced to Au^0 and therefore the rate at which the critical ratio is reached ($Au^{3+}/Au^0 < 0.7$). The fact that the multi-cores took several days to collapse in the Solution A series is not simply explained. For instance, if the Au^{3+}/ Au^0 ratio truly dictates the point at which the multi-cores collapse then the ratio must change over the storage period in the dark without heat. This suggests that the auric acid can be reduced by the acetone without heating. However, no reaction was observed without first heating the samples. The reduction of auric acid to Au^0 is not a one-step process. To rationalise our observations we propose reduction process that includes two key stages. The first stage possesses a high activation energy barrier that requires heating to be surpassed. The second stage contains a lower activation energy barrier that can occur at room temperature, albeit more slowly than at reflux. Studies of the Turkevich reaction conducted by Rodriguez-Gonzalez *et. al.* showed that the reduction of auric acid (Au^{3+}) to $AuCl_2^-$ (Au^{1+}) controlled the induction time of the gold nanoparticle formation reaction.[78] Only when a sufficient level of $AuCl_2^-$ had formed, nucleation could ensue. We suggest that the initial period of microwave induced reflux allows auric acid to be rapidly reduced to $AuCl_2^-$:

$$AuCl_4^- + 2e^- \rightarrow AuCl_2^- + 2Cl^-, \;\; E^0 = +0.926\,V\,(NHE) \qquad \text{(Eq 4.5)}$$

The reduction of auric acid to $AuCl_2^-$ possesses a high activation energy barrier ($E^0 = +0.926$ V) and could only take place at higher temperatures (*i.e.* under reflux). The accumulation of $AuCl_2^-$ subsequently leads to its disproportionation:

$$3AuCl_2^- \rightarrow 2Au^0 + AuCl_4^- + \; 2Cl^- \qquad \text{(Eq 4.6)}$$

As the reduction of a metal chloride by acetone must be a 2 electron transfer process,[116] the direct reduction of $AuCl_2^-$ to Au^0 was not possible and the disproportionation of $AuCl_2^-$ to Au^0 seemed to be the only viable route to Au^0. According to Gammons *et. al.*, the disproportionation of $AuCl_2^-$ to Au^0 takes place at room temperature, albeit quite sluggishly.[117] However, the rate of the disproportionation reaction increases rapidly with $AuCl_2^-$ concentration and temperature. Moreover, the reaction was catalysed by the presence of Au foil. In consideration of their studies we propose that the disproportionation of the $AuCl_2^-$ complex to Au^0 was slow and the rate-limiting step in the overall reduction process. The slow kinetics in the conversion of $AuCl_2^-$ to Au^0 would explain why it took several days for the critical ratio of Au^{3+}/Au^0 to be reached, where the multi-core structures fall apart. It also explained why a higher acetone concentration increases the speed of Au^0 formation, where $AuCl_2^-$ is more rapidly formed by the increased supply of electrons from the reducing agent and its disproportionation accelerated due to its high concentration dependence. The fact that Au^0 catalyses the disproportionation of $AuCl_2^-$ to Au^0 indicates that Au^0 growth at Au^0 sites will be favoured, leading to the nucleation and growth of Au particles through the continued absorption and disproportionation of $AuCl_2^-$. Based on the chemistry of pentavalent bismuth salts with cyclohexanone[115] and copper chloride with acetone,[116]and our observations of the reactions of $AuCl_3$ and cyclohexanone (Section 4.3.5), a reaction mechanism for the reaction of auric acid with acetone was suggested:

$$HAuCl_4 \rightleftharpoons AuCl_3 + HCl \qquad \text{(Eq 4.7a)}$$

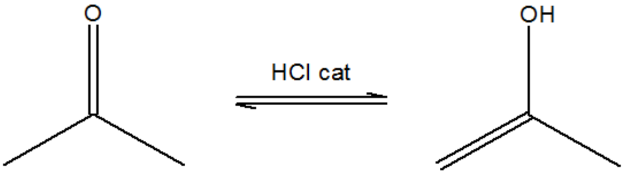

(Eq 4.7b)

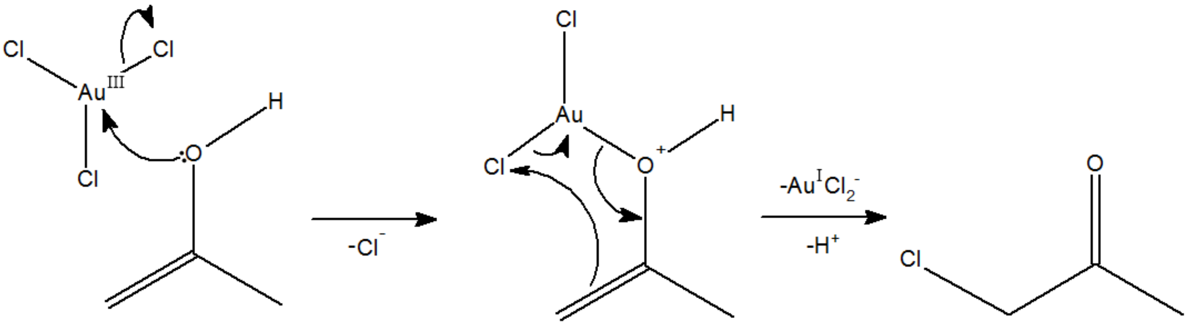

(Eq 4.7c)

Auric acid ($HAuCl_4$) forms an equilibrium in solution with the release of HCl and formation of $AuCl_3$ (Eq 4a). The release of HCl catalytically encourages the tautomerism of the ketone group of acetone to the enol (Eq 4b). Trigonal planar $Au^{III}Cl_3$ is then attacked by the nucleophilic lone pair on oxygen in the enol group leading to the S_N2 ejection of Cl^- (Eq 4c). The locality of the Cl-Au-O bond to the α-alkene bond leads to the cyclic nucleophilic attack of Cl, the reduction of gold from Au^{III} to Au^I and reformation of the ketone functional group. This leads to the formation of $AuCl_2^-$ alongside the by-product, chloroacetone. These reduced Au^I complexes disproportionate in accordance with

Equation 4.6 to form Au^0 atoms and auric acid (Au^{III}). The sequential steps in the reduction reaction can be summarised as:

$$3CH_3COCH_3 + 3HAuCl_4 \xrightarrow{-3CH_3COCH_2Cl} 3H^+ + 3HCl + 3AuCl_2^- \rightarrow 2Au^0 + HAuCl_4 + \ 5HCl$$

(Eq 4.8a)

and the overall reaction as:

$$3CH_3COCH_3 + 2HAuCl_4 \xrightarrow{-3CH_3COCH_2Cl} 2Au^0 + 5HCl \qquad \text{(Eq 4.8b)}$$

The Au^0 catalytically promote the disproportionation of $AuCl_2^-$ (Eq 3) and thus encourage the localised growth of Au^0 particles.

4.4.4.2. 3-pentanone and acetylacetone as a reducing agent in the synthesis of gold colloids

Preliminary reactions were conducted with the alternative ketones 3-pentanone or acetylacetone in the place of acetone (Table 4.4.3.1). The UV-visible spectra of the solutions formed are shown in Figure 4.4.4.3.

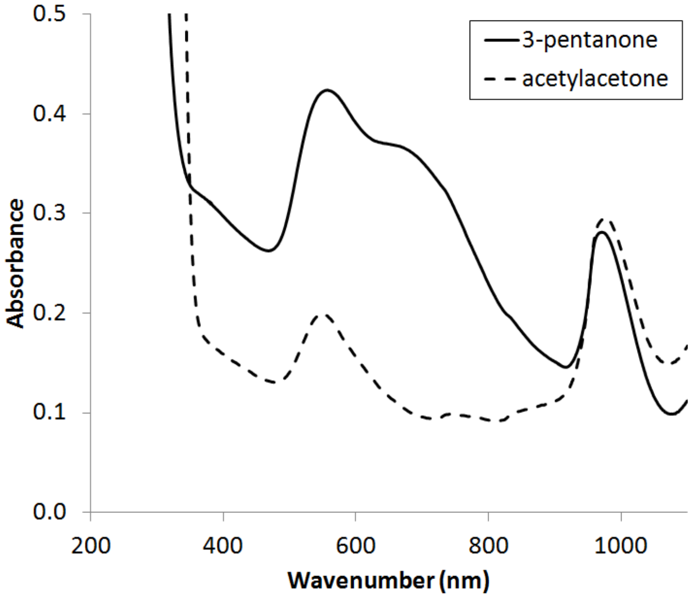

Figure 4.4.4.12: The UV-visible absorption spectra of the gold nanoparticle solutions formed by the microwave-assisted reflux of auric acid (0.28 mM, 10 ml total volume) with either 0.5 ml of 3-pentanone (sample P – 6.0) or 0.5 ml acetylacetone (sample AA – 6.0) for 6.0 mins at Day 1.

The time evolution of the UV-visible absorption profile was not investigated. Gold plasmon bands were present in both solutions, indicating the formation of colloidal gold. The nanoparticle solution formed using acetylacetone behaved strikingly similar to that formed from acetone over

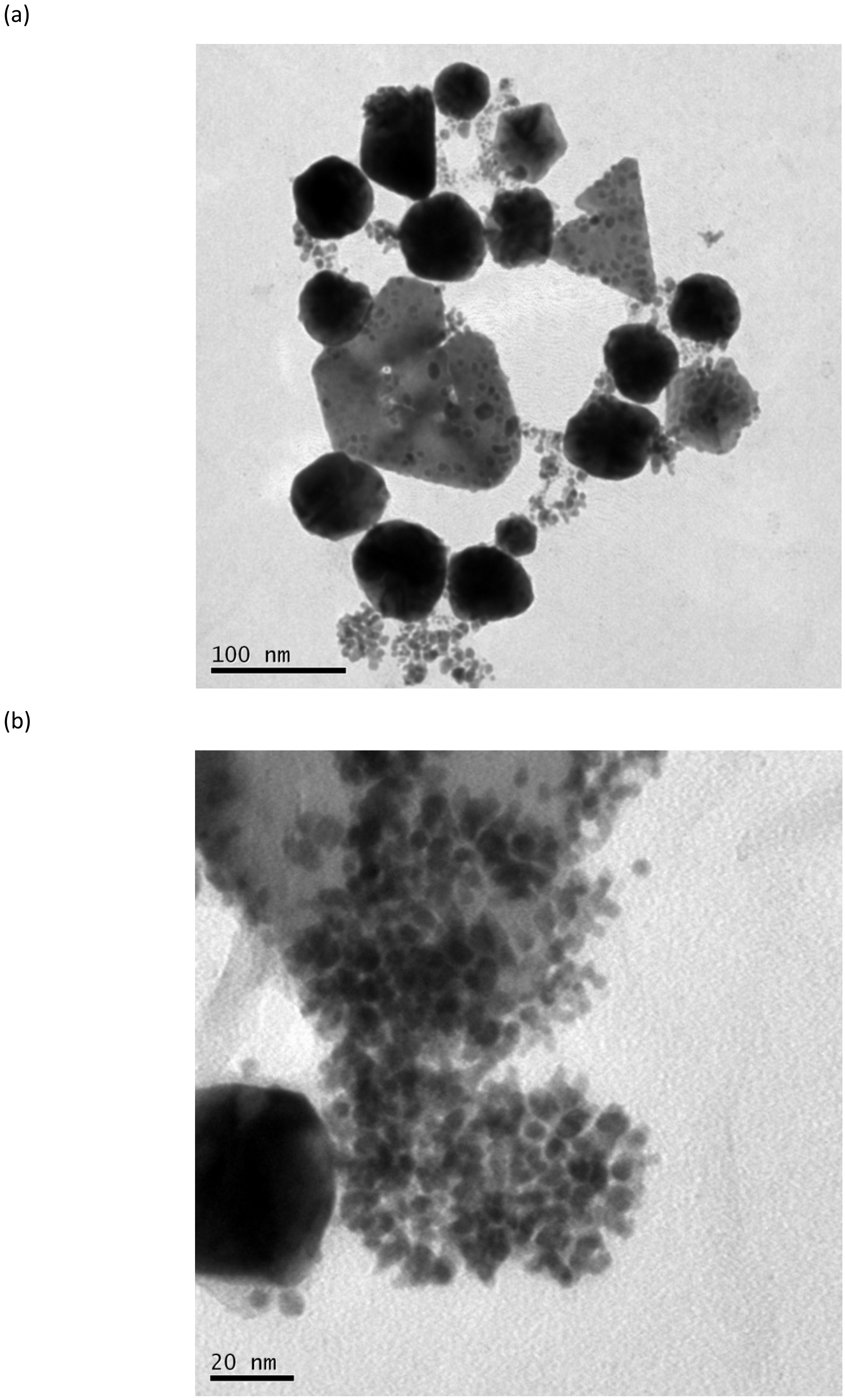

Figure 4.4.4.13: TEM images of gold nanoparticles formed from the reaction of auric acid (0.28 mM, 10 ml total volume) and acetylacetone (0.5 ml) under microwave induced reflux for 6.0 mins (Solution AA – 6.0) at Day 1 immediately after reflux.

the same reflux time of 6.0 mins. The solution formed from acetylacetone showed an SPR band with λ = 550 nm, Abs = 0.1993 whereas the solution formed from acetone showed an SPR band with λ = 548 nm, Abs = 0.2035 on Day 1. On the other hand, the nanoparticle solution formed from 3-pentanone possessed two plasmon bands. In this case we observed an initial SPR band centred at λ_1 = 558 nm, Abs = 0.4240 and a secondary SPR hump located at around λ_2 = 692, Abs = 0.3975 were observed. This indicated one of two phenomena: (i) a non-Gaussian distribution of nanoparticle sizes of equivalent shape (*i.e.* two distinct average sizes were favoured) or (ii) a substantial deviation from spherically shaped particles (*i.e.* the formation of non-isotropically shaped particles that display plasmon properties that differ with the incidence of light such as nanorods[70]).

The particles formed at Day 1 were investigated by TEM. Sample images of the gold nanoparticle solution formed using acetylacetone (Solution AA – 6.0) as the reducing agent are shown in Figure 4.4.4.13. As opposed to the two situations observed previously (either large multi-core structures made up of small particles or dense nanoparticles of various sizes and shape) we see an intermediate situation between the two; where dense particles are partially formed and smaller fragments of the multi-core structures are present (Figure 4.4.4.13(a)). If we assume that the formation of smaller fragments came from the densification of the large multi-core structures, these images reveal an intermediate stage where the multi-core have partially collapsed and are still in the process of forming compact shapes. This indicates that at equal volumes of acetone and acetylacetone (0.5 ml), the nanoparticle formation reaction is faster when acetylacetone is used. A higher presence of the multi-core fragments was present at the edges and cracks of these dense particles. A high magnification image shows the high presence of these multi-core fragments at the edge of a truncated triangle nanosheet (Figure 4.4.4.13(b)). The small particles were roughly 5 nm in diameter; a similar size to those round particles formed within the multi-core structures in reactions with acetone (0.5 ml) at Day 1.

The particles formed in reactions with 3-pentanone (Solution P – 6.0) were also investigated by TEM. Sample images of the gold nanoparticle solution formed using acetylacetone as the reducing agent are shown in Figure 4.4.4.14. At lower magnifications there is little difference between the range of particles and sizes observed in reactions with 3-pentanone (0.5 ml) at Day 1 (Figure 4.4.4.14(a)) with acetone (2.0 ml) at Day 1 (Figure 4.4.4.8(a)). However, at higher magnifications we see that particles were more elliptical with aspect ratios ranging roughly between 1 and 3 (Figure 4.4.4.14(b)). It is well known that gold nanorods show two SPR bands.[70] As such, the presence of elliptical particles in reactions with 3-pentanone explains why two SPR bands were observed at 558 nm and 692 nm (Figure 4.4.4.12).

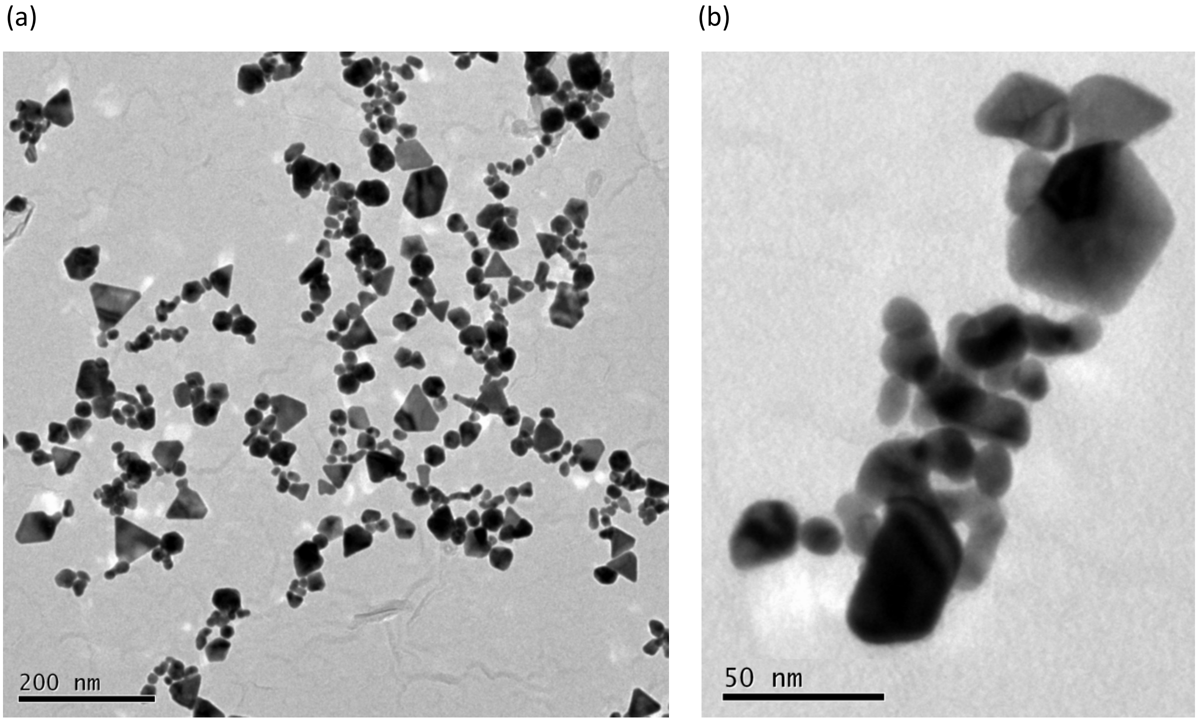

Figure 4.4.4.14: TEM images of gold nanoparticles formed from the reaction of auric acid (0.28 mM, 10 ml total volume) and 3-pentanone (0.5 ml) under microwave induced reflux for 6.0 mins (Solution P – 6.0) at Day 1 immediately after reflux.

Excluding the measurement of elliptical particles, the abundance and average diameter of each type of shape observed were determined for reactions with acetylacetone (Solution AA – 6.0) and 3-pentaonen (Solution P – 6.0). The results were tabulated alongside the results obtained from reactions of acetone (Solution A – 6.0) at Day 8 (Table 4.4.4.3). The three reactions were similar in the sense that a range of particles shapes of various sizes were formed, including the truncated triangular nanosheets. However, significant differences in the abundance of each shape and its average size were observed. To more easily compare trends, bar charts of the particle abundances (Figure 4.4.4. 15(a)) and sizes (Figure 4.4.4. 15(b)) were drawn.

Looking at the change in shape abundance, we see that reactions with acetone were almost twice as liable to form spheres (60 %) than reactions with acetylacetone or 3-pentanone (≈ 35 %). However, reactions with acetylacetone were most liable to form dodecahedrons (23 %) and reactions with 3-pentanone were most liable to form decahedrons (24 %). The relative abundances of triangular structures were similar. Although there was a general trend, where particle diameter increased as the number of shape faces decreased, the sizes of each shape differed substantially between reactions. Spheres formed in reactions with acetone and acetylacetone (≈ 50nm in diameter) were more than twice the size of those formed in reactions with 3-pentanone (≈ 20 nm in diameter). However, the dodecahedrons and decahedrons formed in reactions with acetone were >

40 % larger than those formed in reactions with acetylacetone or 3-pentanone. Moreover, any triangular structure formed in reactions with acetone was nearly twice as big as those formed in reactions with acetylacetone or 3-pentanone.

Table 4.4.4.3: The abundances (%) and average diameters (nm) of the variety of dense shapes formed in the reaction of 0.5 ml of acetone (Day 8), acetylacetone (Day 1) or 3-pentanone (Day 1) with auric acid (0.28 mM, 10 ml total volume) under microwave induced reflux for 6.0 mins. The error in diameter is taken as the standard deviation of the measured particles (N > 60).

	A - 6.0	AA - 6.0	P - 6.0	A - 6.0	AA - 6.0	P - 6.0
	acetone	acetyl-acetone	3-pentanone	acetone	acetyl-acetone	3-pentanone
	Abundance (%)			diameter (nm)		
spheres	60	35	36	49.0 ± 10.6	50.3 ± 9.8	21.8 ± 4.3
dodecahedrons	6	23	17	53.0 ± 15.1	32.9 ± 7.4	29.0 ± 4.1
decahedrons	23	16	24	52.2 ± 16.6	39.2 ± 7.5	31.6 ± 3.3
trigonal bipyramidal	0	9	7	-	61.1 ± 13.1	35.3 ± 2.6
triangular prisms	2	4	3	64.1 ± 37.5	39.5 ± 9.3	34.8 ± 2.7
flat truncated triangles	8	14	12	130 ± 24.3	71.9 ± 9.1	49.3 ± 6.1

A general trend was observed, where particle size were generally larger in solutions formed with acetone, an intermediate size when formed with acetylacetone and smallest when formed with 3-pentanone. The average particle diameter, irrespective of shape, was determined; quantifying this trend:

$$56.9\ nm\ (acetone) > 48.2\ nm\ (acetlyacetone) > \ 30.1\ (3\ pentanone) \qquad \text{(Eq 4.9a)}$$

This size decrease corroborated with spectroscopy, where the SPR band increased from:

$$541\ nm\ (acetone) < 550\ nm\ (acetlyacetone) < \ 558\ nm\ (3\ pentanone) \qquad \text{(Eq 4.9b)}$$

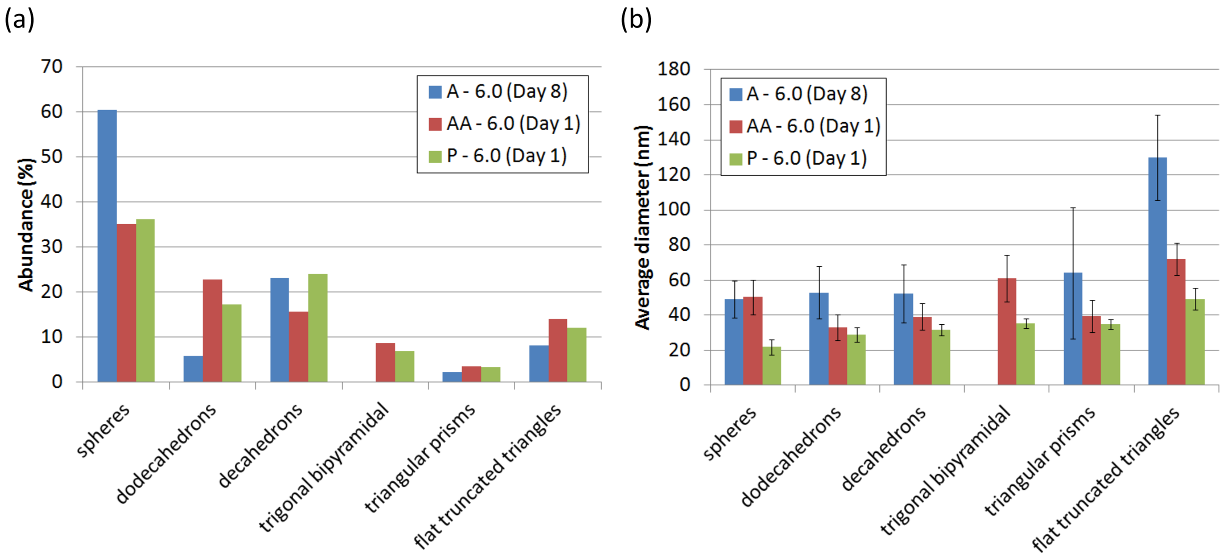

Figure 4.4.4.15: Bar charts showing (a) the abundance [%] and (b) the average diameter [nm] of each type of shape formed from the reaction of 0.5 ml of acetone [A – 6.0 (Day 8)], acetylacetone [AA – 6.0 (Day 1)] or 3-pentanone [P – 6.0 (Day 1)] with auric acid (0.28 mM, 10 ml total volume) under microwave induced reflux for 6.0 mins.

4.4.4.2.1. Possible reaction mechanisms

3-pentanone possesses two equivalent α-carbons (C2, C4) that can tautomerise to the enol; forming either the E or Z isomer:

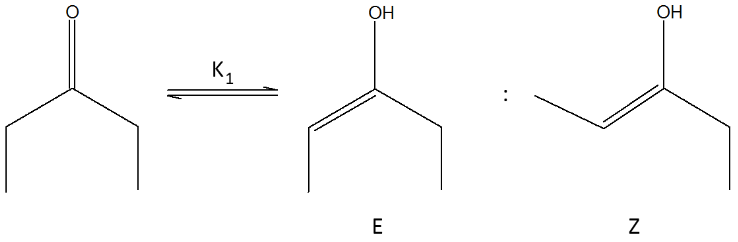

(Eq 4.10a)

where K_1 = 3.7 x 10^{-8}.[118] Assuming the reaction of 3-pentanone and auric acid was mechanistically similar to the reaction of cyclohexanone and auric acid (Section 4.3.5) we predict the more favourable reaction of the E isomer. This is because the alkene bond is more open to nucleophilically attack gold once it is anchored at the hydroxyl group:

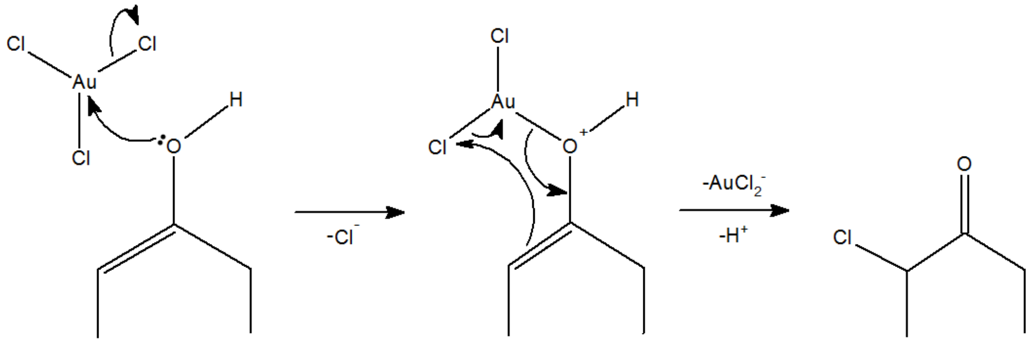

(Eq 4.10b)

Trigonal planar $Au^{III}Cl_3$ is attacked by the lone pair on oxygen in the enol group leading to the S_N2 ejection of Cl^- (Eq 4c). The locality of the anchored Cl-Au-O bond to the open alkene leads to the cyclic nucleophilic attack of Cl, the reduction of gold from Au^{III} to Au^{I} and reformation of the ketone. This leads to the formation of $AuCl_2^-$ alongside the by-product, 2-chloro-pentan-3-one. $AuCl_2^-$ disproportionates forming Au^0 atoms and auric (Au^{III}) acid (Equation 4.6). The Au^0 catalytically promote the continued disproportionation of $AuCl_2^-$ and thus promotes the localised growth of Au^0 particles.

Acetylacetone possesses two non-equivalent pairs of α-carbons (C1, C5’ and C3, C3’) that can tautomerise to the enol. The two pathways are shown below:

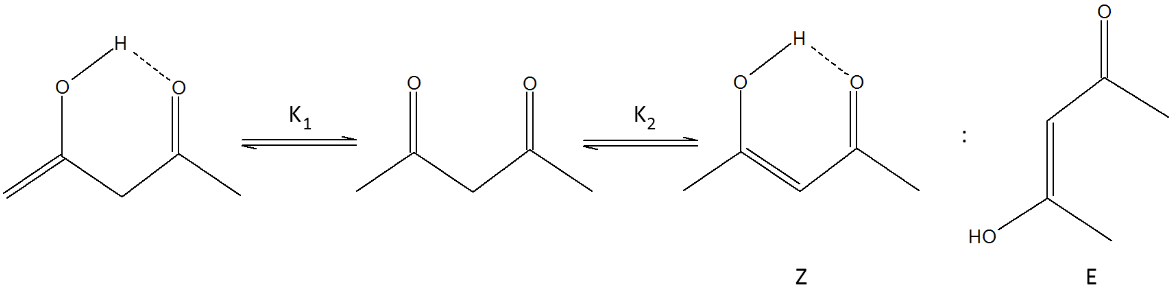

(Eq 4.11a)

where $K_1 << K_2 = 5.5$.[119] Enolisation at either C1 or C5’ leads to the formation of the 1-ene-2-ol (pathway K_1). Enolisation of the C3, C3’ pair leads to the generation of the 2-ene-2-ol (pathway K_2); forming either the Z (omega form) or E (sickle form) isomer.[120] The formation of the omega form is favoured. This is due to the greater acidity of protons at position C3 than protons at C1 ($K_2 >> K_1$) in addition to the stability gained by delocalisation of electrons across the alkene bond α to the ketone group (Z >> E).

Assuming the reaction of acetylacetone and auric acid was also mechanistically similar to the reaction of cyclohexanone and auric acid (Section 4.3.5) we predict the more favourable reaction of either the 1-ene-2-ol (pathway K_1) or the E isomer of the 2-ene-2-ol (pathway K_2). Once again, this is due to the alkene bond being less sterically hindered to nucleophilically attack gold once anchored by the hydroxyl group. The reaction mechanism for the E isomer of the 2-ene-2-ol (Equation 4.11b) and the 1-ene-2-ol (Equation 4.11c) are shown below:

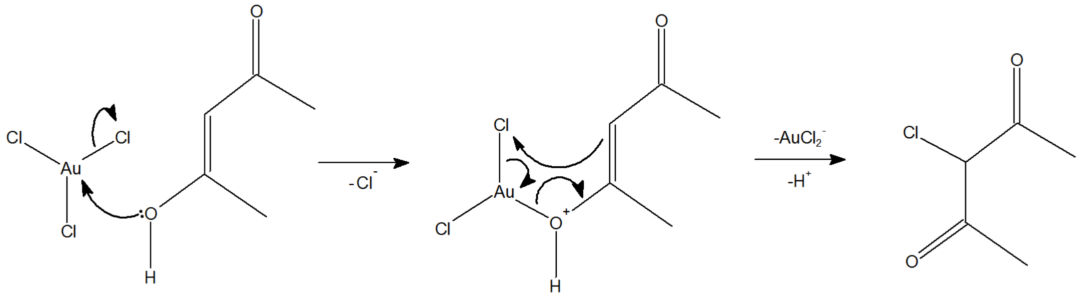

(Eq 4.11b)

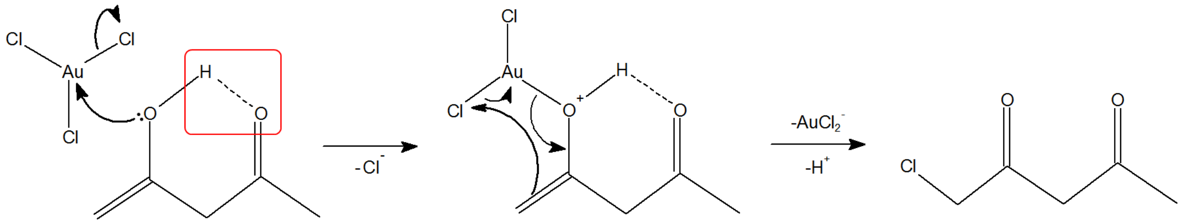

(Eq 4.11c)

In the case of the 1-ene-2-ol, the hydrogen on the hydroxyl group is stabilised by the ketone at C4; decreasing the polarity and nucleophilicity of the hydroxyl group (highlighted in red – Equation 4.11c). Therefore, of the two routes, we predict the reaction with the E isomer of the 2-ene-2-ol is favoured as the hydroxyl group is more nucleophilic and free to react (Equation 4.11b).

4.4.5. Conclusions

Gold nanoparticles were synthesised from the reaction of auric acid and a ketone at microwave induced reflux. Three ketones were examined; acetone, 3-pentanone or acetylacetone. Reactions with acetone in low concentration (0.68 M) were not complete after the initial reflux period and took several days to complete when stored at room temperature thereafter. These progressive changes were assessed using UV-visible spectroscopy and transmission electron microscopy (TEM) over 8 days. Several transformations in the particle shape and size were observed. This involved the initial formation (Day 1) of large multi-core structures [≈ 50 – 100 nm wide] composed of smaller aggregates [≈ 10 – 20 nm wide] that later (Day 8) broke apart and compacted into dense gold particles of varied shape and size [mostly 40 – 50 nm wide]. The transformations were analogous to those underwent in room temperature reactions of cyclohexanone with auric acid (Section 4.3). Given the similarity in growth and chemistry of the two reactions, an analogous mechanistic pathway was proposed, where acetone reduced Au^{3+} ions in auric acid forming chloroacetone and Au^{1+} ions in $AuCl_2^-$ that later disproportionate to Au^0. Conversely, reactions of auric acid with acetylacetone or 3-pentanone were primarily complete after the initial reflux period (6 mins). Particles formed from 3-pentanone were significantly smaller and more elliptical than those formed from acetone or acetylacetone.

4.5. Comparisons of gold nanoparticle reactions with cyclohexanone and other ketones

The relative rates for the reaction of auric acid with acetone, acetylacetone or 3-pentanone was assessed by comparing the heights of their SPR absorption bands immediately after reflux. The reaction with acetone (Figure 4.4.4.2, Solution A – 6.0) showed an SPR band positioned at λ = 548 nm with an absorbance of 0.20. The reaction with acetylacetone (Figure 4.4.4.12, Solution AA – 6.0) showed an SPR band positioned at λ = 550 nm with a similar absorbance of 0.20. The reaction with 3-pentanone (Figure 4.4.4.12, Solution P – 6.0) showed a most intense SPR band at λ = 558 nm with an absorbance of 0.40. The self-activated room temperature reaction of cyclohexanone with auric acid showed an absorbance of 0.63 after 65 mins of reaction. Comparing absorbance alone we see the following trend in rate:

$$cyclohexanone > \ 3\ pentanone > acetylacetone\ \approx\ acetone$$

(Eq 4.12a)

The respective concentrations of each ketone in these reactions were:

$$cyclohexanone\ [0.48\ M] \approx\ 3\ pentanone\ [0.47\ M] \approx acetylacetone\ [0.49\ M] <\ acetone\ [0.68\ M]$$

(Eq 4.12b)

However, in relation to our proposed reaction mechanism for ketones with auric acid (see Section 4.3.5), the concentration of the enolised form (pK_e) of the ketone is more important than the concentration of the ketone itself, where:[118,119]

$$acetylacetone\ (-0.74) < cyclohexanone\ (6.38) <\ 3\ pentanone\ (7.43) < acetone\ (8.33)$$

(Eq 4.12c)

The pK_e of acetylacetone (-0.74) was several orders of magnitude lower than the pK_e of any other ketone examined. This means that on average 99.8% of the ketone is in its enolised form. However, this value represented the pK_e in forming the 1-ene-2-ol form; the form that we believe to be less nucleophilic to reactions with auric acid (see Eq. 4.11c). In fact, the pK_e of the more sterically favourable 2-ene-2-ol form is, to our knowledge, unknown. The pK_e of cyclohexanone (6.38) was an order of magnitude lower than that of the E isomer of 3-pentanone (7.43) and two orders of magnitude lower than the pK_e of acetone (8.33). Nevertheless, a pK_e of 6.38 means that on average only 0.004 % of the ketone exists in its enolised form. If we now account for differences in pK_e and ketone concentration we see the following trend in enol concentration:

$$acetylacetone\ [0.49\ M] \gg cyclohexanone\ (20\ \mu M) > 3\ pentanone\ (1.8\ ) > acetone\ (0.32\ \mu M)$$

(Eq 4.12d)

As the pK_e of the more nucleophilic enol form of acetylacetone (2-ene-2-ol) was not known, the true effect of enol concentration on the reaction rate could not be studied for this ketone. This was not the case for the remaining three ketones. The enol form of cyclohexanone was ≈ 12 times more concentrated than the least sterically hindered enol form 3-pentanone (the E isomer) and was ≈ 62 times more concentrated than the enol form of acetone. This could explain why the reduction reaction was nearly twice for 3-pentanone over acetone. Going further, this may also explain why reactions with cyclohexanone can take place at room temperature given the high concentration of the enol form relative to 3-pentanone and acetone.

Overall, by comparing the pK_e of the stereochemically active enol forms a direct trend between enol concentration and reaction rate with auric acid was observed. This should serve as a guide for those wishing to examine alternative ketones, where non-sterically hindered ketones possessing low pK_e values should provide a more rapid reaction. Future studies of ketones with high tendencies to form non-sterically hindered enol forms would prove this theory true and may lead to the discovery of ketones besides cyclohexanone that can self-activate the formation of gold colloids at room temperature. Of additional interest would be reactions of aldehydes with auric acid, given their relatively higher acidity and propensity to enolise compared with ketones. For instance some common potential candidates include ethanal (pK_e = 6.23),[121] phenyl acetaldehyde (pK_e = 3.07 for the non-sterically hindered E isomer)[122] and 2-indanone (pK_e = 3.84)[123] – examples that all possess pK_e values far lower than cyclohexanone (pK_e = 6.38).

Upon comparing all nanoparticle formation reactions, we find no rational trend between the ketone used and the size and shape of the particle formed. For instance, when acetone or cyclohexanone was used, the presence of each type of particle formed (*i.e.* sphere, dodecahedron *etc*) and its average diameter was similar (Table 4.4.4.3 and Figure 4.3.4.6). When acetylacetone was used the average particle sizes were similar but a significantly lower presence of spheres (≈ 30% less) and a significantly higher presence of dodecahedrons were present (≈ 20% more). The greatest anomaly was 3-pentanone, where the average particle diameters were substantially smaller (by ≈ 50%). This was attributed to the higher tendency of elliptical particle formation (Figure 4.4.4.14(b)).

Where the nanoparticle shape and size was examined in the early stages of the reaction, large multi-core clusters composed of smaller spherical particles were consistently formed. This phenomenon was similarly observed in the formation of gold nanoparticles from the reaction of auric acid and tri-sodium citrate.[78,79] It was explained by Rodríguez-González *et. al.* that as Au^0 particles are formed there is a direct competition for adsorption sites on the gold particle surface sites between chloride ions and the surfactant.[78] During reduction, there is a net positive electronic charge on the gold, which is almost completely neutralized by adsorbed chloride ions. However, as the zeta potential is low, the nuclei form weakly charged Au^0 aggregates – leading to the formation of multi-core clusters (*i.e.* Figure 4.4.4.4). When the auric acid is almost consumed, the particle redox potential dramatically shifts towards more negative values. As the last remaining gold ions are reduced, the chloride ions absorbed on the surface of Au^0 particles are replaced by surfactant (*i.e.* the ketone). This induces peptization as the particle surface becomes more electrically neutral. The chemisorbed surfactant creates a negative zeta potential which leads to the dispersion of the small particles within these multi-core clusters. These small particles recombine and form more compact and dense shapes. An interesting example of the latter part of this process was observed in reactions with acetylacetone (Figure 4.4.4.13). Interestingly, the differing rate of gold nanoparticle formation when using different ketones allows this mechanism to be studied in greater depth. For instance, ketones with high pK_e values (*i.e.* low presence of the enol form) such as acetone (pK_e = 8.33)[124] and butanone (pK_e = 8.76)[118] could be used to study the transformation from auric acid to dense gold particles in a step-by-step fashion.

Previous work on the formation of gold nanoparticles using a ketone as the reducing agent is scarce. For reactions concerning cyclohexanone, the most similar example found in the literature was by Sarkhosh *et. al.*[109] Instead of using auric acid, a gold target was submerged in cyclohexanone and gold nanoparticles were formed by laser ablation of the target. This led to the growth of spherical particles that were typically 50 nm wide. A less similar example was demonstrated by Marin *et. al.* in their use of cyclic aryl ketones that could photocatalytically reduce solutions containing Au^{3+}/ Au^{+} ions to Au^0 particles.[110] Reactions of α-phenylbenzoin with auric acid yielded primarily spherical and partially truncated triangular structures ranging between 20 – 24 nm in diameter. Reactions of benzophenone with auric acid yielded more spherical and smaller particles ≈ 7 nm wide. Interestingly, the process was catalytic, where the aryl ketone could be recovered at the end of the reductive process. Another direct example of the use of cyclohexanone was demonstrated by Biswas *et. al,* however this was in the formation of copper based nanoparticles.[108] The copper particles were grown from a copper sulphate source in cyclohexanone: water: isopropanol: oil mixtures between ≈ 25 – 50 °C. Moreover, the particles that formed, be it CuI (3 – 30 nm wide) $CuCrO_4$ (30 – 60 nm wide) or CuS (40 – 100 nm wide) were ellipsoidal. From our work it was established that cyclohexanone can be used to form a variety of gold nanoparticle particle shapes of ranging size when reacted with aqueous auric acid at room temperature (Figure 4.3.4.6). What separates our synthesis from the literature is the non requirement of heat,[108] light[109,110] or any external energy source for the reaction to proceed with cyclohexanone. In addition, the chemical and physical mechanisms by which these gold nanoparticles form is presented (Section 4.3.5).

There are other examples in the literature where alternative ketones are used to produce gold nanoparticles. For example, Huang *et. al.* electrochemically induced the growth of truncated gold nanocubes from a gold electrode in an aqueous bath containing surfactants and acetone.[100,101] The cubes formed were highly monodisperse averaging 32.6 nm in width. In other examples triangular nanoplates,[125] hexagonal nanoplates[105] or a range of dense 3D particles[106] have been grown using the polymer ketone poly-vinyl-pyrrolidone (PVP). Ali Umar *et. al.* demonstrated the growth of primarily triangular platelet-like particles that were typically ≈ 5 nm thick and ≈ 200 - 500 nm wide in a two step room temperature process.[125] First a gold nano-seed (3 – 4 nm wide particles) was formed from the reaction of auric acid and $NaBH_4$: tri-sodium citrate over 2 hrs. The nano-seed was then mixed with cetyltrimethylammonium bromide (CTAB), polyethylene glycol (PEG) and the ketone PVP for 8 hrs. In the absence of PVP, large nano-flakes were formed. Interestingly, in the absence of PEG, a variety of particle shapes of ranging sizes were formed – analogous to our studies. Wang *et. al.* demonstrated the growth of ≈ 10 micrometer wide hexagonal nanoplates in a single step thermally activated process.[105] This was achieved in a similar fashion by refluxing reacting auric acid with CTAB, PEG and PVP for 30 mins at ≈ 150 °C. Other examples have shown that microwave-assisted reactions of auric acid with PVP and dimethylformamide, methanol or ethanol produced dense 3D shapes of quite varied shape and size.[106] Particles ranged in size from 10 – 200 nm adopting spherical, triangular, hexagonal, pentagonal and rod-like shapes. To our knowledge, neither 3-pentanone nor acetylacetone have been used to produce gold nanoparticles. Moreover, the microwave-assisted reaction of auric acid and acetone, 3-pentanone or acetylacetone is to our knowledge a new pathway to the growth of gold nanoparticles.

From our studies it was shown that the growth of gold nanoparticles from the reaction of auric acid and a ketone (be it a room temperature reaction with cyclohexanone or a microwave-assisted reflux with acetone, 3-pentanone or acetylacetone) proceeds in stages. Firstly large multi-core structures are formed (≈ 50 – 200 nm wide), composed of small spherical particles (≈ 10 nm wide). These large structures then break apart and rearrange themselves into dense structures. The dense structures formed were a variety of shapes and sizes – forming spherical, triangular, hexagonal and pentagonal 3D shapes (≈ 20 – 60 nm wide) and truncated triangular 2D nanoplates (≈ 50 – 500 nm wide). Stable multi-core nanoparticle structures have previously been achieved.[102,103] In one instance, Jena *et. al.* grew Au multi-core structures (≈ 200 nm wide), deemed nano-flowers, by simply reacting 5-hydroxyindole-3-acetic acid (HIAA) with auric acid at room temperature for 30 min.[103] In another case, Tong *et. al.* grew smaller Pd multi-core structures (≈ 50 nm wide) under microwave heating from the reaction of Pd acetate with ethylene glycol, KOH and a methyl isobutyl ketone.[102] The most similar gold colloid to those formed in our ketone syntheses was demonstrated by Ali Umar *et. al.* from the reaction of gold nano-seeds with CTAB and the ketone polymer PVP at room temperature.[125]

In the next section we will present a summary of our results from chapters 1 – 4 thus far. It will primarily be a summary of the different reagent concentrations and methods of activating the reactions employed (*i.e.* thermally activated, microwave-assisted *etc*) in the synthesis of our gold nanoparticles and the average size and abundance of the various shapes that form. This will be of particulate benefit to the reader if they desire to grow gold nanoparticles of a particular shape/ size.

4.6. A comparison of the gold nanoparticle reactions explored thus far

After revisiting the Turkevich synthesis (Chapter 2), various new methods of growing gold nanoparticles were explored (Chapters 3 & 4). Two major avenues were explored, where either:

(i) the reducing agent or
(ii) the method for activating the reduction reaction

was changed.

The auric acid concentration was kept constant (0.28 mM). The effect of changing the tri-sodium citrate reducing agent (used in the Turkevich synthesis) was investigated (from 0.96 to 3.88 mM). A range of activation methods were also investigated: (i) the traditional thermal route, (ii) microwave-assisted heating, (iii) ultra-violet light activation or (iv) sonolysis. The novel use of acetone, acetylacetone, 2-pentanone and cyclohexanone ketones as reducing agents was also explored. A table summarising the gold nanoparticle sizes and shapes formed from these syntheses is presented (Table 4.3.1).

It was found that altering the tri-sodium citrate concentration from 0.96 to 3.88 mM did not significantly change the shape or average size of the gold nanoparticles formed. Changing the activation method had a larger impact where ultra-violet light resulted in the formation of the smallest particles (from ≈ 8 – 11 nm in diameter) and sonication resulted in the formation of the largest particles (from ≈ 17 – 18 nm in diameter). Most shapes formed were spherical, irrespective of the activation method or tri-sodium citrate concentration examined. Only a slight deviation from spherical to ellipsoidal shapes was observed then activated using ultra-violet light. More substantial changes were observed when the reducing agent was replaced with various ketones. Firstly, a greater variety of shapes were observed from spherical to more defined dodecahedra, decahedra, trigonal bipyramids and other shapes. Secondly, the average particle sizes were larger ranging from ≈ 40 – 400 nm in diameter. Spheres were still the most common shape in all of the colloids formed from ketones. However, acetylacetone showed the greatest propensity to form a variety of shapes. The particles grown using 2-pentanone showed some ellipsoidal nature, with aspect ratios in particles ranging from 1 to 3 (*i.e.* purely spherical to strongly ellipsoidal). Large "2D" triangular nanoplates were observed for all ketones explored. The size of these nanoplates ranged from ≈ 50 nm using 2-pentanone to ≈ 80 nm using acetylacetone to ≈ 100 - 200 nm using acetone to ≈ 250 – 400 nm using cyclohexanone. Interestingly, the reaction of auric acid and cyclohexanone occurred at room temperature and required no external activation source. A more than quadruple increase in the acetone concentration resulted in only marginal increases in average particle size (from ≈ 50 to 70 nm).

Table: 4.6.1: A summary of the sizes, shapes and abundance of each shape of the particles formed in the gold colloid syntheses investigated in Chapters 2 – 4. Reagent concentration shown in square brackets; *Thermal* denotes reactions heated at 100 ˚C for 10 mins; *MWA* denotes microwave-assisted (750 W) reactions heated at reflux for the time indicated in brackets; *Sonolysis* denotes sonication (60 Hz) for 60 mins; *UV* denotes irradiation with 254 nm (16 W) for 60 mins. *Ellipsoid diameters are an average of the projected length and width. †Shapes measured from the point of a vertex that bisects the projected image. ‡Self-activates at room-temperature where the shapes and sizes shown are for a solution after 3 months (*i.e.* a "*ripened*" solution).

Reagent [concentration]		Activation method	Particle shape, size and population							
			Sphere	Ellipsoid*/ aspect ratio	Dodecahedra†	Decahedra†	Trigonal bipyramids†	Triangular prisms†	Triangular nanoplates†	Hexagonal nanoplates†
auric acid [0.28 mM]	tri-sodium citrate [0.96 mM]	Thermal	11.4 ± 2.2	-	-	-	-	-	-	-
		MWA (3 mins)	17.2 ± 2.4	-	-	-	-	-	-	-
		UV	-	8.0 ± 1.4/ 1.08 ± 0.07	-	-	-	-	-	-
		Sonolysis	16.9 ± 2.1	-	-	-	-	-	-	-
	tri-sodium citrate [1.94 mM]	Thermal	11.0 ± 1.9	-	-	-	-	-	-	-
		MWA (3 mins)	11.6 ± 0.9	-	-	-	-	-	-	-
		UV	-	10.8 ± 2.4/ 1.37 ± 0.26	-	-	-	-	-	-
		Sonolysis	18.0 ± 5.0	-	-	-	-	-	-	-
	tri-sodium citrate [3.88 mM]	Thermal	11.9 ± 2.0	-	-	-	-	-	-	-
		MWA (3 mins)	11.3 ± 1.6	-	-	-	-	-	-	-
		UV	-	10.9 ± 2.3/ 1.56 ± 0.56	-	-	-	-	-	-
		Sonolysis	17.9 ± 6.1	-	-	-	-	-	-	-
	cyclohexanone‡ [0.48 M]	-	43 ± 7 [≈ 50%]	-	41 ± 9 [≈ 20%]	32 ± 5 [≈ 5%]	35 ± 5 [≈ 5%]	-	275 ± 50 [≈ 5%]	325 ± 75 [≈ 5%]
	acetone [2.72 M]	MWA (6 mins)	68.5 ± 7.7 [75 %]	-	65.9 ± 8.8 [9 %]	66.9 ± 10.8 [4 %]	97.3 ± 14.3 [4 %]	120 ± 20 [3 %]	200 ± 36 [6 %]	-
	acetone [0.68 M]		49.0 ± 10.6 [60 %]	-	53.0 ± 15.1 [6 %]	52.2 ± 16.6 [23 %]	-	64.1 ± 37.5 [2 %]	130 ± 24 [8 %]	-
	acetylacetone [0.49 M]		50.3 ± 9.8 [35 %]	-	32.9 ± 7.4 [23 %]	39.2 ± 7.5 [16 %]	61.1 ± 13.1 [9 %]	39.5 ± 37.5 [4 %]	71.9 ± 9.1 [14 %]	-
	2-pentanone [0.47 M]		-	21.8 ± 4.3/ ≈ 1 – 3 [36 %]	29.0 ± 4.1 [17 %]	31.6 ± 3.3 [24 %]	35.3 ± 2.6 [7 %]	34.8 ± 2.7 [3 %]	49.3 ± 6.1 [12 %]	-

In the next chapter we will begin our investigations of core-shell silver-gold and gold-silver particles. We will start with the case of silver core- gold shell nanoparticles and investigate the effect of changing the gold/ silver ratio on the physical properties of the colloids and their functional capacity to enhance the absorption of methylene blue dye. In the penultimate section we will revisit traditional methods in forming gold core- silver shell particles and briefly investigate the effect of changing metal concentrations and ascorbic acid as an additive.

5. New routes to the controlled growth of core-shell silver-gold and gold-silver nanoparticles

5.1. Overview

Recently, a lot of attention has been paid to the synthesis and characterisation of bimetallic nanoparticles due to their unique catalytic, electronic, optical, structural, and thermal properties[126–128] as well as their technological applications as catalysts,[129–132] sensors,[133] within nano-electronic devices,[134–136] or as biosensors.[137] It is the current understanding that the versatility of nano-materials may be attributed to their size and shape dependent properties;[136] however, the combination of noble metals, either as alloy or core-shell structures, are tuneable factors and also contribute to bimetallic systems.[138–140] There are five different cases of bimetallic nanoparticle that can form. An example for a gold and silver bimetallic nanoparticle is shown in Scheme 5.1.1.

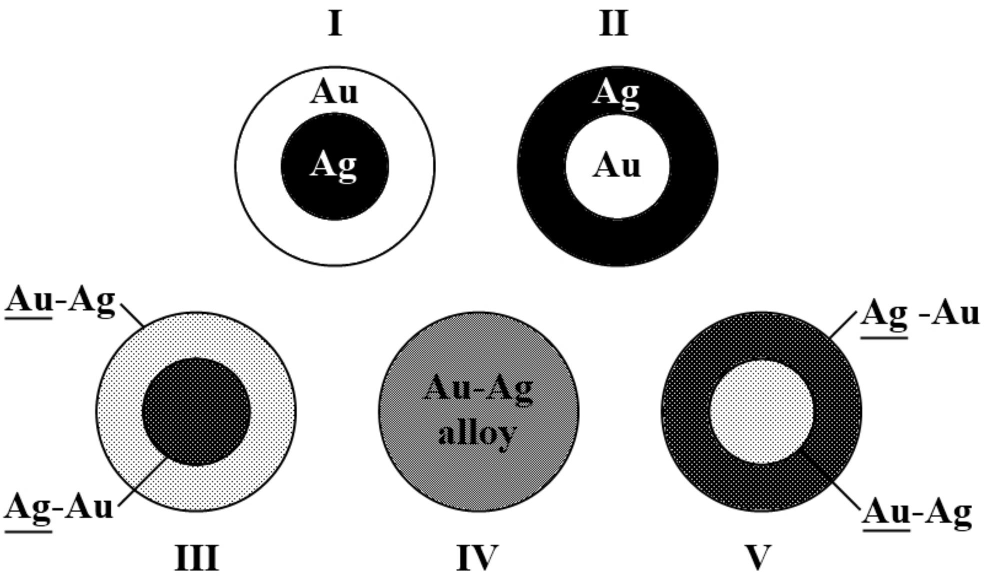

Scheme 5.1.1: A diagram depicting the five different types of bimetallic nanoparticle that can form when gold and silver constituents are combined. Type I = Ag core - Au shell, Type II = Au core – Ag shell, Type III = Ag rich core – Au rich shell, Type IV = pure Au – Ag alloy, Type V = Au rich core – Ag rich shell.

There have been several studies of bimetallic noble metal nanoparticle including combinations of Pt-Ru, Cu-Pd, Pt-Mo, Pt-W, Pt-Ni, and Au-Ag.[141–144] The Au-Ag system has been the most extensively studied due to the fact that both Ag and Au nanoparticles display distinctive optical plasmon absorbances in the visible region.[145,146] The optical and catalytic properties of Ag and Au nanoparticles have been demonstrated for use in a wide range of applications.[7,22]

Current research has employed Au and Ag nanoparticles for the destruction of bacteria,[147–150] photo-switches,[151] improvements in detection of cancer,[152] DNA[153] and single molecules by surface enhanced Raman spectroscopy (SERS)[154] and for improving the optical properties of thin-film semiconductors by forming composites.[12,155–159] By combining these two metals into a single entity, catalytic properties can be further enhanced[132] and localized surface plasmon absorption can be tuned continuously between the two limits of monometallic Au and Ag.[160]

In the bulk, Ag and Au form alloys for all compositions with very little surface segregation. This is due to their analogous face-centred cubic packing of almost identical lattice size (Ag = 4.068 Å, Au = 4.078 Å)[161] and similar chemical properties.[162] Nanoparticles with either alloyed (Scheme 5.2.1, Type IV),[163–173] or core–shell segregated structures (Scheme 5.2.1, Type I and II) can be synthesized by a variety of techniques.[174,175] The most common method for forming Au-Ag nanoparticle alloys involves a Turkevich-type co-reduction of auric acid and silver nitrate in the presence of a stabilising agent such as tri-sodium citrate in water or micro-emulsions.[163–165] A variety of other synthetic routes to bimetallic Au-Ag alloys have been developed, including inverse micelle methods,[167] replacement reactions,[168] laser-assisted formations,[170] alcohol[169] or borohydride reductions,[171] laser ablation,[166] ultrasound irradiation[172] and metal evaporation-condensation reactions;[173] where the synthesis of core-shell nanoparticles is dominated by two-step seed mediated processes.[174,175]

5.2. Introduction

In this Chapter we will investigate two new methods for producing core-shell colloids of gold and silver. The first part, Section 5.3, deals with the one-pot synthesis of silver-gold core-shell nanoparticles. Five types of particles were made, ranging from pure gold at one end of the spectrum, through three kinds of core-shell of varied composition, to pure silver at the other end of the spectrum. The size and shape of three colloids were investigated, that of the pure gold, pure silver and the 50: 50 silver-gold core-shell. Moreover, their interaction with methylene blue dye was assessed for their potentially increased functionality as light activated agents in the lethal photosensitisation of bacteria. The second part, Section 5.4, deals with the two stage synthesis of gold-silver core-shell nanoparticles. This was achieved using a modified two-stage synthetic route that yielded primarily spherical Au-Ag core-shell particles. The gold cores were formed through the co-reduction of auric acid by tri-sodium citrate. The silver coating was formed over these gold cores using silver nitrate, tri-sodium citrate and ascorbic acid. The effect of altering the reagent concentrations during the silver coating stage was studied. An interesting effect was observed where increasing levels of ascorbic acid led to the progressive increase in the central position of the SPR band, its absorbance and the radius of the encapsulating silver shell. These observed trends were compared with relevant examples in the literature.

5.3. One-pot synthesis of silver-gold core-shell nanoparticle solutions and their interactions with methylene blue dye

5.3.1. Overview

A one-pot modified Turkevich synthesis was used to synthesise a range of colloids from pure Ag, through core-shell Ag-Au mixtures to pure Au by addition of tri-sodium citrate to auric acid and silver nitrate mixtures.

The colloids were analyzed by X-ray diffraction (XRD) and wide-beam energy dispersive X-ray (EDX) analysis. UV-visible spectroscopy showed a non-linear variation in surface plasmon resonance band with Au: Ag ratio consistent with core-shell formation. High resolution transmission electron microscope (HRTEM) images in conjunction with thin-beam EDX line analysis confirmed the presence of predominantly Ag cores and Au exteriors in the nanoparticles. Argon ion sputtering with X-ray photoelectron spectroscopy (XPS) measurements of particles also indicated Ag-Au core-shell formation. Ag (0), Au (0) and significant levels of Au (I) states were observed, correlating with a Ag-Au core-shell model where the gold shell is partially oxidised at the surface. Subsequent titration of the colloids with methylene blue (MB) dye showed strong positive increases in the extinction coefficient at the MB absorption maximum. At the optimum levels of dye addition a linear relationship was found between average nanoparticle size and the number of dye solvation shells. Pure Au and Ag colloids showed the greatest propensity for an increase in extinction coefficient of MB due to an enhanced transfer of surface plasmons to localised dye molecules and demonstrate the potential for increased functionality as light activated agents in the lethal photosensitisation of bacteria.

5.3.2. Introduction

The synthesis of core-shell nanoparticles is dominated by two-step seed mediated processes.[174,175] In order to further simplify the synthesis of core-shell particles we developed a one-pot synthetic route to silver-gold core-shell particles. This was based on the most common route to the formation of Au-Ag alloys, which involves the co-reduction of auric acid and silver nitrate in the presence of a stabilising agent such as tri-sodium citrate in water/ micro-emulsions.[163–165] In this section we present a new reduction method for the one-step production of Ag-Au core-shell nanoparticles through a modified Turkevich approach. The cores and shells of the particles primarily consist of Ag and Au respectively (Scheme 5.1.1, Type III). Near monodispersity of the particles was achieved by prolonging their reflux. The colloids of varying Au-Ag ratio were characterised using UV-visible spectroscopy, energy dispersive X-ray (EDX) analysis, X-ray diffraction (XRD), X-ray photoelectron spectroscopy (XPS) and high resolution transmission electron microscope (HRTEM) equipped with a thin-beam EDX probe. The formation of core-shell particles in this one-step synthesis also sheds light on the kinetics of the reaction mechanism; the rate of reaction of silver nitrate was found to be more rapid than auric acid under the conditions imposed.

Dyes deposited onto the surface of Au or Ag metal generally display a change in their intensity of colouration.[176] This is due to an electronic transfer from the metallic surface to the absorbed dye. Similarly, Au, Ag and Au-Ag alloy colloidal nanoparticles also demonstrate this phenomenon when dyes are deposited onto their surface.[177–179] For anionic dyes, such as cyanine, a decrease in the colour intensity is observed. This is because the electronic transfer from the interacting nanoparticle inhibits colour processes due to columbic repulsion.[177] The reverse effect is observed for cationic dyes such as methylene blue (MB), where an increase in the colour intensity is observed on interaction with the metallic surface.[178] This is because the electronic transfer from the interacting nanoparticle enhances absorption of light by the dye molecules. Such positive interactions have proved very important in the use of MB dye absorbed on gold nanoparticles as tags for the enhanced SERS detection of molecular species.[180] They have also enhanced the efficacy of MB in its light-activated lethal photo-sensitization of bacteria potency in the destruction of bacteria.[181] It was only recently demonstrated that Methylene blue (MB) dye was capable of acting as a light activated agent in the lethal photo-sensitization of bacteria.[182,183] When light is absorbed by the dye, excited triplet states are formed that interacts with oxygen to generate singlet oxygen species. Singlet oxygen is a highly reactive and can damage cell walls, plasma membranes and DNA, leading to cell death. By enhancing the level of light that MB can absorb, through its absorption and interaction with nanoparticles, greater levels of singlet oxygen production leading to increased bacterial kills have been observed.[184] The change in the optical properties of cyanine dye absorbed on various colloidal Au-Ag composites has been investigated.[177] However, to our knowledge, the possible enhancement in the optical properties of MB dye absorbed on Ag-Au core-shell nanoparticles has not been reported.

The interaction of MB dye with our silver-gold core-shell particles was compared with pure Ag and pure Au nanoparticle solutions of equal concentration by UV-visible spectroscopy. It was shown that the extinction coefficient of MB dye could be significantly enhanced when combined with core-shell structures, however, the pure Ag and Au colloids showed more significant enhancements. To our knowledge, this is the first report of Ag-Au core-shell nanoparticles that have been synthesised in a single step without the use of seeds.

5.3.3. Experimental

All reagents were purchased form Sigma-Aldrich UK unless otherwise stated.

5.3.3.1. Synthesis

All glassware was cleaned with aqua regia (3HCl: $1HNO_3$) and rinsed with copious amounts of deionised water prior to use. Aqueous silver nitrate, auric acid and sodium citrate stock solutions were made up. The silver nitrate and auric acid stock solutions consisted of $AgNO_3$ (85 mg) and $HAuCl_4.3H_2O$ (170 mg) respectively. The solutions were dissolved up to a volume of 100 ml with distilled water making 5 mM solutions. The sodium citrate stock solution consisted of $Na_3C_6H_5O_7.2H_2O$ (250 mg) dissolved in 50 ml of distilled water (20 mM). Pure nanoparticle solutions of either gold or silver were synthesised by dissolving 2 ml of the appropriate metal stock solution in 16 ml of distilled water and uniformly heating in an oil bath with constant stirring. At boiling, 2 ml of the citrate stock was injected into the solution. The solution, with continuous stirring, was refluxed for 1 hour to ensure complete ripening of the colloid before removal from the oil bath. Colour changes in solution characteristic of gold and silver nanoparticle formation were observed, changing from colourless to lilac to pink to red for the gold synthesis and from colourless to brown for the silver synthesis. After cooling to room temperature, the concentrated nanoparticle solution was diluted to a total volume of 40 ml (0.28 mM metal content). Upon dilution, gold solutions became a more pale red and silver solutions a dark yellow. By mixing specific amounts of gold and silver stock solution, to a total volume of 2 ml, silver-gold core-shell nanoparticles of varying molar ratio were synthesised analogously. The colours of eventual solutions varied, graduating from pale red in pure Au nanoparticle solutions to dark yellow in pure Ag nanoparticle solutions.

5.3.3.2. Analysis

The surface plasmon resonance profile of each colloid was measured using a PerkinElmer Lambda 25 UV/VIS spectrometer over the 190 - 1000 nm range. Prior to further characterisation, samples were purified by centrifugation. Solutions were first spun at 20,000 rpm (≈ 48,000 x g) for 30 mins on a Beckman Coulter Avanti Centrifuge J-26 XP causing the nanoparticles to rest at the bottom of the container. The solution was replaced with fresh distilled water to remove any un-reacted reagents and salt by-products. The process was repeated twice more to ensure that the solutions were free from contaminants. Particle sizes and core-shell structures were investigated using high resolution transmission electron microscopy with a Jeol 4000EX HRTEM machine at Oxford University. The composition of the core-shell particles was analyzed using a Jeol JEM-2010 equipped with a thin-beam (diameter ≈ 5 nm) EDX probe, also at Oxford University. Samples for TEM analysis were prepared by evaporating purified solution droplets onto lacey carbon film coated copper grids.

For wide-beam (diameter ≈ 10 µm) energy dispersive X-ray (EDX) analysis, X-ray photoelectron spectroscopy (XPS) and glancing angle X-ray diffraction (XRD) a concentrated stack of nanoparticles was required. This was formed by continuously casting droplets of the colloid onto a silica substrate until a dark layer was observed. The EDX analysis was performed on a Jeol-6301F field emission instrument. The XPS analysis was performed at Cardiff University using a Kratos Axis Ultra-DLD photoelectron spectrometer using monochromatic Al-K_α radiation. Survey and high resolution scans were performed before Ar-ion sputtering (90 s) the surface for a total of 3 cycles to attain a compositional profile. Survey scans were collected in the range 0 - 1200 eV (binding energy) at a pass energy of 160 eV. Higher resolution scans were recorded for the principle peaks of Au (4f), Ag (3d), C (1s), O (1s) and Si (2p) at a pass energy of 40 eV. The peaks were modelled using CasaXPS software to determine elemental environment and concentration.[185] Peak positions were adjusted to adventitious carbon (graphite) and peak areas were adjusted using sensitivity factors to determine composition.[186] The XRD analysis was conducted using micro-focus Bruker GADDS powder X-ray diffractometer with a monochromated Cu $K_{\alpha 1}$ (1.5406 Å) source and CCD area X-ray detector capable of 0.01° resolution in 2θ. The diffraction patterns were compared with database standards for bulk gold and silver standards and further analysed by comparison with a Le Bail refined model[187] using the GSAS and EXPGUI software suite.[188]

5.3.3.3. Methylene blue dye titrations

A 20 ml aliquot of the nanoparticle solution was titrated with a stock solution of methylene blue (MB) dye. This was made by dissolving 0.46 ml of a concentrated (1% w/v) MB solution (purchased from Alfa Aesar - Johnson Matthey) up to 100 ml in volume with distilled water. From the stock solution, a 0.25 ml aliquot was added to the nanoparticle solution being tested and then shaken thoroughly. A 3 ml portion was removed for assessment by UV-visible spectroscopy and then returned to the solution for further additions. The process of addition, mixing and assessment was repeated until the surface plasmon resonance (SPR) band from the nanoparticle colloid was completely quenched.

5.3.4. Results and discussion

Gold, silver and gold-silver colloidal nanoparticles were prepared by co-addition of sodium citrate stock solution to heated auric acid and silver nitrate mixtures of predetermined ratio: (i) 100% Au, (ii) 75% Au: 25% Ag, (iii) 50% Au: 50% Ag, (iv) 25% Au: 75% Ag and (v) 100% Ag. Solutions were refluxed to encourage monodispersity through digestive ripening.[189] The colours of the solutions ranged from pale yellow (pure Ag) to pink/ red (pure Au) with intermediate hues in between (Figure 5.3.4.1).

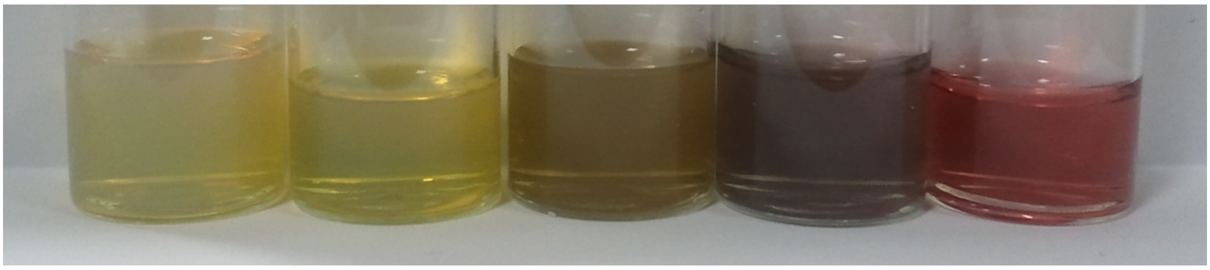

Figure 5.3.4.1: Au, Ag and Au/Ag core-shell (Ag core-Au shell) colloidal suspensions were prepared by a modified Turkevich thermal co-addition of sodium citrate solution to auric acid and silver nitrate mixtures of predetermined Au: Ag ratio; 100% Au, 75% Au: 25%Ag, 50% Au: 50% Ag, 25% Au: 75% Ag and 100% Ag. Solutions are displayed in the image above from greatest silver content on the left (Ag 100%) to greatest gold content on the right (Au 100%).

The spectroscopic profile of each colloid was assessed by UV-visible spectroscopy. A stacked plot of the spectral profiles is shown in Figure 5.3.4.2(a). The absorption of each pattern has been normalised to the height of their SPR band. From pure Ag to pure Au a general trend for increasing SPR band centre (nm) was seen. Slight side bands were also observed at ≈ 320 nm in both the 25% Au: 75% Ag and 100% Ag samples. This indicated that the size distribution of nanoparticles did not conform to the typical Gaussian distribution that is often seen. This did not indicate that nano-rod shapes had formed. Even though two plasmon band centres are typical for nano-rods, they normally differ quite considerably in wavelength (*i.e.* one SPR band centres in the visible and another in the IR region that originate from the asymmetry of the rods).[70] The wide SPR bands seen in the 75% Au: 25% Ag and 50% Au: 50% samples indicated a comparatively broader range of particle sizes formed and increased polydispersity. Each colloid displayed a single prominent SPR band centre. This showed that the solutions did not consist of mixtures of pure Au and Ag nanoparticles as such solutions would show individual SPR bands at *c.a.* 385 nm for Ag and *c.a.* 520 nm for gold. Where Au-Ag bimetallic nanoparticles form alloys, a linear relationship between the surface plasmon resonance centre and Au/Ag metal content is observed.[190] However, a non-linear relationship between the plasmon resonance centre and Au/Ag metal content was observed in this study, as shown in Figure 5.3.4.2(b). This indicated core-shell particles had formed, as predicted by Mie theory.[191] The relationship fit a Boltzmann model with good agreement ($r^2 = 0.98$). The slight blue-shift in SPR centre of the 25% Au: 75% Ag sample compared to that of pure silver was attributed to significant differences in average nanoparticle diameters.[192] Although the metal concentrations were equivalent; the SPR absorbance of pure Ag nanoparticles was far greater than that of pure Au, with a steady decrease in overall absorbance for the Au-Ag core-shell colloids with increasing Au content.

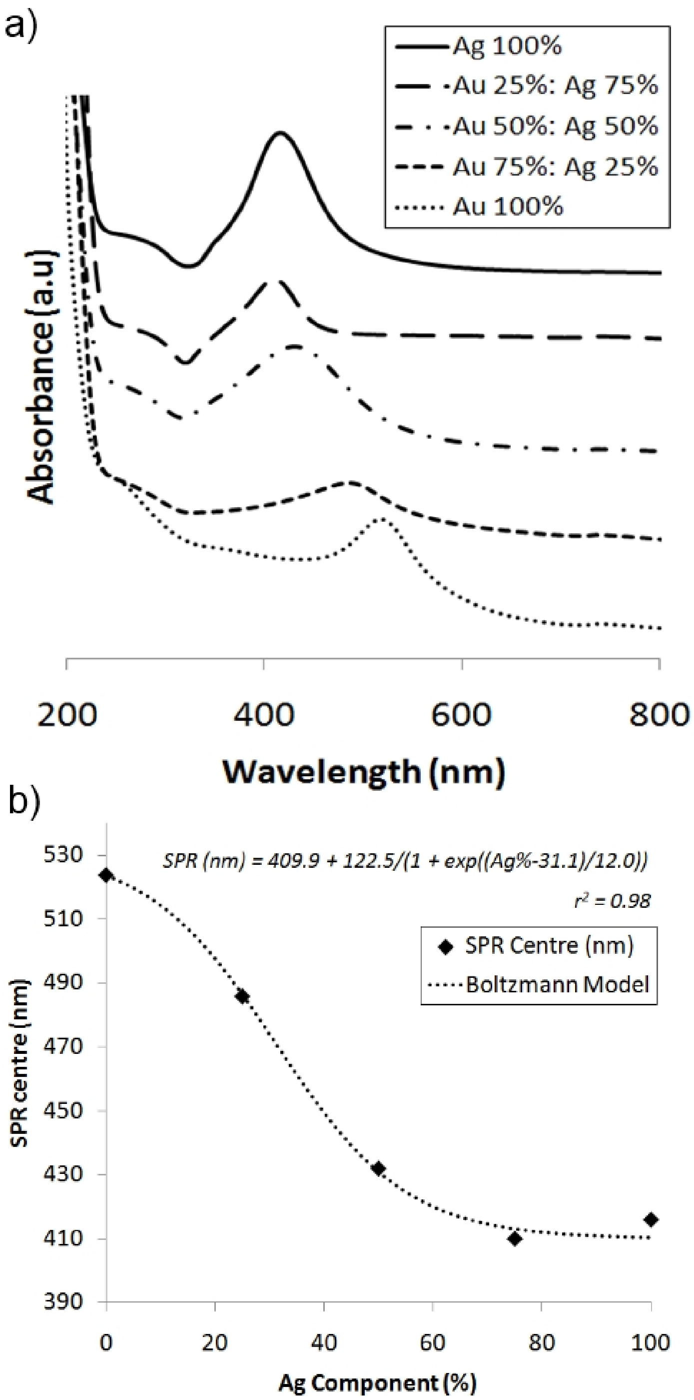

Figure 5.3.4.2: (a) A stacked plot of normalised UV-visible absorption spectra and (b) the resulting SPR centres against Ag % content for pure Au, Ag and the Au/Ag core shell nanoparticle colloids synthesised by a modified Turkevich thermal co-reduction of auric acid and/or silver nitrate mixtures.

The XRD patterns of the colloids formed in this study were of face-centred cubic (FCC) symmetry, analogous to their bulk gold ($FM\bar{3}M$, a = 4.083 Å) and silver ($FM\bar{3}M$, a = 4.068 Å) counterparts. A stack of the corresponding diffraction patterns are displayed in Figure 5.3.4.3.

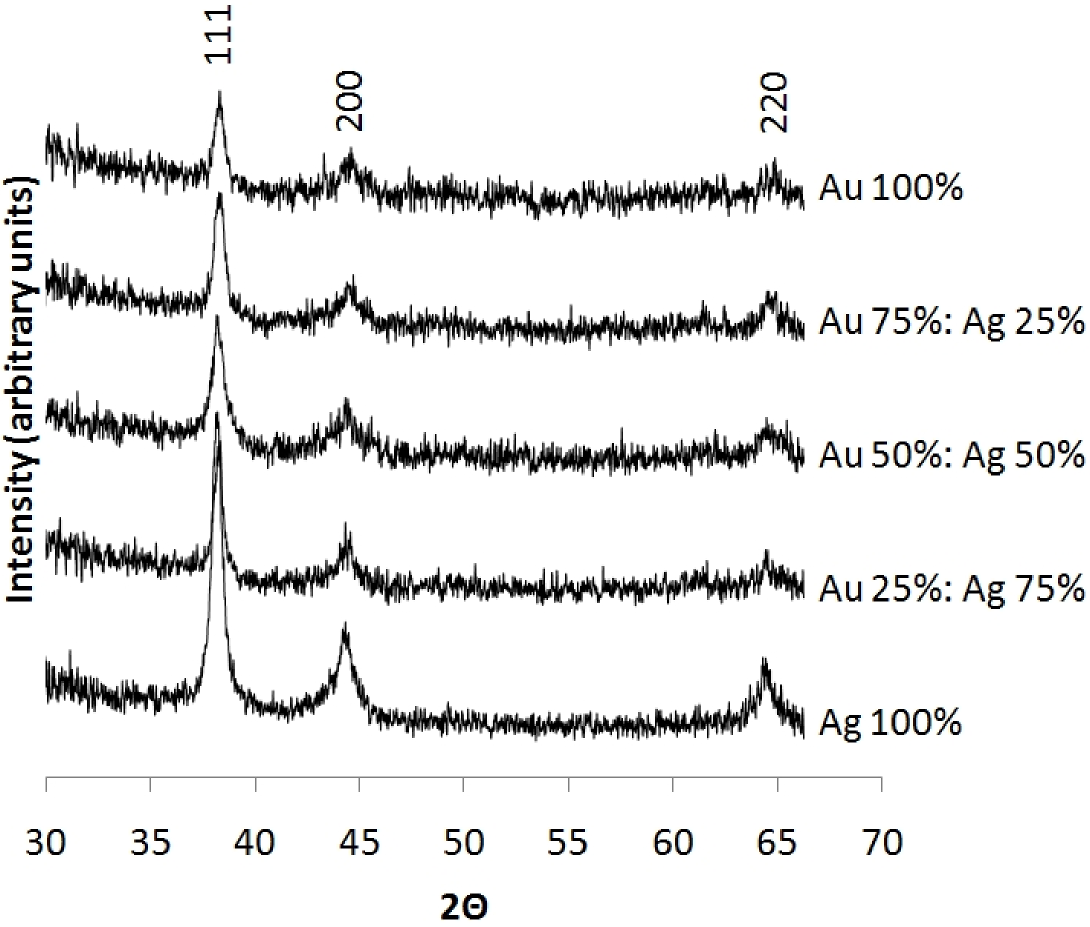

Figure 5.3.4.3: Stack of the XRD diffraction patterns acquired from Au, Ag and Au-Ag core-shell (Ag core-Au shell) colloidal suspensions deposited on silica. The nanoparticles were synthesised by a modified Turkevich thermal co-addition of tri-sodium citrate to auric acid and silver nitrate mixtures of predetermined Au: Ag ratio.

The X-ray diffraction data was fit to a Le Bail refined model.[188] An increase in the unit cell lattice parameter *a* was observed with increasing gold content (Table 5.3.4.1). This was attributed to the larger ionic radius of Ag over Au.[161] The diffraction peaks were broad, characteristic of nanoparticulate materials due to the small crystallites formed. By assessing the widths of the dominant diffraction peak of (111) symmetry the average crystallite size was quantified using the Scherrer equation.[193] The X-ray diffraction patterns did not show separate peaks for Au-FCC and Ag-FCC formation. Such should be the case for Ag-Au core-shell growth. In fact, the unit cell lattice parameter *a* increased steadily with increasing Au content, completely in line with Vegard's law of alloy formation.[194] However, the resolution of the X-ray diffraction apparatus was not sufficiently high to distinguish between overlapping peaks, especially given their broadness due to their low crystallite size. A list of the X-ray diffraction parameters and average crystallite sizes are shown in Table 5.3.4.1.

Table 5.3.4.1: The UV-visible spectroscopic SPR centres (nm), Au content (%),unit cell lattice parameters *a* and crystallite Scherrer width (nm), HRTEM determined average particle diameters (nm) and maximum absorbance increases and changes in the extinction coefficient ε ($M^{-1}cm^{-1}$) from methylene blue titrations for the nanoparticle colloids synthesised by a one-pot citrate co-reduction reaction of auric acid and/or silver nitrate.

		Ag 100%	Au 25%: Ag 75%	Au 50%: Ag 50%	Au 75%: Ag 25%	Au 100%
Au (%) component		0 ± 0	27.3 ± 1.1	51.4 ± 3.9	72.3 ± 5.3	100 ± 0
Unit cell length *a* (Å)		4.068 (1)	4.072 (1)	4.078 (1)	4.079 (1)	4.083 (1)
Average crystallite size (nm)		13	15	10	13	13
Average particle diameter (nm)		31.4 ± 12.7	-	46.2 ± 11.7	-	22.7 ± 3.0
SPR centre (nm)		416	410	432	486	521
Maximum increase in methylene blue dye absorbance	MB: metal	0.0144	0.0199	0.0146	0.0126	0.009
	Δ Abs	0.54	0.49	0.47	0.47	0.45
	Δ ε	1.54 x 10^5	1.53 x 10^5	1.34 x 10^5	1.43 x 10^5	1.64 x 10^5
	% ε	216	213	187	200	229

A wide-beam (≈ 10 µm diameter beam) energy dispersive X-ray (EDX) analysis of the colloids revealed compositions close to the predetermined Au: Ag ratios (Table 5.3.4.1). The samples were cleansed prior to analysis by several cycles of centrifugation. This allowed any un-reacted tri-sodium citrate reductant, metal ions and reaction by-products to be decanted from the solution. Therefore any presence of Au and Ag metal detected in these samples was due to incorporation within nanoparticles. This ultimately demonstrated the complete reaction of the metal precursors, regardless of the pre-formulated Au: Ag ratio, and full incorporation of the metals ions with the colloid.

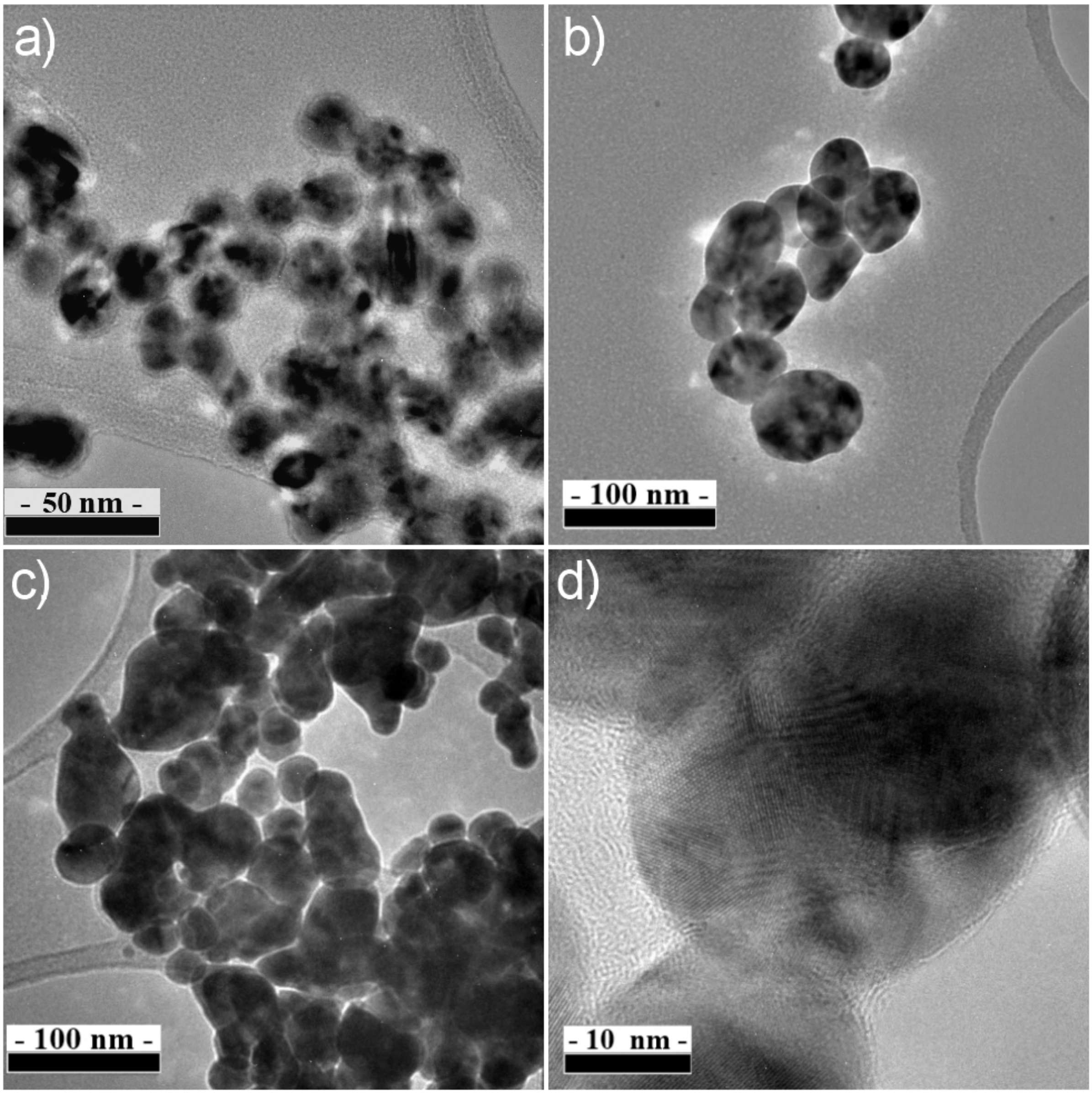

Figure 5.4.4: Representative HRTEM images of (a) the pure Au (Au 100%), (b) the pure Ag (Ag 100%)and (c) & (d) the 50: 50 Au: Ag mix (Au 50%: Ag 50%). Particles observed in the solitary metal colloids were primarily spherical, with deformed ellipsoids and "egg" shapes seen in the mixture. The colloids were synthesised by a modified Turkevich thermal co-addition of tri-sodium citrate to auric acid and silver nitrate mixtures of predetermined Au: Ag ratio.

The size and shape of nanoparticles in the pure Au (Au 100%), pure Ag (Ag 100%) and 50:50 Au: Ag mix (Au 50%: Ag 50%) were assessed by HRTEM. Figures 5.3.4.4 (a-c) show lower magnification images of Au 100%, Ag 100% and Au 50%: Ag 50% respectively. Particles formed in the solitary metal colloids were primarily spherical and of a narrow distribution of size. However, more ellipsoidal shapes were observed within the 50: 50 mixture, with a larger distribution of size.

A closer observation of this mixture at higher magnification revealed "egg" like structures with dense central cores due to the dark contrast (≈ 20 nm in diameter) and less dense outer shells. Such significant differences in TEM image contrast have previously been used to discern core-shell formation alone.[195] Although the lattice fringes were clearly discernible, HRTEM was unable to differentiate between the core and shell components because of the lack of distinctively different crystallographic features of Au-FCC and Ag-FCC structures. Nevertheless, the lattice fringes observed were of a similar size predicted by Scherrer X-ray diffraction line broadening (≈ 9.5 nm). The particle sizes from a series of images were measured for each colloid. For ellipsoidal particles, the average width about the symmetric horizontal and vertical axis was taken as the diameter. The median particle diameter ± the standard deviation error (nm) are listed in Table 5.3.4.1. The nanoparticles formed in the pure Au colloid (22.7 ± 3.0 nm) were significantly smaller and more monodisperse than those formed in the pure Ag (31.4 ± 12.7 nm) and 50: 50 mix (46.2 ± 11.7 nm). The pure Au colloid primarily consisted of spherical particles, with a mean elliptical aspect ratio of 1.08. The particles in the pure Ag colloid were more ellipsoidal and showed a larger aspect ratio of 1.21. However, the most elliptical particles were seen within the Ag-Au core-shell colloid, where a mean aspect ratio of 1.37 was observed.

In order to discern the nature of the Ag-Au core-shell structures observed by HRTEM, a TEM machine equipped with a thin-beam EDX probe was used to investigate the 50: 50 Au: Ag mix (sample Au 50%: Ag 50%). The EDX spectrum was acquired by focussing a thin beam (≈ 5 nm in diameter) across several positions along a particular core-shell structure. The ratio of percentage composition of Ag was determined from the viable counts of the Au M-Line and Ag L-Line excitations. From the variation in composition across particles (Figure 5.3.4.5), the results confirmed that the particles were core-shell in nature of the Type III (see Scheme 5.1.1). Although the clarity of the images was significantly lower on this instrument, the "egg" like shape of the core-shell structure was still clearly discernible (Figure 5.3.4.5(a)).

An increase in the level (number of viable counts) and composition (%) of Ag was observed on moving across the core-shell structure from position 1 to 3. Subsequent movements to positions 5 and 6 lead to sharp decreases in the level and composition of Ag. This indicated that the cores (position 3) were silver-rich. An inverse trend was observed for Au, where the composition minimised at position 3 (the centre of the particle) and increased towards the edges at positions 1 and 6. Given wide-beam EDX analysis results demonstrated an approximately 50: 50 incorporation of Ag: Au in the overall bimetallic colloid, this particular nanoparticle in question was noticeably silver rich along the axis analysed.

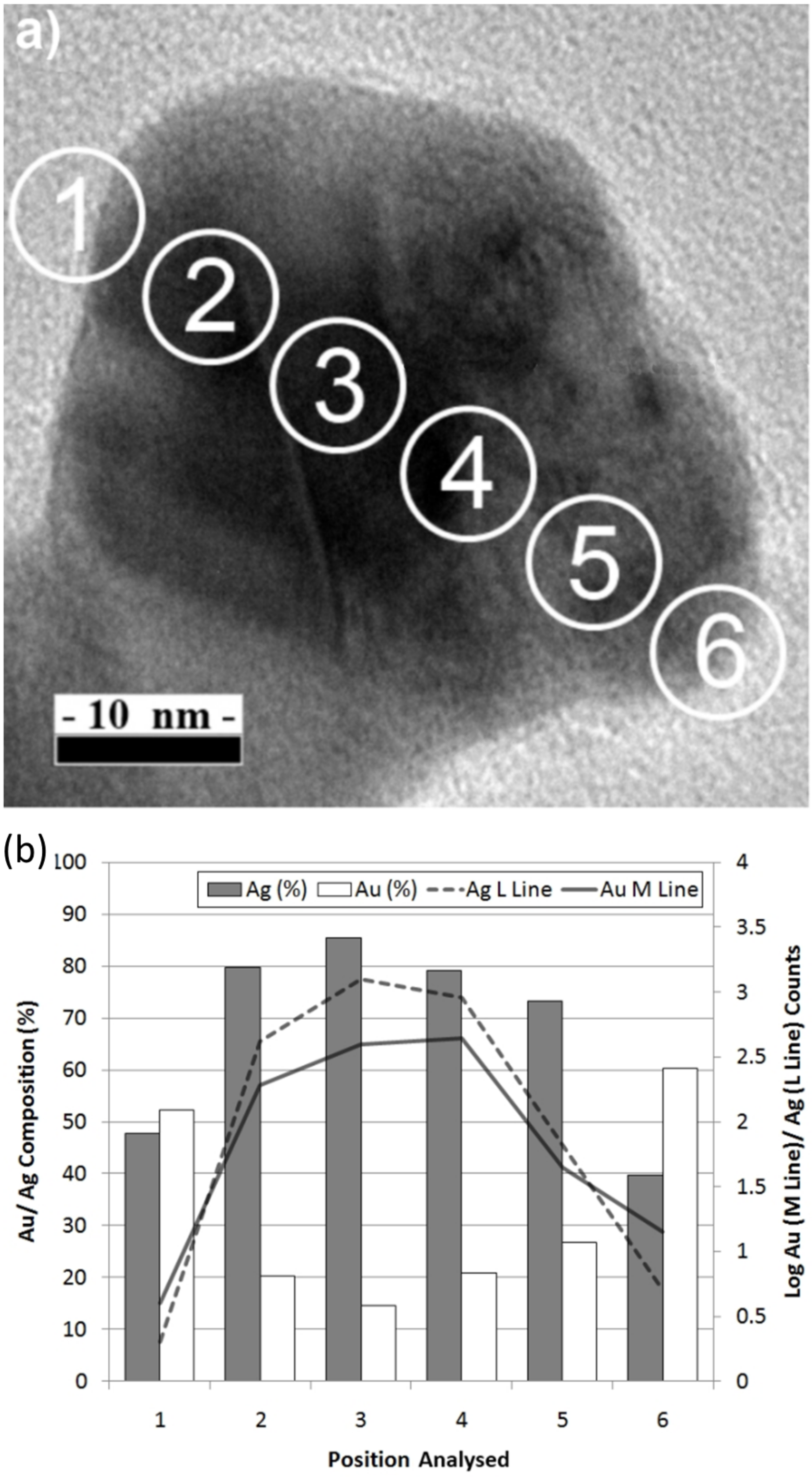

Figure 5.3.4.5: (a) A lower magnification of the TEM image of the Au-Ag core-shell structure with labels that show where thin-beam (≈ 5 nm) EDX analysis was conducted on an individual particle from the Au 50%: Ag 50% colloid. (b) The levels (Au/Ag counts) and the Ag composition (%) for each of the positions analysed. The core-shell particles were synthesised by a one-pot thermal co-addition of tri-sodium citrate to a 1: 1 mixture of auric acid and silver nitrate.

The fact that the number of counts from Au M-Line and Ag L-Line emissions increased by 3 orders of magnitude from position 1 to the middle positions of the nanoparticle and then decreased 3 orders of magnitude from the middle to position 6 was attributed to the round shape of the spherical particle. Four additional particles were assessed in an analogous manner. A dominant Ag core was observed in each case as well. Nevertheless, both Ag and Au in approximately equal ratio were detected in the outer shells of the particles. Although the EDX beam was fine-tuned to a diameter of 5 nm, it was not possible to discern how much of the particle was excited upon impact. It could not be explicitly discerned whether the core-shell particles formed were purely of a Ag core and Au outer shell. As an equivalent level of Au and Ag was incorporated into these particles, as seen from our wide-beam EDX analysis (≈ 10 µm) of a large number of particles simultaneously, in addition to the cores being predominantly made of Ag, it was apparent that these core-shell particles consisted of a predominantly Ag core and Au rich shell (core-shell Type III structure; see Scheme 5.1.1).

Au-Ag particles have previously been characterised using a wide-area EDX analysis method (bulk analysis) in conjunction with X-ray photoelectron spectroscopy (XPS), a surface analytical technique, to confirm the presence of core-shell structures.[196] Although this method confirmed the solitary presence of a gold shell, transitional changes from the core outwards could not be assessed in the way that they were in this study. Au-Ag core-shells have also previously been assessed by TEM imaging alone.[195] By modelling the change in image contrast, the presence of Au cores and Ag shells were determined, however, the level and composition of Au and Ag could not be quantified. Sajanlal *et. al.* used the thin-beam EDX technique, analogous to that used in this study, to assess changes in composition of Ag-Au core-shell micron-sized mesoflowers.[197] Although Sajanlal *et. al.* mapped the levels of Au and Ag over a large number of pixels, such a technique could not be applied in this study due to the significantly smaller size of our particles (nanometre scale) compared with his (micrometre scale) and the low counts that resulted.

XPS was used to investigate the oxidation states of the noble metal species in sample Au 50%: Ag 50%. Given the surface sensitivity of XPS, where chemical information from only the topmost layers of the sample is acquired (typically only a few nanometres deep), argon-ion sputtering was used to probe the bulk. A thin powder layer of the colloid was cast onto a silica support by continuously dropping solution droplets at the same location in-between evaporations. Adventitious graphite (1s) at a binding energy of 284.5 eV was observed in addition to organic carbon (1s) and carboxylic oxygen (1s) species at binding energies of 289.3 eV and 530.8 eV respectively. This was attributed to the citrate surfactant surface-layer.[198] No silicon environment

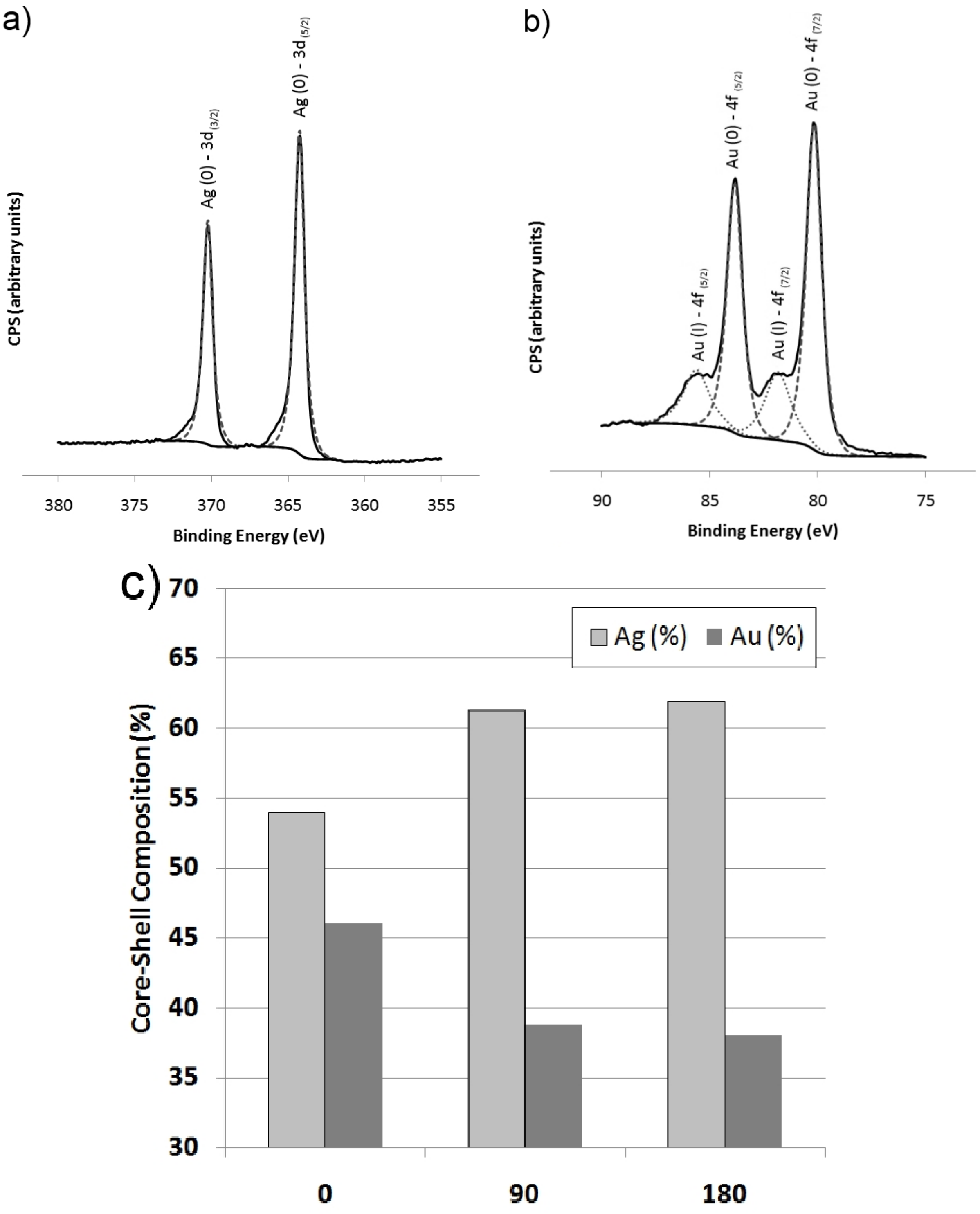

Figure 5.3.4.6: Example the high-resolution XPS scans of sample Au 50%: Ag 50% in the (a) Ag [3d] and (b) Au [4f] regions before Ar-ion sputtering. (c) A plot of the Ag/Au (%) against argon-ion sputtering time (s). The core-shell particles were synthesised by a one-pot thermal co-addition of tri-sodium citrate to a 1: 1 mixture of auric acid and silver nitrate.

from the underlying silica support was observed and demonstrated that the excitation layer originated solely from the colloidal stack of particles. Both silver and gold environments were detected with high intensity. This indicated that the excitation depth was strong enough to probe the cores of the core-shell particles (Figures 5.3.4.6(a) and 5.3.4.6(b)).

A solitary Ag (0) environment was observed in the 3d orbital excitation range at binding energies of 368.1 eV ($3d_{5/2}$) and 374.1 eV ($3d_{3/2}$).[199] Two distinct gold environments were observed in the 4f region. Predominantly Au (0) was observed at a binding energy of 84.0 eV ($4f_{7/2}$)[200] in addition to a minor fraction of Au (I) at a binding energy of 85.6 eV ($4f_{7/2}$).[201] The ratio of Au (0) to Au (I) was approximately 3: 1. As only Au was seen in both an oxidised and elemental state this further corroborated with evidence for core-shell formation; with Ag present at the core encapsulated by a Au shell. This is because the surface of a particle is most likely to become oxidised as opposed to the core. In fact, from looking at the chemistry of Ag and Au, Ag is far more liable to oxidise than Au, so seeing that only the Au had oxidised strongly points towards the formation of Ag core- Au shell particles (Type III, see Scheme 5.1.1).

Ar-ion sputtering was conducted for two 90 second cycles, with XPS scans in-between. The level of carbon and oxygen reduced considerably with each cycle. This was attributed to the removal of the citrate surfactant surface layer. No additional oxidation states for the metal environments were observed, however, the Ag: Au ratio increased with each cycle (Figure 5.3.4.6(c)). This was attributed to the removal of the Au-rich shell layers with each ion-bombardment, thus further confirming a Ag-rich core. Both alloyed Ag-Au and Au-Ag core-shell colloids have been formed by seed mediated syntheses conducted by Pande *et. al*.[202] These bimetallic colloids were also probed by XPS. However, both the alloyed and core-shelled materials showed only metallic environments of gold and silver, where no surface oxidation was observed. Contrary to our findings, Pande *et. al.* observed both gold and silver environments in equal ratio, demonstrating that the XPS excitations from the particles cores and shells were equally detected. By incorporating all evidence from our physical characterisations of sample Au 50%: Ag 50%, a schematic of these core-shell structures was drawn (Figure 5.3.4.7).

Au-Ag core-shell structures were previously formed by Yang *et. al.* using a seed-mediated synthesis.[175] Ag seeds were first formed by refluxing an aqueous solution of $AgNO_3$ with $NaBH_4$ and a tri-sodium citrate stabiliser. These seeds (≈ 9.6 nm in diameter) were then further refluxed in 1:1 ratio with $HAuCl_4$ and additional stabiliser to form monodisperse core-shells that were less than 9 nm in diameter. In our synthesis, $AgNO_3$ and $HAuCl_4$ salts were similarly reduced using tri-sodium

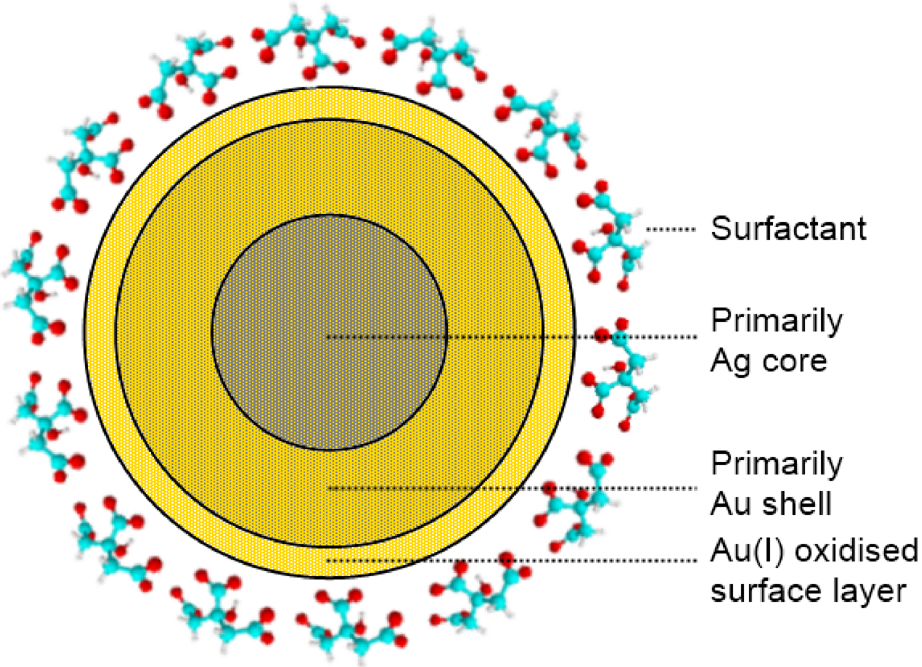

Figure 5.3.4.7: A diagram depicting the layers within the core-shell particles formed by a one-pot thermal co-addition of tri-sodium citrate to a 1: 1 mixture of auric acid and silver nitrate (sample Au 50%: Ag 50%). Particles were on average 46.2 ± 11.7 nm in diameter. The size of the Ag cores could not be determined as the transition between a primarily Ag core to a primarily Au shell was gradual (Type III core-shell, Scheme 5.1.1)

citrate, skipping the seed formation stage of Yang *et. al.*[175] Our synthesis resulted in core-shell particles of contrastingly different size (46.2 ± 11.7 nm average particle diameter). The formation of considerably smaller particles by Yang *et. al.* was attributed to the use of $NaBH_4$ in the seed formation stage, which typically encourages the formation of smaller colloids.[196] Similarly, Srnova-Sloufova *et. al.* synthesised Au-Ag core-shell colloids by a two-step seed mediated aqueous reaction of pre-formed Ag seeds (9 ± 2 nm) with $HAuCl_4$ and hydroxylamine reducing agent.[195] The resulting nanoparticles were also significantly smaller than those formed in this study, typically ranging from 8 – 12 nm in size. It was previously shown by Sanchez-Ramirez *et. al.* that thermal reaction of $HAuCl_4$ and $AgNO_3$ aqueous mixtures with tri-sodium citrate at very low metal concentrations can form Au-Ag alloyed colloids.[128] A linear variation of the SPR band centre and Au: Ag content was observed in their colloids, agreeing with a Mie theory model for the formation of an alloyed colloid. Although the same chemicals used in this study were used by Sanchez-Ramirez *et. al.*, a non-linear variation in SPR band centre with Au: Ag content was observed herein. This phenomenon had been previously associated in the literature with Ag-Au core-shell formation.[203] This was also confirmed in our study by a rigorous analysis of the particles using HRTEM, XPS and EDX thin-beam analysis. The difference between the two syntheses was the concentration of the metal sources and reductant, where in this study the reagents were 3 orders of magnitude more concentrated. Given the predominance of the Ag cores seen in this study, it was also reasonable to conclude that a significantly more rapid reaction of $AgNO_3$ with tri-sodium citrate compared with $HAuCl_4$ and tri-sodium citrate ensues under the experimental conditions imposed. The Ag-rich cores that initially form is then encapsulated by Au-rich shell layers from the more slowly reacting $HAuCl_4$.

5.3.4.1. Methylene blue dye titrations

The nanoparticle solutions were titrated against solutions of the cationic dye, methylene blue (MB). A UV-visible spectrum of aliquots taken between additions enabled the effect on the absorption of the dye at 662 nm (the absorbance maximum of the dye) to be assessed. An example of the MB titration against the Au 50%: Ag 50% core-shell nanoparticles is displayed in Figure 5.3.4.8 (a). A steady increase in the characteristic absorption profile of MB dye was observed with sequential additions. There was no apparent deviation from this characteristic profile, even at high MB loadings. This indicated that solely monomeric MB was present in solution since the dimer shows a strong absorbance maximum at approximately 620 nm.[204] However, a quenching of the colloid's SPR band of was observed. This indicated the dye was interacting with the nanoparticles.[205] The interactions caused an increase in the absorption maximum of the dye and demonstrated the excitation transfer from the metallic surface to an absorbing dye molecule. The point at which the maximum increase in this absorption occurred was determined by plotting the MB/ metal ratio against the increase in dye absorption (Figure 5.3.4.8(b)). For the case of sample 50% Au: 50% Ag, the greatest MB absorption increase was observed at a MB/metal ratio of 0.0146. This optimum corresponded to ≈ 14 MB dye molecules interacting with 1000 metal atoms. Almost concordantly at this position, the greatest quenching in the SPR band was observed. All of the colloids had a positive effect on the absorbance maximum of MB, yet by differing degrees (Table 5.3.4.1). At the absorbance maximum, the true difference between the extinction coefficients of the dye and the sample was determined by a simple subtraction, taking the original absorbance from the colloid into account. This was then converted into a percentage increase due to metal–dye interactions relative to MB dye in water alone, so that true comparisons with the literature could be made.

Comparing all titrations, the maximum increase in dye absorbance (0.54 absorption units) was seen in the titration of the pure silver colloid (Ag 100%). A trend was observed whereby the absorption maximum decreased with increasing gold content. However, the MB concentration that was present in the solution at this optimum should be taken into account in order to provide a more comparable quantity, namely, the percentage increase in the extinction coefficient of the dye (% ε). This meant that although the lowest dye absorbance increase was observed in the pure gold sample (0.45 absorption units), when the MB/ metal ratio at this absorbance maximum was taken into

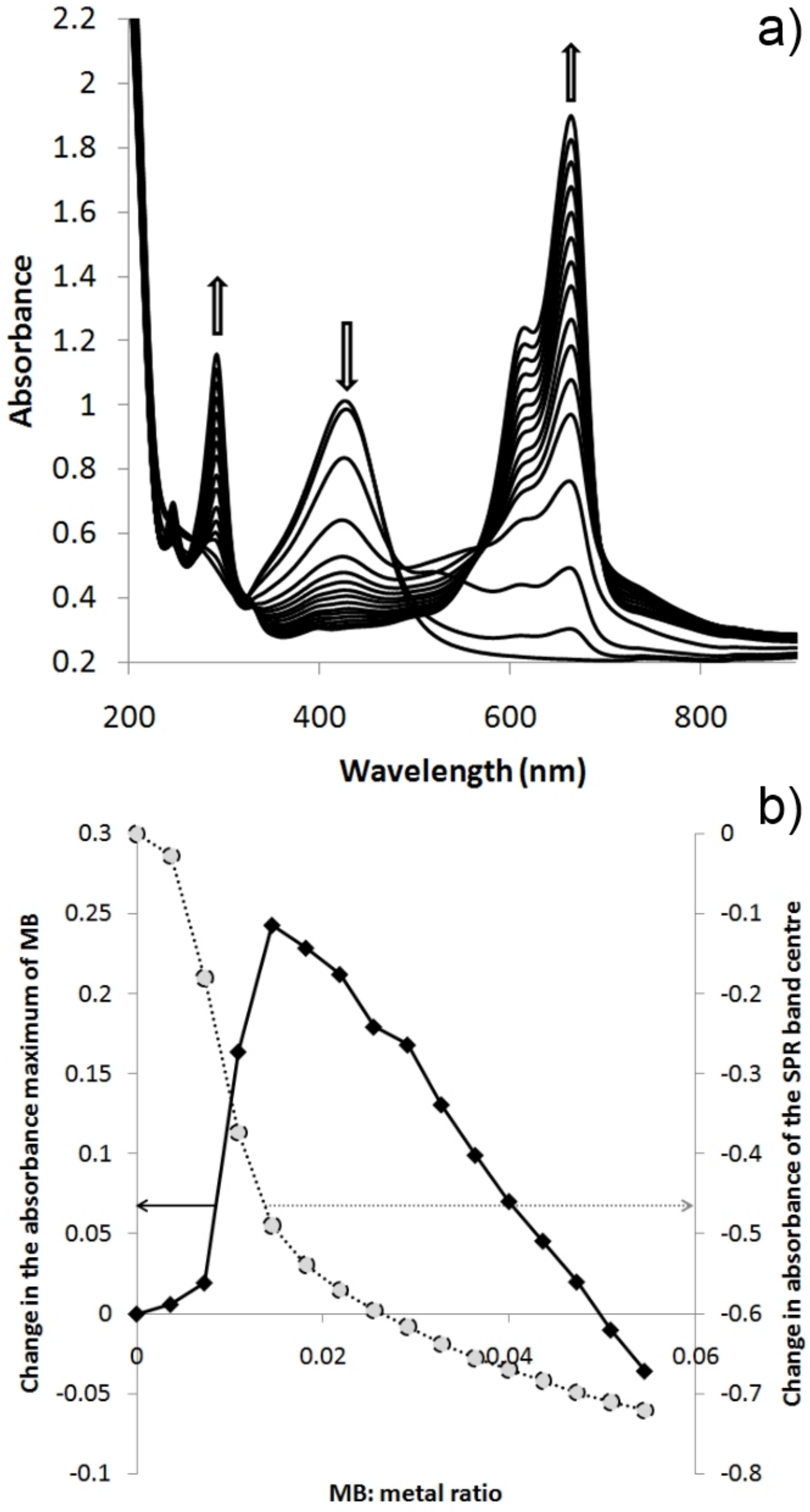

Figure 5.3.4.8: (a) UV/visible spectra obtained between MB dye additions to a 20 mL aliquot of sample Au 50%: Ag 50% and (b) the magnitude of the MB increases at 662 nm compared with a standard solution alongside the quenching of the SPR band centre at 432 nm against the MB/ metal ratio. The absorbance maximum occurred at a MB/ metal ratio of 0.0146.

account (lowest MB/ metal ratio of the series, 0.0090), the most significant percentage increase (229 %) in the extinction coefficient of the dye was found in this sample. This was because the greatest enhancement in MB absorbance occurred at a much lower dye loading for the pure Au colloid compared with any other colloid examined. By accounting for the MB/ metal ratio at the point of maximum enhancement in MB absorbance a trend was revealed where the metal–dye interactions were strongest at the pure Au and Ag ends of the series and minimised in the middle of the series at the Au 50%: Ag 50% sample. Overall, this demonstrated that the interactions of MB dye with the pure Au sample yielded the most effective metal-dye charge transfer. Recent studies of Au-Ag core-shell particles by Maenosono *et. al.* show that the greatest degree of electron transfer occurs from the Au core to the Ag shell.[206–208] As such, we expect our Ag-Au core-shell particles to behave in a similar manner, and push electronic charge towards the core and thus reduce metal-dye charge transfer.

When the average nanoparticle surface area of each colloid (calculated using the average particle diameter determined from TEM imaging) and the number of MB molecules that would surround each particle were taken into account, a linear trend was observed ($r^2 = 0.99$). This relationship showed how important a high particle surface area is for achieving a high increase in the extinction coefficient of interacting MB dye.

There are several ways in which a MB dye molecule can interact with a nanoparticle in solution. If the two extreme cases are considered, the approximate number of MB coordination shells that surround each particle can be estimated from the titration results. This is assuming:

(i) The nanoparticles do not aggregate during the titration
(ii) Each MB dye molecule was interacting with a single nanoparticle (not forming bridged interactions between two or more nanoparticles)
(iii) Using the average nanoparticle size as a model would give an accurate depiction of conditions throughout the colloid.

Colloidal aggregation leads to the rapid loss of SPR properties and particles falling out of solution, typically as a fine black powder that forms at the basin. Additionally, if a large proportion of MB dye molecules formed bridging interactions between particles then aggregation would be encouraged. As aggregation was not observed in any of the titrations performed, assumptions (i) and (ii) were fair. Given the solutions were quite monodisperse (Table 5.3.4.1), assumption (iii) was also fair.

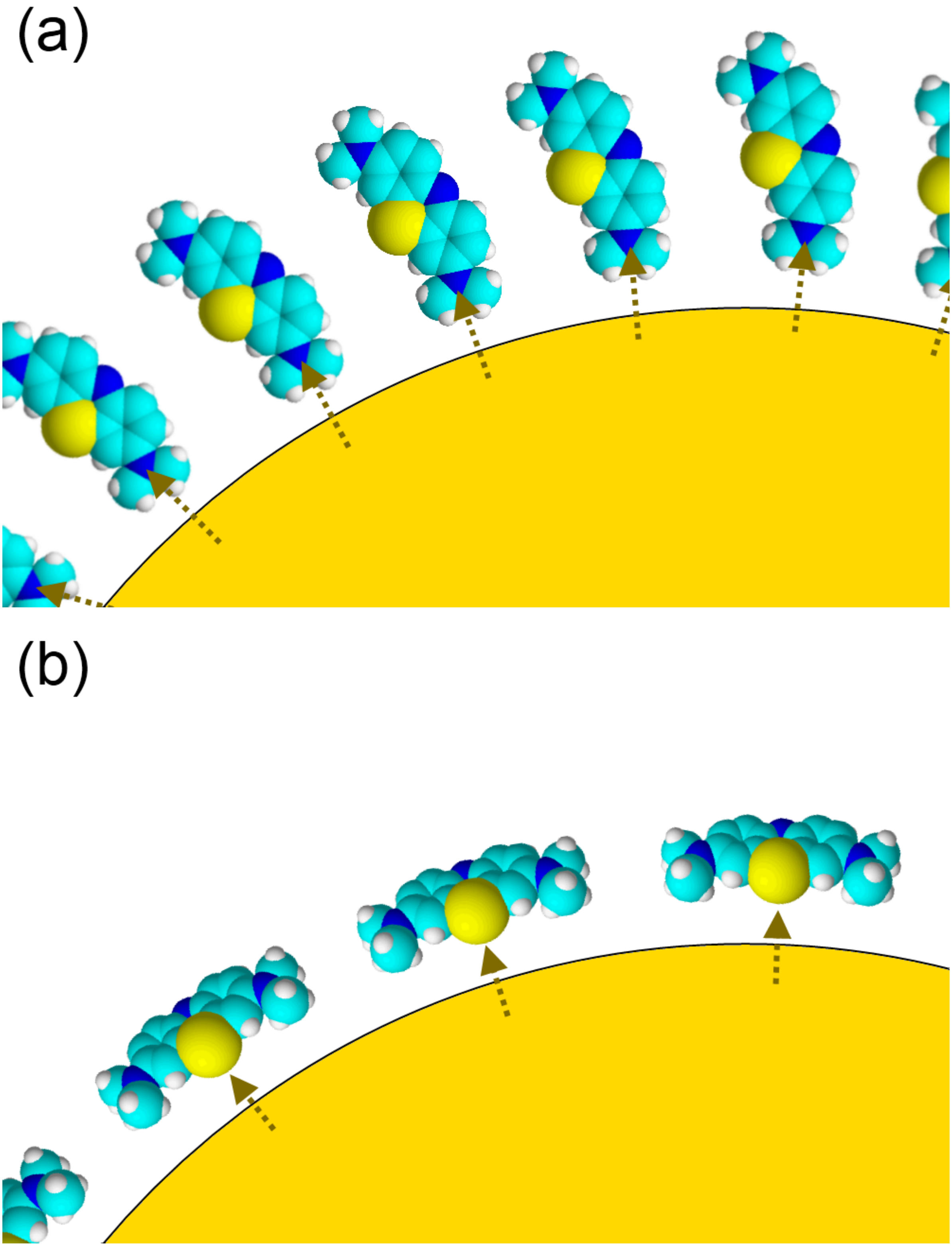

Figure 5.3.4.9: Diagrams depicting the interaction of MB molecules with a nanoparticle surface. The two extreme cases of (a) upward stacking and (b) flat stacking were considered for determining the number of MB shells that surrounded each particle in the colloids examined.

The two cases that we considered are the highest and lowest modes of surface coverage, namely, where the MB dye molecule lies completely flat compared to the nanoparticle plane (maximum area is 89.5 Å^2) or points up by means of an interaction of a side amine group to the plane (minimum area is 7.1 Å^2). A diagram depicting each interaction is shown in Figure 5.3.4.9. In making these two assumptions the average number of coordination shells that surrounded each nanoparticle in the pure gold sample (Au 100 %) was 0.4 for the case of upward MB stacking (Figure 5.3.4.9 (a)) and 5 for the case of flat MB stacking (Figure 5.3.4.9 (b)). As it was not known which mode of MB interaction was prominent, be it the flat or upward stacking case, it was presumed that the number of MB shells surrounding each gold particle at the optimum was somewhere between 0.43 and 5.1 shells. The upward stacking case for samples Ag 100 % and Au 50%: Ag 50% showed 0.95 and 1.4 shells respectively. The flat stacking case for samples Ag 100 % and Au 50%: Ag 50% showed 11.2 and 16.7 shells respectively. Comparing the colloids across the series it was found that larger particles required a larger number of MB solvation shells to reach the point where a maximum increase in the extinction coefficient was observed. A linear trend between these two properties was observed ($r^2 = 0.97$). This could explain why a lower percentage increase in the extinction coefficient was observed in the comparatively larger Ag-Au core-shell colloid, where a poorer “communication” between the metal and the dye resulted due to the greater average distance between each MB molecule and the surface of the interacting particle.

Although the pure Au colloid showed the greatest metal–dye interactions, one might attribute it to the larger overall surface area of the sites available for interaction. This meant that a greater amount of surface active sites would be available in the pure Au colloid compared with other colloids formed in this study, thus better accommodating dye absorption at closer distances on average. For example, when Hyett *et. al.* titrated MB dye with smaller gold colloids (12 ± 1 nm in diameter) of equivalent concentration an approximately 550 % increase in the extinction coefficient was observed; a more than double increase compared with this study.[179] However, the total nanoparticle surface area available in 20 mL of a 0.5 mm solution in their gold colloid (170 cm^2) would be almost double the area available in our colloid (90 cm^2). Their maximum extinction coefficient increase occurred at a dye concentration of 2.2 µm. This was approximately half the level of dye compared with the pure Au titration in this study, where the maximum occurred at a concentration of 4.3 µm. By comparing the titration results across both of studies, two relationships become clear:

(i) The larger the particles, the greater the average distance between the particle and the interacting dye is at the optimum (where the greatest increase in the extinction coefficient of the dye is reached and metal–dye interactions are at their maximum)

(ii) The smaller the particles, the lower the MB/metal ratio at the optimum and the greater the increase in the extinction coefficient (as each metal contributes more effectively and the SPR interaction is spread over a lower number of dye molecules).

Within this study, the pure Au and pure Ag colloids showed a marginally greater propensity for increasing the extinction coefficient of MB dye. The near equivalence of the MB dye interactions with the pure Au and Ag colloids were in slight contrast to the height of their plasmon bands, since the plasmon band of Ag was far stronger. It was clear that the effects are in balance as the sample surface area should also be taken into account, where the pure Au colloid had a greater total surface area (89.9 mL) compared with the pure Ag colloid (65.5 mL).

The intensely coloured optical response of the gold and silver metallic/ bimetallic colloids arises from the dielectric field excitations at the surface of the particles. These photo-excitations induce density oscillations, where a collective movement of the electrons gives rise to the intense colour. When the colloid is titrated with cationic dyes such as MB, the dye interacts with the particles in the colloid and is absorbed. When the titration is done at high dye concentrations, several shells of dye molecules can cover each nanoparticle and, at high enough loadings, particle agglomeration ensues.

The increase in the MB absorbance has been previously attributed to the transfer of photo-induced plasmons at the nanoparticle surface to the locally surrounding dye molecules.[179] In this study, the Ag-Au core-shell colloids showed the lowest increase in the extinction coefficient when titrated with MB dye. It was thus assumed that better transfer of the surface plasmons to the local dye molecules occurred in the pure Au and Ag colloids. The poorer enhancement observed in the core-shell particles was related to: (i) sample surface area and (ii) crystallinity and phase barriers. Across the series, the Au 50%: Ag 50% core-shell sample possessed the lowest total surface area (44.3 mL), which was less than half of the total surface area available in the pure Au colloid (89.9 mL). Of note, the average crystallite size of the pure Au and Ag samples (≈ 13 nm) was higher than the Au 50%: Ag 50% core-shell sample (≈ 10 nm), where electron movement will most likely be hindered in a less crystalline sample. In core-shell samples, the existence of phase-boundaries would further hinder the free movement of electrons within particles. As such, the transfer of the photo-induced dielectric field excitations (*i.e.* SPR) from the core to the surface should, in theory, be more greatly hindered in core-shell materials.

5.3.5. Conclusion

A one-pot modified Turkevich process was used to synthesise a range of colloids from pure Ag, through Ag-Au core-shell structures to pure Au colloids by the thermally activated reduction of auric acid and silver nitrate mixtures by tri-sodium citrate. Non-proportional changes in the SPR band centre indicated that core-shell particles had formed. HRTEM imaging, in conjunction with thin-beam EDX line analysis, confirmed the presence of predominantly Ag cores and Au exteriors in the core-shell particles of Au 50%: Ag 50% formulation. XPS depth profiling supported these results. Two distinct Au (0) and Au(I) environments were observed in the exterior shell, showing that a metallic Ag core was covered by a metallic Au shell partially oxidised at the surface. Titrations of these colloids against methylene blue dye showed strong positive increases in the extinction coefficient at the absorption maximum. We believe that this is the first time that the efficacy of a range of Ag-Au core-shell like particles in enhancing dye colouration has been explored. At the optimum levels of dye addition, a linear relationship between the average nanoparticle size and the number of dye solvation shells was observed. The pure Au and pure Ag particles showed the greatest propensity for an increase in the extinction coefficient of the dye, explained by the better transfer of surface plasmon oscillations of electric charge to the dye molecules localised at their surface.

In the next section we describe the two-stage synthesis of Au-Ag core-shell particles. Gold cores were first formed by the Turkevich method.[77] These gold seeds were then coated with silver shells by heating at reflux in the presence silver nitrate, tri-sodium citrate and ascorbic acid. The concentration of silver nitrate, tri-sodium citrate and ascorbic acid were varied to study their effect on the size/ shape of the silver shell formed. The optical properties and size/ shape of the core-shell particles formed were assessed by UV-visible spectroscopy and TEM respectively. The observed trends were compared with similar syntheses in the literature.

5.4. Two-step synthesis of core-shell gold-silver nanoparticles

5.4.1. Overview

A modification of a simple two-stage synthetic route to primarily spherical Au-Ag core-shell particles is presented. The gold cores were formed in the common way through the Turkevich reduction of auric acid in tri-sodium citrate.[77] The silver coating stage was based upon a modified method first demonstrated by Rodríguez-González *et. al.*[209] This entailed the reflux of the gold cores in a solution containing silver nitrate, tri-sodium citrate (this replaced CTAB in their original synthesis) and ascorbic acid. More interestingly, the effects of altering the concentration of each reagent used in the silver coating stage were studied by UV-visible spectroscopy and TEM. Increasing the level of ascorbic acid led to the progressive increase in the SPR band centre and its absorbance. Moreover, the radius of the encapsulating silver shell increased in size. These observed trends were compared with the original synthesis of Rodríguez-González *et. al.*[209] and other relevant examples in the literature.

5.4.2. Introduction

The *in situ* chemical reduction of auric acid is perhaps the most popular route to the formation of gold nanoparticles. A range of reducing agents including citrate,[77] borohydride,[210] hydrazine,[211] nitric/ hydrochloric acid,[210] dimethyl formamide[212] and ascorbic acid (vitamin C)[213] are commonly used. The latter is frequently used in synthesising complex shapes including nano-rods,[214–216] nano-flowers,[217] nano-tripods,[104] triangular nano-plates[72,125] and can sometimes induce room temperature growth.[218]

A range of Au-Ag core-shell particles have been grown using ascorbic acid. The simple case of primarily spherical Au-Ag core-shell particles was demonstrated by Rodríguez-González *et. al.*[209] Spherical gold seeds (17 ± 3 nm diameter) were prepared by the Turkevich method. The encapsulating silver coating (16 ± 3 nm shell radius) was prepared by sequentially adding CTAB, ascorbic acid, silver nitrate and sodium hydroxide. In another case, micrometre sized bi-metallic meso-flowers were grown by Sajanlal *et. al.* [219] This was achieved by encapsulating pre-formed gold meso-flowers (≈ 2 µm diameter from tip to tip) with a silver layer (≈ 0.5 µm shell radius) by the sequential addition of CTAB, silver nitrate and ascorbic acid and then heating the solution at 80 °C for 1 hr. Bi-metallic Au-Ag core-shell triangular nanoplates were grown by Rai *et. al.*[220] The flat gold triangular nanoplate seeds (≈ 200 ± 100 nm in diameter) were formed from the reaction of auric acid and lemongrass extract. The silver shell (between ≈ 25 – 100 nm shell radius) was then formed by the reaction of silver nitrate and ascorbic acid over a range of pH (7 – 12).[220] Bi-metallic Au-Ag nano-cubes were also achieved by Ma *et. al.*[221] The Au nano-cube seeds (11 ± 1 nm wide) were grown in a two-step process that first involved the reduction of auric acid by borohydride in CTAB and then involved their reduction in additional auric acid with ascorbic acid in cetyltrimethylammonium chloride (CTAC). The silver shell layer was then grown in the presence of silver nitrate, ascorbic acid and CTAC at 60 °C, which could be finely tuned from 1.2 to 20 nm in thickness depending on the silver nitrate concentration. Finally, boat-shaped Au-Ag core-shells were demonstrated by Yang *et. al.* by coating gold nanorods (70 ± 18 nm long and 12 ± 2 nm wide) with a silver layer (4 to 20 nm thick from the "deck" to the "hull") in glycine with CTAB, silver nitrate and ascorbic acid.[222]

In this section we describe the modified synthesis of Au-Ag core-shell particles from a two stage process. First, the gold cores were formed using the Turkevich method.[77] This simply entailed the reflux of auric acid with tri-sodium citrate forming gold nanoparticle seeds. The gold seeds were then coated with silver shells based upon a modified method first demonstrated by Rodríguez-González *et. al.*[209] This was typically achieved by heating the gold seeds at reflux alongside silver nitrate, tri-sodium citrate (replacing the use of CTAB in their original synthesis) and ascorbic acid. The concentration of silver nitrate, tri-sodium citrate and ascorbic acid were varied to study their effect on the size/ shape of the silver shell formed. The optical properties and size/ shape of the core-shell particles formed were assessed by UV-visible spectroscopy and TEM respectively. Primarily spherical core-shell particles were observed with a similarly sized gold core (≈ 15 nm in diameter) and a silver shell that ranged in radius depending on the synthetic conditions applied from 7.1 to 20.5 nm. A trend was observed where increasing levels of ascorbic acid caused progressive increases in SPR band centre and absorbance. Moreover, the radius of the encapsulating silver shell increased when a greater level of ascorbic acid was used. This effect was less pronounced with changes in silver nitrate and tri-sodium citrate concentration. These observed trends were compared with the original synthesis of Rodríguez-González *et. al.*[209]

5.4.3. Experimental

All reagents were purchased form Sigma-Aldrich UK unless otherwise stated. All glassware was cleaned with aqua regia (3HCl: 1HNO_3) and rinsed with copious amounts of deionised water prior to use.

5.4.3.1. Synthesis

Au-Ag core-shell nanoparticles were formed from Au nanoparticle seeds. The Au nanoparticle seeds were first formed by a simple Turkevich method.[77] This required the reflux of auric acid (0.28 mM) and tri-sodium citrate (10 mM) solutions in 20 mL deionised water for 5 mins. The solution changed from a faint yellow solution to a bright red solution, indicating the formation of Au seeds (primarily spherical particles that are 15.4 ± 3.0 nm in diameter). The solution was then allowed to cool to room temperature before the second synthetic stage – the formation of the Ag shell coating. This was achieved in four separate ways for comparison. In each case the solution was heated under reflux for 5 mins, where 2 mL of the Au NP seed solution in 10 mL of deionised water was mixed with:

(i) 2 mL of silver nitrate (0.05 mM) and 2.0 mL of tri-sodium citrate (20 mM),
(ii) 1 mL of silver nitrate (0.05 mM), 2.0 mL of tri-sodium citrate (20 mM) and 0.5 mL of ascorbic acid (0.1 M),
(iii) 4.0 mL of silver nitrate (0.05 mM), 4.0 mL of tri-sodium citrate (20 mM) and 1.0 mL of ascorbic acid (0.1 M) and
(iv) 2.0 mL of silver nitrate (0.05 mM), 2.0 mL of tri-sodium citrate (20 mM) and 2.0 mL of ascorbic acid (0.1 M).

For the purpose of identifying solutions they were labelled Solution: (i) A, (ii) B, (iii) C and (iv) D. The reagents used in forming Solutions A – D are summarised in Table 5.4.3.1.

Table 5.4.3.1: A summary of the concentration and volume of each reagent added in composing Solutions A – D.

Solution	Au NP seed (mL)	deionised water (mL)	silver nitrate 0.05 mM (mL)	tri-sodium citrate 20 mM (mL)	ascorbic acid 0.1 M (mL)	volume (mL)
A	2.0	10	2.0	2.0	0.0	16
B	2.0	10	1.0	2.0	0.5	15.5
C	2.0	10	4.0	4.0	1.0	21.0
D	2.0	10	2.0	2.0	2.0	18.0

Before each solution was refluxed, solutions were pale pink. When the solutions reached boiling point, an almost instantaneous transition from a pale pink to a hazy golden-brown occurred. In the case of Solutions A and D, a deeper brown coloured solution was observed. Solution B was slightly more yellow coloured than the other solutions. Solution C was slightly more orange in colour. The solutions were two-toned, appearing dark brown in reflectance and showing an orange yellow tinge in transmittance. Solutions A – D are displayed in Figure 6.3.1 alongside their original Au NP seed solution.

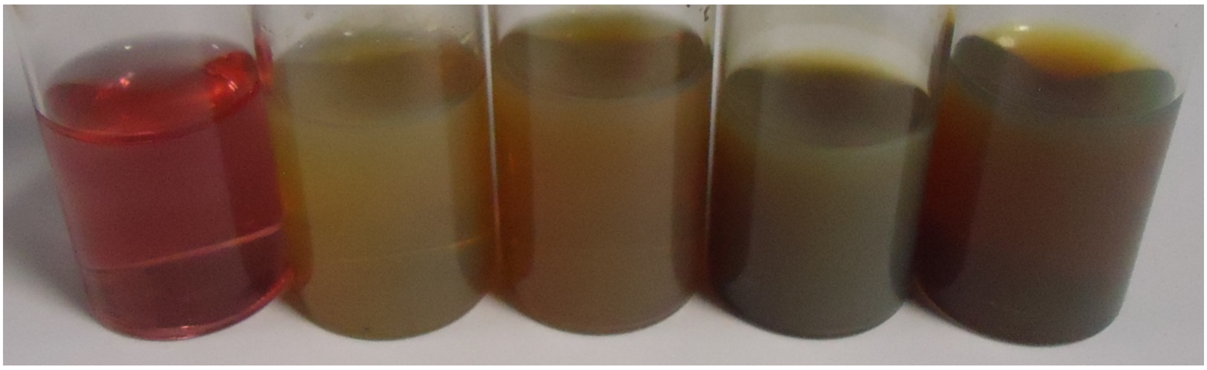

Figure 5.4.3.1: A photograph of the nanoparticle solutions studied in this chapter. From left to right we have the Au NP seed solution and then Solutions A, B, C and D, the Au-Ag core-shells.

5.4.3.2. Analysis

The UV-visible absorption spectra of Solutions A – D were assessed using a PerkinElmer Lambda 25 UV/VIS spectrometer. The digital image was taken using a Kodak C813 digital camera. The size and shape of particle cores and shells were investigated on a Jeol 4000EX HRTEM device. Samples for TEM analysis were prepared by evaporating purified solution droplets onto lacey carbon film coated copper grids.

5.4.4. Results and discussion

Au-Ag core-shell nanoparticle solutions were synthesised in a two step process. First a Au seed was formed from a typical Turkevich style reaction.[77] This involved refluxing solutions of auric acid salt and tri-sodium citrate, which acts as both the reducing agent and particle surfactant for stabilisation of the Au particles that are formed. Next, Ag shell layers were grown around these Au cores in reflux reactions with silver nitrate salt. This was achieved by four different protocols for comparison. Sample A involved the direct reflux with silver nitrate salt and tri-sodium citrate. Samples B - D involved the addition of varying amounts of silver nitrate salt, tri-sodium citrate and ascorbic acid.

The absorption spectrum of each core-shell colloid (diluted by a factor of either 20 or 40) as well as the original Au seed solution was assessed by UV-visible spectroscopy (Figure 5.4.4.1). A UV-visible spectrum typical to the formation of gold nanoparticles was observed in Figure 5.4.4.1(a) for the Au seed solution. The SPR band was centred at 521 nm (abs = 0.73). The UV-visible spectrum of ascorbic acid (0.1 M) was plotted alongside the Au seed solution. This showed an almost flat absorption over the visible range (abs < 0.1). Figure 5.4.4.1(b) shows the stacked UV-visible absorption spectra of Solutions A – D, diluted by either a factor of 20 or 40 as the absorbance of pure solutions saturated the detector. Solutions C and D were deeper in colour and thus diluted by the larger multiple (40). The absorbance data for Solution D was not further altered. Solutions C – A were stacked above Solution D by cumulatively adding 0.1 Absorbance units to each spectrum. Compared with the Au seed solution, much broader SPR bands were observed. These were typically more than 200 nm in width whereas the Au seed SPR band was only ≈ 100 nm wide. The centre of each SPR band was blue shifted relative to the Au seed (λmax = 521 nm). Solution A was the most blue shifted (λmax = 416 nm) and Solution D was the least blue shifted (λmax = 430 nm).

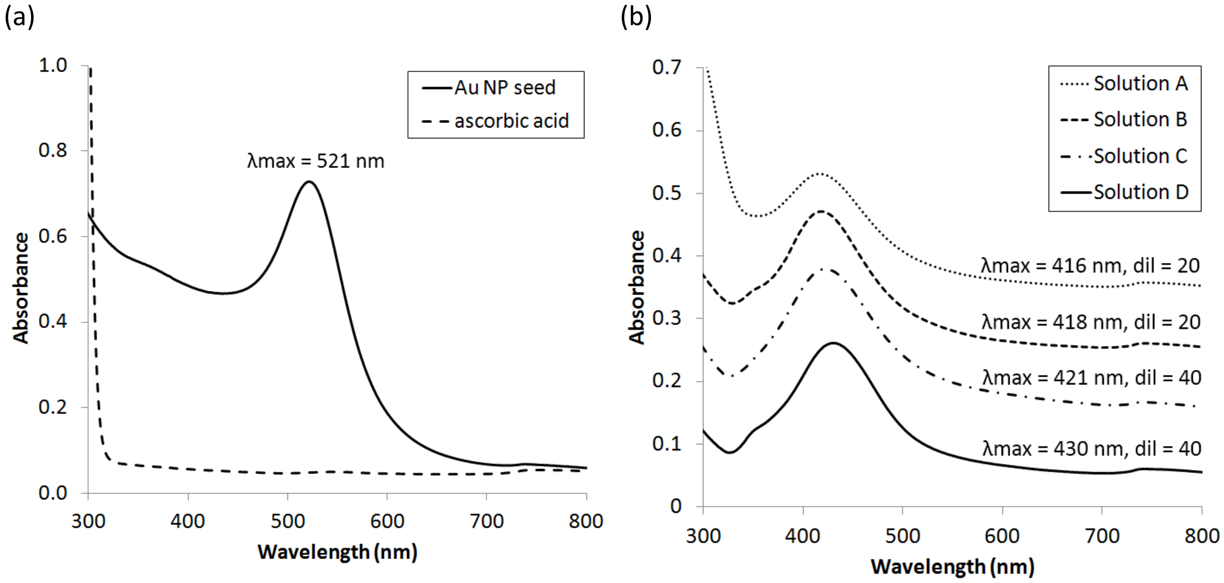

Figure 5.4.4.1: (a) The UV-visible absorption spectrum of an Au seed nanoparticle solution and (b) stacked UV-visible absorption spectra of the Au-Ag core-shell colloids produced from this seed (Solutions A – D); *λmax* represents the centre of each surface plasmon resonance maximum and *dil* represents the multiple of dilution. In Figure (a) the spectrum of ascorbic acid solution (0.1 M) is plotted for comparison.

A trend was observed where a progressive increase in ascorbic acid (0.1 M) caused a lesser shift in the SPR band of the original Au seed solution (Figure 5.4.4.2). It was assumed that these SPR shifts were mainly dependent on the level of ascorbic acid introduced. This was because no rational trend between the level of citric acid or silver nitrate added was observed. It was thus postulated that the SPR band centre could be tailored by controlling the level of ascorbic acid added to the Au NP seed.

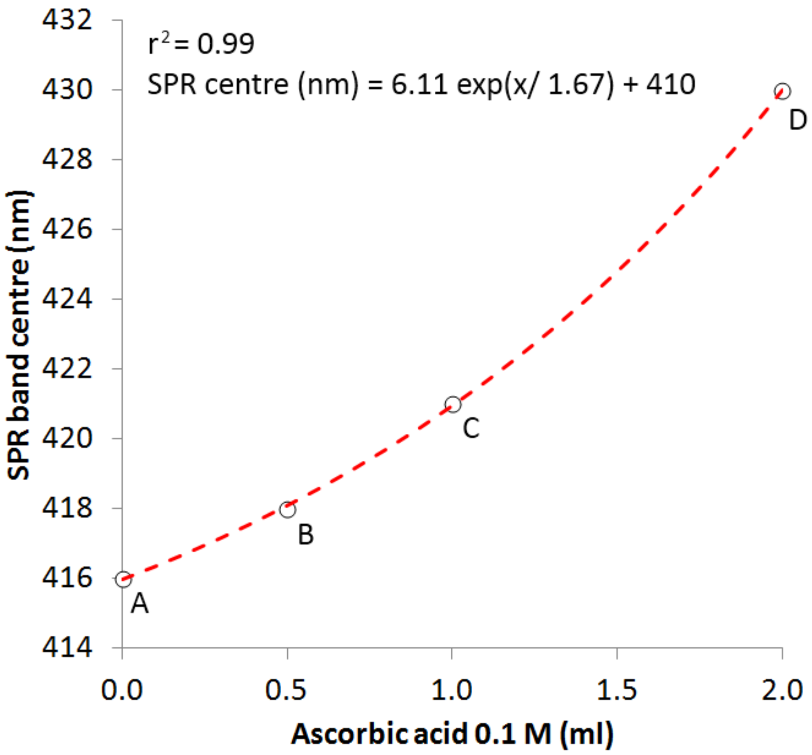

Figure 5.4.4.2: The exponential relationship (r^2 = 0.99) between the resulting SPR band centre (nm) and the original volume of ascorbic acid 0.1 M (mL) added to the Au NP seed solution. The letters A – D denote the Solution label for each data point.

The increase in SPR absorbances in the Au-Ag core-shell nanoparticles formed was not due to the increase in metal content alone. This was because SPR band absorbance increased by at least one order of magnitude. The large increase in SPR band absorbance was attributed to the strong SPR absorbance of silver nanoparticles relative to gold. This was aptly demonstrated by comparing the metal concentrations with the absorbance maxima (Table 5.4.4.1). By deriving the SPR absorbance per metal (mM) for each solution it was demonstrated that the Au seed solution was far less absorbing than the Au-Ag core-shell colloids (Solutions A – D). The absorbance to metal ratio generally increased from Solution A to D. Once again, this was apparently related to the level of ascorbic acid used more so than anything else. In plotting the percentage ascorbic acid introduced (relative to the co-reducing agent tri-sodium citrate) an almost linear relationship was observed. As of yet, how the level of ascorbic acid causes the SPR band to red-shift and increase the SPR absorbance is unclear.

Table 5.4.4.1: The nanoparticle solution metal concentrations of Au and Ag (mM), solution dilution multiples, SPR band centres (nm) and heights (abs), true height (= [1+dil.multiple] x height) and abs/ [metal] ratio (= true height/ total [metal]).

	Metal concentration (mM)		SPR				
Sample	[Au]	[Ag]	dilution multiple	centre (nm)	height (Abs)	true height (abs)	abs/ [metal] ratio
Au seed	0.25	0.00	0	521	0.729	0.729	0.291
Solution A	0.31	6.25	20	416	0.262	5.50	0.837
Solution B	0.32	3.23	20	418	0.232	4.86	1.37
Solution C	0.24	9.52	40	421	0.271	11.1	1.14
Solution D	0.28	5.56	40	430	0.279	11.4	1.96

The size and shape of the Au-Ag core-shell particles formed were probed by TEM (Solutions A – C). The Au seed solution was also analysed for a direct comparison. For further comparison a new solution was formed similar to Solution A but without the secondary addition of tri-sodium citrate (*i.e.* no further reductant was added before the 5 min reflux) and containing only additional silver salt. This solution will be referred to as Solution X. Figure 5.4.4.3(a) shows an image of the Au nanoparticles formed in the seed solution. The particles formed were primarily spherical with some formation of distinct decahedral and tetrahedral shapes. Particle diameters were 15.4 nm on average with a standard deviation of 3.0 nm (15.4 ± 3.0 nm). Interestingly, when no further reducing agent was added to the Au seed and silver salt mixture before reflux (Solution X) some degree of Au-Ag core-shell formation was observed (Figure 5.4.4.3(b)). It was assumed that this process was reliant upon some excess tri-sodium citrate that may have remained with the Au seed solution for this partial reduction process to occur. The reason for assuming only a partial reduction was due to the comparatively “fluffy” nature of the Ag shell formed around the Au core. This indicates the formation of an amorphous and low density shell. When the sizes of the cores and shells were measured an interesting effect was observed. The cores had now increased to 39.2 ± 14.7 nm in diameter and the total encapsulating shell diameters (*i.e.* total nanoparticle diameter including the enclosed core) were 233 ± 48.2 nm (shell radius = 96.7 nm). As the gold salt in the original Au NP seed solution had reacted to completion the increase in the size of the cores in Solution X could only have been due to two phenomena:

(i) a dense Ag shell was formed around the Au seeds which was indistinct from the original seed particle or

(ii) Au: Ag alloyed particles were formed though ingress of Ag particles within the Au NP seeds.

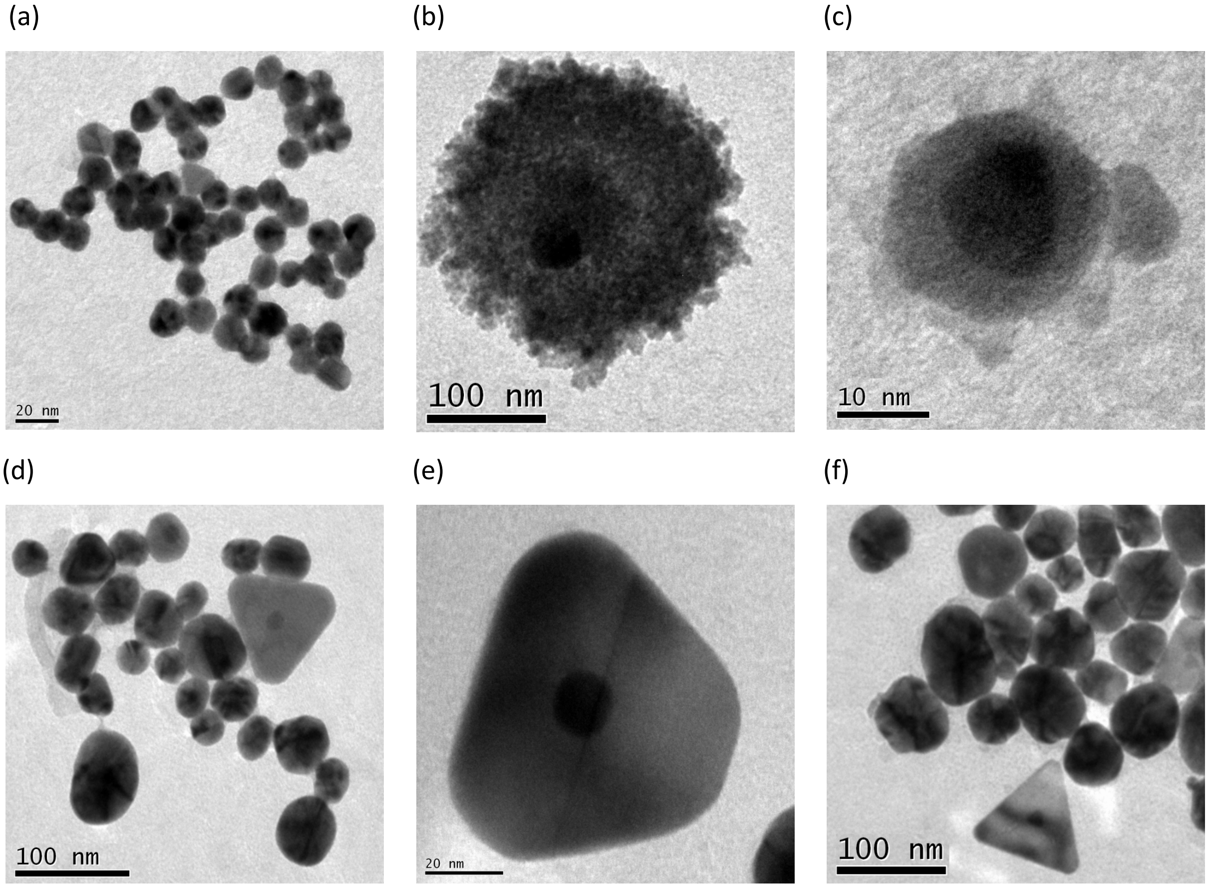

Figure 5.4.4.3: Representative TEM images of (a) Au seed particles and (b-f) the Au-Ag core-shell type structures that are formed upon reaction with $AgNO_3$ salt; (b) is from Solution X – a solution analogous to Solution A but without the addition of tri-sodium citrate, (c) is Solution A, (d) and (e) are from Solution B and (f) is from Solution C.

As previous studies had established the clear differences in TEM image contrast between core and shell layers,[195] phenomenon (i) was unlikely and given the almost analogous crystallographic nature of Au and Ag, phenomenon (ii) was more likely. This is verified by the large number of studies where particulate Au-Ag alloys readily form. Such an effect was not observed in Solution A; the counterpart of Solution X but with the inclusion of tri-sodium citrate. Distinct Ag shells were formed around the Au seeds. An example is shown in Figure 5.4.4.3(c). The size of the Au seeds did not significantly change (average diameter = 16.1 ± 3.2 nm). The Ag shells were lighter in contrast to the Au cores they encapsulated (encapsulation diameter = 30.3 ± 4.2 nm). The average extended radii (*i.e. half* the encapsulating shell diameter minus the core radius) of the outer Ag shells were 7.1 nm – substantially smaller than those observed in Solution X. This was attributed to the higher density of these Ag shells that yielded more compact structures. The Ag shell layers formed in Solutions B (Figure 5.4.4.3(d-e)) and C (Figure 5.4.4.3(f)) were also compact. Nevertheless, they formed significantly larger shell layers than those formed in Solution A; where the encapsulating diameters were 51.8 ± 7.2 nm and 56.0 ± 16 nm for Solutions B and C respectively. In addition, truncated triangular structures appeared (< 10 % in abundance, Figure 5.4.4.3 (e)), a product of the addition of ascorbic acid to the mix. Similar to Solution A, the diameter of the Au cores did not significantly change in relation to the seed (15.5 ± 2.0 nm for Solution B and 15.0 ± 2.8 nm for Solution C).

Table 5.4.4.2: A summary of the Au core and encapsulating Ag shell diameters (nm) [<x> = average and σ = standard deviation], their average volume (10^3 nm^3) and comparative Ag: Au ratio [particle versus original salt ratio].

	Core diameter (nm)		Encapsulating shell diameter (nm)			Volume (10^3 nm^3)		Ag: Au volume ratio	
	<x>	σ	<x>	σ	Extended shell radius	Au	Ag	Shell: Core	$AgNO_3$: $HAuCl_4$
Au seeds	15.4	3.0	-	-	-	1.91	-	0	0
A	16.1	3.2	30.3	4.2	7.1	2.19	12.4	5.7	20.2
B	15.5	2.0	51.8	7.2	18.2	1.93	70.8	36.6	10.1
C	15.0	2.8	56.0	16.0	20.5	1.78	89.9	50.4	39.7

The average diameters of the Au cores and Ag shells observed in Solutions A – C are summarised in Table 5.4.4.2. Information from the Au seed is included for comparison. Across Solutions A –D, the diameter of the Au cores did not significantly change. Small differences in the average core size were most probably due to sampling and measurement errors. On the contrary, the encapsulating Ag shell diameter increased substantially from 30.3 ± 4.2 nm (Solution A) to 56.0 ± 16.0 nm (Solution C). This corresponded to an extended shell radius increase from 7.1 to 20.5 nm. The volume of the Au cores and Ag shells were determined, where shell volume increased from 12.4 x 10^3 in Solution A to 89.9 x 10^3 nm^3 in Solution C. Bulk Au and Ag share an almost equal atoms/ unit area, therefore the Ag: Au ratio could be deduced by simply dividing the volume of the Ag shell by that of the Au core. This increased from 5.7 to 36.6 to 50.4 for Solutions A to B to C respectively. Intriguingly, this did not correspond to the original Ag salt: Au salt ratio before reflux. What we find is that the resulting Ag: Au volume ratio was almost linearly dependent on the ascorbic acid concentration – irrespective of the amount of $AgNO_3$ / tri-sodium citrate added. For instance, Solution B contained twice as much $AgNO_3$ than Solution C, yet Solution C formed Ag shells that were 1.4 times larger in size.

Bi-metallic Au-Ag core-shell particles were previously grown by Rodrigues Gonzalez *et. al.* in a similar manner.[209] Primarily spherical core-shell particles were formed, similar to our studies. Moreover, some particles adopted triangular structures, quite analogous to our own where the central Au core was positioned directly at the centre of the particle. However, some rod-like structures were observed by Rodrigues Gonzalez *et. al.* not akin to any of our Au-Ag core-shell syntheses. In terms of their synthetic procedure, their Au cores were formed from the analogous co-reduction of auric acid by tri-sodium citrate at reflux. Even though their auric acid was slightly more concentrated than ours (0.50 mM *vs* 0.28 mM) the gold nanoparticles that formed were of similar size (17 ± 3 nm in diameter *vs* 15.4 ± 3.0 nm). Their silver coating was formed from the reaction of 20 mL of 50 mM CTAB, 1 mL of 0.1 M ascorbic acid solution, 0.5 mL of 10 mM silver nitrate and 0.1 mL of 1.0 M NaOH alongside 0.5 mL of the original gold colloid. No heat was provided. The silver coating formed was on average 16 ± 3 nm in extended shell radius, similar to Solution B made in our investigation (18.2 nm, Table 5.4.4.2).

Our syntheses showed that a progressive increase in the level of ascorbic acid led to the progressive increase in the radius of the silver shell formed (alongside progressive shifts in the SPR band centre, Table 5.4.4.1). Previous studies by Ma *et. al.* have shown that the silver shell coating of gold particles can be controlled by altering concentration of the silver source.[221] However, Ma *et. al.* did not study the effect of changing the concentration of ascorbic acid

5.4.5. Conclusion

Primarily spherical Au-Ag core-shell particles were formed by a modified two-stage seed-mediated route. Spherical gold cores (15.4 ± 3.0 nm in diameter) were formed by the Turkevich route. The gold seeds were coated with silver shells at reflux using silver nitrate, tri-sodium citrate and ascorbic acid. The effect of changing the concentration of all three reagents used during the silver coating stage was studied. The most striking effect was observed when the ascorbic acid concentration was altered. When the level of ascorbic acid was increased (from 0 to 2.0 mL), the SPR band red-shifted (from 416 to 430 nm) and its absorbance increased (from 5.5 to 11.4 Abs units). Moreover, the radius of the encapsulating silver shell increased in size (from 7.1 to 20.5 nm).

In the next chapter a summary and conclusion of our major findings is provided. A future outlook and some insight as to what further experiments would be of interest to the scientific community are suggested.

6. Thesis summary and conclusions

In this thesis we revisited perhaps the most common method for growing gold nanoparticles, the Turkevich method, and then made experimental modifications to this method as our basis for growing gold nanoparticles in various ways. In making step-wise modifications to the synthesis (*i.e.* reagent concentrations *etc*), we were able to develop a better understanding of how this impacted on the colloid formed. Interestingly, we showed how gold nanoparticles grown by the Turkevich method marginally decreased in size (*i.e.* digestive ripening) over a period of weeks. In removing reaction by-products and excess reagents we were able to prove that this process was not an extended chemical reaction but rather a physical process of re-ordering. Further examination showed that this long term process of particle re-ordering (from days – weeks at room temperature) could be dramatically sped up by thoroughly refluxing the colloid (in a matter of minutes). This finding corroborated with previous studies on the mechanism of gold particle formation from the Turkevich method and shed further light on the re-ordering process. The effect of altering the activation method from the traditional thermal heating method to microwave-assisted heating, ultra-violet light activation or sonication was studied for the same reaction. Interestingly we found clear differences in the aspect ratio and size of the particles formed depending upon the activation method used. We next studied the effect of replacing tri-sodium citrate, the reducing agent traditionally used in the Turkevich method, with various ketones. The gold nanoparticles formed were at least twice as large as those made using tri-sodium citrate and adopted a variety of distinct multi-faceted 3D (including decahedrons, trigonal bipyramids, triangular prisms *etc*) or 2D shapes (triangular/ hexagonal nanoplates). Perhaps most interestingly, reactions with the cyclic ketone cyclohexanone occurred at room temperature forming gold colloids in a matter of minutes. Based on the by-product (2-chlorocyclohexanone; NMR, gas chromatography and FT-IR spectroscopy) and the chemistry ketones with other noble metal salts such as $CuCl_2$ and $Ph_3Bi(V)Cl_2$, we were able to establish a highly plausible reaction mechanism.

Taking the concept of modifying the Turkevich method further, we then demonstrated how silver-gold core-shell particles of various compositions could be grown in a single step. Moreover, we demonstrated that their interactions with the cationic dye, methylene blue, could yield significant enhancements in the extinction coefficient of the dye (≈ 200 % increase). This type of interaction has been attributed to electronic transfer from the nanoparticle to the surface absorbed dye. A relationship was found where smaller particles reached a maximum enhancement at lower dye concentrations. A lower enhancement in the dye's extinction coefficient was observed in Ag-Au core-shell colloids compared with pure Ag or pure Au. These muted enhancements found in core-shell colloids were attributed to a number of potential causes such as lower surface area, crystallinity and the adverse presence of phase boundaries. Finally, we also demonstrated how Au-Ag core-shell particles could be grown in a two-step process using gold "seeds". The effect of ascorbic acid used alongside tri-sodium citrate as a co-reducing agent was studied and found to be critically related to the size of the Ag shell that encapsulates the Au core, where higher concentrations of ascorbic acid produced thicker shells.

6.1. Future outlook and possible experiments

The variety of methods employed in research to grow gold and silver metal nanoparticles is vast. As the industrial need for such noble metal nanoparticles is increasing, new low-cost and environmentally friendly routes should be established. Gaining further insight into how these nanoparticles grow under various experimental conditions is of equal importance. Given the high cost of gold and silver, it is vital for industries that employ their nanoparticle chemistry to keep additional costs low for their future use to remain competitive. Establishing synthetic protocol where the product is well defined (*i.e.* size, shape, SPR properties *etc*) will make it easier for industries to apply protocol best-suited to their commercial application.

In this thesis several methods for growing gold and gold-silver colloids were explored. Perhaps most interesting was the use of the cyclic ketone cyclohexanone in achieving room temperature growth of gold nanoparticles in an aqueous medium. Compared with traditional reducing agents such as tri-sodium citrate (≈ £2.50/ mol), cyclohexanone is cheaper (≈ £0.75/ mol). Compared with the cost of gold (≈ £4,900 / mol) and silver (≈ £40 / mol), the cost of the reducing agent is minimal. Nevertheless, when one considers the fact that typical nanoparticle solutions are of mM concentration, the true cost per litre of 0.3 M product would be ≈ £1.40 for gold and less than 1 p for silver. For cyclohexanone, the true cost-saving measure is in its ability to activate gold nanoparticle growth at room temperature, which is a unique trait compared with traditional reducing agents that often require reflux (*i.e.* an unnecessary heated cost may be avoided). What lets cyclohexanone down is the non-specificity of the particles that form, where various shapes are formed of differing size. Most industrial applications require nanoparticles of a specific shape and narrow size-range to function in a given product (*e.g.* pregnancy test kits).

We believe that the systematic study of a range of ketones might lead to analogous room temperature chemistry and perhaps yield monodisperse colloids. Our studies thus far indicate that a low pK_e for enolisation is vital for reactions with ketones to occur at room temperature. As such, we believe aldehydes, given their relatively higher acidity and propensity to enolise compared with ketones may be better suited candidates. For instance ethanal (pK_e = 6.23), phenyl acetaldehyde (pK_e = 3.07 for the non-sterically hindered E isomer) and 2-indanone (pK_e = 3.84) are all examples that possess pK_e values far lower than cyclohexanone (pK_e = 6.38). Further considering the problem of multi-shape/ size growth often seen with ketone reducing agents (seen in all our studies herein and in the literature), one should also look to create more monodisperse colloids that are better suited to current industrial applications. We therefore suggest the systematic study of co-reducing agents (such as tri-sodium citrate, ascorbic acid *etc*) or size constricting agents (such as cetyl trimethylammonium bromide, polyethylene glycol *etc*) to be used alongside low temperature activating ketones (such as cyclohexanone).

7. References

(1) Yong, K.-T.; Swihart, M. T.; Ding, H.; Prasad, P. N. *Plasmonics* **2009**, *4*, 79.

(2) Murphy, C. J.; Gole, A. M.; Stone, J. W.; Sisco, P. N.; Alkilany, A. M.; Goldsmith, E. C.; Baxter, S. C. *Acc. Chem. Res.* **2008**, *41*, 1721.

(3) Clearblue. http://www.clearblue.com/uk/clearblue-pregnancy-test.php (accessed Jun 22, 2014).

(4) Qian, X.-M.; Nie, S. M. *Chem. Soc. Rev.* **2008**, *37*, 912.

(5) Lee, K.-S.; El-Sayed, M. A. *J. Phys. Chem. B* **2006**, *110*, 19220.

(6) Jain, P. K.; El-Sayed, I. H.; El-Sayed, M. A. *Nano Today* **2007**, *2*, 18.

(7) Min, B. K.; Friend, C. M. *Chem. Rev.* **2007**, *107*, 2709.

(8) Wang, A.-Q.; Chang, C.-M.; Mou, C.-Y. *J. Phys. Chem. B* **2005**, *109*, 18860.

(9) Thompson, D. T. *Nano Today* **2007**, *2*, 40.

(10) Kim, W. B.; Rodriguez-Rivera, G. L.; Evans, S. T.; Voitl, T.; Einspahr, J. J.; Voyles, P. M.; Dumesic, J. A. *J. Catal.* **2005**, *235*, 327.

(11) Hughes, M. D.; Xu, Y.-J.; Jenkins, P.; McMorn, P.; Landon, P.; Enache, D. I.; Carley, A. F.; Attard, G. A.; Hutchings, G. J.; King, F.; Stitt, E. H.; Johnston, P.; Griffin, K.; Kiely, C. J. *Nature* **2005**, *437*, 1132.

(12) Palgrave, R. G.; Parkin, I. P. *J. Am. Chem. Soc.* **2006**, *128*, 1587.

(13) Walters, G.; Parkin, I. P. *J. Mater. Chem.* **2009**, *19*, 574.

(14) Kafizas, A.; Kellici, S.; Darr, J. A.; Parkin, I. P. *J. Photochem. Photobiol. A Chem.* **2009**, *204*, 183.

(15) Gil-Tomas, J.; Tubby, S.; Parkin, I. P.; Narband, N.; Dekker, L.; Nair, S. P.; Wilson, M.; Street, C. *J. Mater. Chem.* **2007**, *17*, 3739.

(16) Nath, S.; Kaittanist, C.; Tinkharn, A.; Perez, J. M. *Anal. Chem.* **2008**, *80*, 1033.

(17) Perni, S.; Piccirillo, C.; Pratten, J.; Prokopovich, P.; Chrzanowski, W.; Parkin, I. P.; Wilson, M. *Biomaterials* **2009**, *30*, 89.

(18) Paciotti, G. F.; Kingston, D. G. I.; Tamarkin, L. *Drug Dev. Res.* **2006**, *67*, 47.

(19) Schofield, C. L.; Field, R. A.; Russell, D. A. *Anal. Chem.* **2007**, *79*, 1356.

(20) Naja, G.; Bouvrette, P.; Hrapovic, S.; Luong, J. H. T. *Analyst* **2007**, *132*, 679.

(21) Chen, L.-M.; Liu, Y.-N. *Appl. Mater. Interfaces* **2011**, *3*, 3091.

(22) Edwards-Jones, V. *Lett. Appl. Microbiol.* **2009**, *49*, 147.

(23) Shrestha, R.; Joshi, D. R.; Gopali, J.; Piya, S. *Nepal J. Sci. Technol.* **2010**, *10*, 189.

(24) Chopra, I. *J. Antimicrob. Chemother.* **2007**, *59*, 587.

(25) Sung, J. H.; Ji, J. H.; Park, J. D.; Yoon, J. U.; Kim, D. S.; Jeon, K. S.; Song, M. Y.; Jeong, J.; Han, B. S.; Han, J. H.; Chung, Y. H.; Chang, H. K.; Lee, J. H.; Cho, M. H.; Kelman, B. J.; Yu, I. J. *Toxicol. Sci.* **2009**, *108*, 452.

(26) SilverNano. http://www.samsung.com/my/consumer/learningresources/silvernano/silvernano/refigerator.html (accessed Jun 22, 2014).

(27) Evans, R. A.; Hanley, T. L.; Skidmore, M. A.; Davis, T. P.; Such, G. K.; Yee, L. H.; Ball, G. E.; Lewis, D. A. *Nat. Mater.* **2005**, *4*, 249.

(28) Ohko, Y.; Tatsuma, T.; Fujii, T.; Naoi, K.; Niwa, C.; Kubota, Y.; Fujishima, A. *Nat. Mater.* **2003**, *2*, 29.

(29) Yao, J. N.; Hashimoto, K.; Fujishima, A. *Nature* **1992**, *355*, 624.

(30) Page, K.; Palgrave, R. G.; Parkin, I. P.; Wilson, M.; Savin, S. L. P.; Chadwick, A. V. *J. Mater. Chem.* **2007**, *17*, 95.

(31) El-Brolossy, T. A.; Abdallah, T.; Mohamed, M. B.; Abdallah, S.; Easawi, K.; Negm, S.; Talaat, H. *Eur. Phys. J. Spec. Top.* **2008**, *153*, 361.

(32) Kneipp, K.; Moskovits, M.; Kneipp, H. *Surface-enhanced raman scattering: physics and applications*; Springer, 2006.

(33) Mie, G. *Ann. Phys.* **1908**, *23*, 377.

(34) Papavassiliou, G. C. *Prog. Solid State Chem.* **1979**, *12*, 185.

(35) Link, S.; El-Sayed, M. A. *Int. Rev. Phys. Chem.* **2000**, *19*, 409.

(36) Du, H. *Appl. Opt.* **2004**, *43*, 1951.

(37) Barnett, C. E. *J. Phys. Chem.* **1942**, *46*, 69.

(38) Link, S.; El-Sayed, M. A. *J. Phys. Chem. B* **1999**, *103*, 4212.

(39) Kreibig, U.; Vollmer, M. *Optical Properties of Metal Clusters*; Springer: Berlin, 1995.

(40) Alvarez, M. M.; Khoury, J. T.; Schaaff, T. G.; Shafigullin, M. N.; Vezmar, I.; Whetten, R. L. *J. Phys. Chem. B* **1997**, *101*, 3706.

(41) Nozik, A. J.; Memming, R. *J. Phys. Chem.* **1996**, *100*, 13061.

(42) Henglein, A. *Chem. Rev.* **1989**, *89*, 1861.

(43) Schaaff, T. G.; Knight, G.; Shafigullin, M. N.; Borkman, R. F.; Whetten, R. L. *J. Phys. Chem. B* **1998**, *102*, 10643.

(44) Yong, K.-T.; Sahoo, Y.; Swihart, M. T.; Prasad, P. N. *Colloids Surfaces A Physicochem. Eng. Asp.* **2006**, *290*, 89.

(45) Mott, D.; Lee, J.; Thuy, N. T. B.; Aoki, Y.; Singh, P.; Maenosono, S. *Jpn. J. Appl. Phys.* **2011**, *50*, 065004.

(46) Carotenuto, G. *Appl. Organomet. Chem.* **2001**, *15*, 344.

(47) Pendry, J. *Science (80-.).* **1999**, *285*, 1687.

(48) Tessier, P. M. In *Proceedings of SPIE*; SPIE, 2002; Vol. 4577, p. 53.

(49) Das, P.; Metiu, H. *J. Phys. Chem.* **1985**, *89*, 4680.

(50) Storhoff, J. J.; Elghanian, R.; Mucic, R. C.; Mirkin, C. A.; Letsinger, R. L. *J. Am. Chem. Soc.* **1998**, *120*, 1959.

(51) Douglas, F.; Yañez, R.; Ros, J.; Marín, S.; Escosura-Muñiz, A.; Alegret, S.; Merkoçi, A. *J. Nanoparticle Res.* **2008**, *10*, 97.

(52) Shore, M. S.; Wang, J.; Johnston-Peck, A. C.; Oldenburg, A. L.; Tracy, J. B. *Small* **2011**, *7*, 230.

(53) Banerjee, M.; Sharma, S.; Chattopadhyay, A.; Ghosh, S. S. *Nanoscale* **2011**, *3*, 5120.

(54) IndustryWeek http://www.industryweek.com.

(55) Schmid, G. *Clusters and Colloids : From Theory to Application*; VCH: Weinheim, 1994.

(56) Park, J.-E.; Atobe, M.; Fuchigami, T. *Ultrason. Sonochem.* **2006**, *13*, 237.

(57) Suslick, K. S.; Flannigan, D. J. *Annu. Rev. Phys. Chem.* **2008**, *59*, 659.

(58) Liu, F.-K.; Ker, C.-J.; Chang, Y.-C.; Ko, F.-H.; Chu, T.-C.; Dai, B.-T. *Jpn. J. Appl. Phys.* **2003**, *42*, 4152.

(59) Kundu, S.; Liang, H. *Langmuir* **2008**, *24*, 9668.

(60) Esumi, K.; Suzuki, A.; Aihara, N.; Usui, K.; Torigoe, K. *Langmuir* **1998**, *14*, 3157.

(61) Yang, S.; Zhang, T.; Zhang, L.; Wang, S.; Yang, Z.; Ding, B. *Colloids Surfaces A Physicochem. Eng. Asp.* **2007**, *296*, 37.

(62) Plech, A.; Kotaidis, V.; Siems, A.; Sztucki, M. *Phys. Chem. Chem. Phys.* **2008**, *10*, 3888.

(63) Liu, Y.; Chen, S.; Zhong, L.; Wu, G. *Radiat. Phys. Chem.* **2009**, *78*, 251.

(64) Ortega, M. A.; Rodriguez, L.; Castillo, J.; Piscitelli, V.; Fernandez, A.; Echevarria, L. *J. Opt. A Pure Appl. Opt.* **2008**, *10*, 104024.

(65) Werner, D.; Hashimoto, S.; Tomita, T.; Matsuo, S.; Makita, Y. *J. Phys. Chem. C* **2008**, *112*, 16801.

(66) Reetz, M. T.; Helbig, W. *J. Am. Chem. Soc.* **1994**, *116*, 7401.

(67) Blackborow, J. R.; Yound, D. *Metal Vapor Synthesis*; Springer: New York, 1979.

(68) Provis, J. L.; Vlachos, D. G. *J. Phys. Chem. B* **2006**, *110*, 3098.

(69) Van der Zande, B. M. I.; Böhmer, M. R.; Fokkink, L. G. J.; Schönenberger, C. *J. Phys. Chem. B* **1997**, *101*, 852.

(70) Chang, S.-S.; Lee, C.-L.; Wang, C. R. C. *J. Phys. Chem. B* **1997**, *101*, 6661.

(71) Agnihotri, M.; Joshi, S.; Kumar, A. R.; Zinjarde, S.; Kulkarni, S. *Mater. Lett.* **2009**, *63*, 1231.

(72) Basu, N.; Bhattacharya, R.; Mukherjee, P. *Biomed. Mater.* **2008**, *3*, 034105.

(73) Tai, Y.; Tran, N. T. T.; Tsai, Y.-C.; Fang, J.-Y.; Chang, L.-W. *IET Nanobiotechnology* **2011**, *5*, 52.

(74) Chandran, S. P.; Chaudhary, M.; Pasricha, R.; Ahmad, A.; Sastry, M. *Biotechnol. Prog.* **2006**, *22*, 577.

(75) Brust, M.; Walker, M.; Bethell, D.; Schiffrin, D. J.; Whyman, R. *J. Chem. Soc. Chem. Commun.* **1994**, *7*, 801.

(76) Kimling, J.; Maier, M.; Okenve, B.; Kotaidis, V.; Ballot, H.; Plech, A. *J. Phys. Chem. B* **2006**, *110*, 15700.

(77) Turkevich, J.; Stevenson, P. C.; Hillier, J. *Discuss. Faraday Soc.* **1951**, *11*, 55.

(78) Rodríguez-González, B.; Mulvaney, P.; Liz-Marzán, L. M. *Zeitschrift für Phys. Chemie* **2007**, *221*, 415.

(79) Chow, M. K.; Zukowski, C. F. *J. Colloid Interface Sci.* **1994**, *165*, 97.

(80) Polte, J.; Ahner, T. T.; Delissen, F.; Sokolov, S.; Emmerling, F.; Thünemann, A. F.; Kraehnert, R. *J. Am. Chem. Soc.* **2010**, *132*, 1296.

(81) Polte, J.; Erler, R.; Thünemann, A. F.; Sokolov, S.; Ahner, T. T.; Rademann, K.; Emmerling, F.; Kraehnert, R. *ACS Nano* **2010**, *4*, 1076.

(82) Hendel, T.; Wuithschick, M.; Kettemann, F.; Birnbaum, A.; Rademann, K.; Polte, J. *Anal. Chem.* **2014**, *86*, 11115.

(83) Oriani, R. A. *Acta Metall.* **1964**, *12*, 1399.

(84) Haiss, W.; Thanh, N. T. K.; Aveyard, J.; Fernig, D. G. *Anal. Chem.* **2007**, *79*, 4215.

(85) Liu, X.; Atwater, M.; Wang, J.; Huo, Q. *Colloids Surfaces B Biointerfaces* **2007**, *58*, 3.

(86) Salvati, R.; Logno, A.; Carotenuto, G.; Denicola, S.; Pepe, G.; Nicolais, L.; Barone, A. *Appl. Surf. Sci.* **2005**, *248*, 28.

(87) Hao, W.; Yang, W.; Huang, W.; Zhang, G.; Wu, Q. *Mater. Lett.* **2008**, *62*, 3106.

(88) Tanaka, H. K. M.; McIntire, M.; Castillo-Garza, R. *Microporous Mesoporous Mater.* **2005**, *85*, 374.

(89) Lee, D.; Park, S.; Lee, J.; Hwang, N. *Acta Mater.* **2007**, *55*, 5281.

(90) Prasad, B. L. V.; Stoeva, S. I.; Sorensen, C. M.; Klabunde, K. J. *Langmuir* **2002**, *18*, 7515.

(91) Prasad, B. L. V.; Stoeva, S. I.; Sorensen, C. M.; Klabunde, K. J. *Chem. Mater.* **2003**, *15*, 935.

(92) Stoeva, S. I.; Smetana, A. B.; Sorensen, C. M.; Klabunde, K. J. *J. Colloid Interface Sci.* **2007**, *309*, 94.

(93) Sidhaye, D. S.; Prasad, B. L. V. *New J. Chem.* **2011**, *35*, 755.

(94) Kumar, S.; Gandhi, K. S.; Kumar, R. *Ind. Eng. Chem. Res.* **2007**, *46*, 3128.

(95) Nehl, C. L.; Hafner, J. H. *J. Mater. Chem.* **2008**, *18*, 2415.

(96) Nagata, Y.; Mizukoshi, Y.; Okitsu, K.; Maeda, Y. *Radiat. Res. J.* **1996**, *146*, 333.

(97) Su, C.-H.; Wu, P.-L.; Yeh, C.-S. *J. Phys. Chem. B* **2003**, *107*, 14240.

(98) Bar-Ilan, O.; Albrecht, R. M.; Fako, V. E.; Furgeson, D. Y. *Small* **2009**, *5*, 1897.

(99) Chithrani, B. D.; Ghazani, A. A.; Chan, W. C. W. *Nano Lett.* **2006**, *6*, 662.

(100) Huang, C.; Chiu, P.; Wang, Y.; Chen, W. R.; Meen, T. H. *J. Electrochem. Soc.* **2006**, *153*, D129.

(101) Huang, C.; Wang, Y.; Chiu, P.; Shih, M.; Meen, T. H. *Mater. Lett.* **2006**, *60*, 1896.

(102) Tong, X.; Zhao, Y.; Huang, T.; Liu, H.; Liew, K. Y. *Appl. Surf. Sci.* **2009**, *255*, 9463.

(103) Jena, B. K.; Raj, C. R. *Chem. Mater.* **2008**, *20*, 3546.

(104) Ali Umar, A.; Oyama, M. *Cryst. Growth Des.* **2009**, *9*, 1146.

(105) Wang, C.; Kan, C.; Zhu, J.; Zeng, X.; Wang, X.; Li, H.; Shi, D. *J. Nanomater.* **2010**, *2010*, 1.

(106) Tsuji, M.; Hashimoto, M.; Nishizawa, Y.; Kubokawa, M.; Tsuji, T. *Chem. - A Eur. J.* **2005**, *11*, 440.

(107) Shankar, S. S.; Rai, A.; Ankamwar, B.; Singh, A.; Ahmad, A.; Sastry, M. *Nat. Mater.* **2004**, *3*, 482.

(108) Biswas, S.; Hait, S. K.; Bhattacharya, S. C.; Moulik, S. P. *J. Dispers. Sci. Technol.* **2005**, *25*, 801.

(109) Sarkhosh, L.; Aleali, H.; Karimzadeh, R.; Mansour, N. *Phys. Status Solidi* **2010**, *207*, 2303.

(110) Marin, M. L.; McGilvray, K. L.; Scaiano, J. C. *J. Am. Chem. Soc.* **2008**, *130*, 16572.

(111) Herschlog, V. *Ind. Eng. Chem. Anal. Ed.* **1941**, *13*, 561.

(112) Haiss, W.; Thanh, N. T. K.; Aveyard, J.; Fernig, D. G. *Anal. Chem.* **2007**, *79*, 4215.

(113) Owen, E. A.; Yates, E. L. *J. Chem. Phys.* **1935**, *3*, 605.

(114) Cederstav, A. K.; Novak, B. M. *J. Am. Chem. Soc.* **1994**, *116*, 4073.

(115) Barton, D. H. R.; Blazejewski, J.-C.; Charpiot, B.; Finet, J.-P.; Motherwell, W. B.; Papoula, M. T. B.; Stanforth, S. P. *J. Chem. Soc. Perkin Trans. 1* **1985**, 2667.

(116) Kochi, J. K. *J. Am. Chem. Soc.* **1955**, *77*, 5274.

(117) Gammons, C. H.; Yu, Y.; Williams-Jones, A. E. *Geochim. Cosmochim. Acta* **1997**, *61*, 1971.

(118) Keeffe, J. R.; Kresge, A. J.; Scbepp, N. P. *J. Am. Chem. Soc.* **1990**, *112*, 4862.

(119) Karelson, M.; Maran, U.; Katritzky, A. R. *Tetrahedraon* **1996**, *52*, 11325.

(120) Delchev, V. B.; Mikosch, H.; St Nikolov, G. *Monatshefte Fur Chemie* **2001**, *348*, 339.

(121) Chiang, Y.; Hojatti, M.; Keeffe, J. R.; Kresge, A. J.; Schepp, N. P.; Wirz, J. *J. Am. Chem. Soc.* **1987**, *109*, 4000.

(122) Chiang, Y.; Kresge, A. J.; Walsh, P. A.; Yin, Y. *J. Chem. Soc. Chem. Commun.* **1989**, 869.

(123) Keeffe, J. R.; Kresge, A. J.; Yin, Y. *J. Am. Chem. Soc.* **1988**, *110*, 8201.

(124) Chiang, Y.; Kresge, A. J.; Schepp, N. P. *J. Am. Chem. Soc.* **1989**, *111*, 3977.

(125) Ali Umar, A.; Oyama, M.; Mat Salleh, M.; Yeop Majlis, B. *Cryst. Growth Des.* **2010**, *10*, 3694.

(126) Rodriguez-Lopez, J. L.; Montejano-Carrizales, J. M.; Pal, U.; Sanchez-Ramirez, J. F.; Troiani, H. E.; Garcia, D.; Miki-Yoshida, M.; Jose-Yacaman, M. *Phys. Rev. Lett.* **2004**, *92*, 196102/1.

(127) Sanchez-Ramirez, J. F.; Perez, J. L. J.; Orea, A. C.; Fuentes, R. G.; Bautista-Hernandez, A.; Pal, U. *J. Nanosci. Nanotechnol.* **2006**, *6*, 685.

(128) Esparza, R.; Rosas, G.; Lopez Fuentes, M.; Sanchez-Ramirez, J. F.; Pal, U.; Ascencio, J. A.; Perez, R. *Mater. Charact.* **2007**, *58*, 694.

(129) Ye, H.; Crooks, R. M. *J. Am. Chem. Soc.* **2007**, *129*, 3627.

(130) Nutt, M. O.; Heck, K. N.; Alvarez, P.; Wong, M. S. *Appl. Catal. B Environ.* **2006**, *69*, 115.

(131) Hernandez-Fernandez, P.; Rojas, S.; Ocon, P.; Gomez de la Fuente, J. L.; San Fabian, J.; Sanza, J.; Pena, M. A.; Garcia-Garcia, F. J.; Terreros, P.; Fierro, J. L. G. *J. Phys. Chem. C* **2007**, *111*, 2913.

(132) Liu, J.-H.; Wang, A.-Q.; Chi, Y.-S.; Lin, H.-P.; Mou, C.-Y. *J. Phys. Chem. B* **2005**, *109*, 40.

(133) Sharma, A. K.; Gupta, B. D. *Nanotechnology* **2006**, *17*, 124.

(134) Ishii, T.; Otsuka, H.; Kataoka, K.; Nagasaki, Y. *Langmuir* **2004**, *20*, 561.

(135) Sarkar, A.; Kapoor, S.; Mukherjee, T. *J. Phys. Chem. B* **2005**, *109*, 7698.

(136) Burda, C.; Chen, X.; Narayanan, R.; El-Sayed, M. A. *Chem. Rev.* **2005**, *105*, 1025.

(137) Zynio, S. A.; Samoylov, A. V.; Surovtseva, E. R.; Mirsky, V. M.; Shirshov, Y. M. *Sensors* **2002**, *2*, 62.

(138) Daniel, M.-C.; Astruc, D. *Chem. Rev.* **2004**, *104*, 293.

(139) Scott, R. W. J.; Wilson, O. M.; Oh, S.-K.; Kenik, E. A.; Crooks, R. M. *J. Am. Chem. Soc.* **2004**, *126*, 15583.

(140) Scott, R. W. J.; Datye, A. K.; Crooks, R. M. *J. Am. Chem. Soc.* **2003**, *125*, 3708.

(141) Esparza, R.; Ascencio, J. A.; Rosas, G.; Ramirez, J. F. S.; Pal, U.; Perez, R. *J. Nanosci. Nanotechnol.* **2005**, *5*, 641.

(142) Wang, A.-Q.; Liu, J.-H.; Lin, S. D.; Lin, T.-S.; Mou, C.-Y. *J. Catal.* **2005**, *233*, 186.

(143) Molenbroek, A. M.; Haukka, S.; Clausen, B. S. *J. Phys. Chem. B* **1998**, *102*, 10680.

(144) Basnayake, R.; Li, Z.; Katar, S.; Zhou, W.; Rivera, H.; Smotkin, E. S.; Casadonte Jr., D. J.; Korzeniewski, C. *Langmuir* **2006**, *22*, 10446.

(145) Liz-Marzan, L. M. *Langmuir* **2006**, *22*, 32.

(146) Ferrando, R.; Jellinek, J.; Johnston, R. L. *Chem. Rev.* **2008**, *108*, 845.

(147) Walters, G.; Parkin, I. P. *J. Mater. Chem.* **2009**, *19*, 574.

(148) Nath, S.; Kaittanis, C.; Tinkham, A.; Perez, J. M. *Anal. Chem.* **2008**, *80*, 1033.

(149) Gil-Tomas, J.; Tubby, S.; Parkin, I. P.; Narband, N.; Dekker, L.; Nair, S. P.; Wilson, M.; Street, C. *J. Mater. Chem.* **2007**, *17*, 3739.

(150) Noimark, S.; Dunnill, C. W.; Wilson, M.; Parkin, I. P. *Chem. Soc. Rev.* **2009**, *38*, 3435.

(151) Ahonen, P.; Schiffrin, D. J.; Paprotny, J.; Kontturi, K. *Phys. Chem. Chem. Phys.* **2007**, *9*, 651.

(152) Yu, C.; Nakshatri, H.; Irudayaraj, J. *Nano Lett.* **2007**, *7*, 2300.

(153) Li, M.; Lin, Y.-C.; Wu, C.-C.; Liu, H.-S. *Nucleic Acids Res.* **2005**, *33*, E184/1.

(154) Qian, X.-M.; Nie, S. M. *Chem. Soc. Rev.* **2008**, *37*, 912.

(155) Ferrara, M. C.; Mirenghi, L.; Mevoli, A.; Tapfer, L. *Nanotechnology* **2008**, *19*, 365706/1.

(156) Armelao, L.; Barreca, D.; Bottaro, G.; Gasparotto, A.; Maccato, C.; Maragno, C.; Tondello, E.; Lavrencic, S. U.; Bergant, M.; Mahne, D. *Nanotechnology* **2007**, *18*, 375709/1.

(157) Ito, A.; Masumoto, H.; Goto, T. *Mater. Trans.* **2003**, *44*, 1599.

(158) Palgrave, R. G.; Parkin, I. P. *Chem. Mater.* **2007**, *19*, 4630.

(159) Palgrave, R. G.; Parkin, I. P. *Gold Bull.* **2008**, *41*, 66.

(160) Mulvaney, P. *Langmuir* **1996**, *12*, 788.

(161) Davey, W. P. *Philos. Mag.* **1925**, *50*, 311.

(162) Lee, K.-S.; El-Sayed, M. A. *J. Phys. Chem. B* **2006**, *110*, 19220.

(163) Link, S.; Wang, Z. L.; El-Sayed, M. A. *J. Phys. Chem. B* **1999**, *103*, 3529.

(164) Chen, D.-H.; Chen, C.-J. *J. Mater. Chem.* **2002**, *12*, 1557.

(165) Mallin, M. P.; Murphy, C. J. *Nano Lett.* **2002**, *2*, 1235.

(166) Han, H.; Fang, Y.; Li, Z.; Xu, H. *Appl. Phys. Lett.* **2008**, *92*, 023116/1.

(167) Li, Z. Y.; Wilcoxon, J. P.; Yin, F.; Chen, Y.; Palmer, R. E.; Johnston, R. L. *Faraday Discuss.* **2008**, *138*, 363.

(168) Zhang, Q.; Lee, J. Y.; Yang, J.; Boothroyd, C.; Zhang, J. *Nanotechnology* **2007**, *18*, 245605/1.

(169) Karthikeyan, B.; Anija, M.; Philip, R. *Appl. Phys. Lett.* **2006**, *88*, 053104/1.

(170) Chen, Y. H.; Yeh, C. S. *Chem. Commun.* **2001**, 371.

(171) Chen, H. M.; Liu, R. S.; Jang, L.-Y.; Lee, J.-F.; Hu, S. F. *Chem. Phys. Lett.* **2006**, *421*, 118.

(172) Takatani, H.; Kago, H.; Nakanishi, M.; Kobayashi, Y.; Hori, F.; Oshima, R. *Rev. Adv. Mater. Sci.* **2003**, *5*, 232.

(173) Schmidt, A. A.; Anton, R. *Surf. Sci.* **1995**, *322*, 307.

(174) Lu, L.; Wang, H.; Zhou, Y.; Xi, S.; Zhang, H.; Hu, J.; Zhao, B. *Chem. Commun.* **2002**, *2*, 144.

(175) Yang, J.; Lee, J. Y.; Too, H.-P. *Plasmonics* **2006**, *1*, 67.

(176) Glass, A. M.; Liao, P. F.; Bergman, J. G.; Olson, D. H. *Opt. Lett.* **1980**, *5*, 368.

(177) Kometani, N.; Tsubonishi, M.; Fujita, T.; Asami, K.; Yonezawa, Y. *Langmuir* **2001**, *17*, 578.

(178) Xiao, G.-N.; Man, S.-Q. *Chem. Phys. Lett.* **2007**, *447*, 305.

(179) Narband, N.; Uppal, M. A.; Dunnill, C. W.; Hyett, G.; Wilson, M.; Parkin, I. P. *Phys. Chem. Chem. Phys.* **2009**, *11*, 10513.

(180) Chen, J.; Jiang, J.; Gao, X.; Gong, J.; Shen, G.; Yu, R. *Colloids Surfaces, A Physicochem. Eng. Asp.* **2007**, *294*, 80.

(181) Perni, S.; Piccirillo, C.; Pratten, J.; Prokopovich, P.; Chrzanowski, W.; Parkin, I. P.; Wilson, M. *Biomaterials* **2008**, *30*, 89.

(182) Bertolini, G.; Lauro, F. M.; Cortella, G.; Merchat, M. *Biochim. Biophys. Acta* **2000**, *169*, 1475.

(183) Jori, G.; Fabris, C.; Soncin, M.; Ferro, S.; Coppellotti, O.; Dei, D.; Fantetti, L.; Chiti, G.; Roncucci, G. *Lasers Surg. Med.* **2006**, *38*, 468.

(184) Perni, S.; Piccirillo, C.; Kafizas, A.; Uppal, M. A.; Pratten, J.; Wilson, M.; Parkin, I. P. *J. Clust. Sci.* **2010**, *21*, 427.

(185) Casa Software Ltd http://www.casaxps.com/ (accessed Feb 8, 2011).

(186) Briggs, D.; Seah, M. P. *Practical Surface Analysis by Auger and X-ray Photoelectron Spectroscopy*; 2nd editio.; John Wiley and Sons: Chichester, 1992.

(187) Rietveld, H. M. *J. Appl. Crystallogr.* **1969**, *2*, 65.

(188) Toby, B. H. *J. Appl. Crystallogr.* **2001**, *34*, 210.

(189) Prasad, B. L. V.; Stoeva, S. I.; Sorensen, C. M.; Klabunde, K. J. *Langmuir* **2002**, *18*, 7515.

(190) Rodriguez-Gonzalez, B.; Sanchez-Iglesias, A.; Giersig, M.; Liz-Marzan, L. M. *Faraday Discuss.* **2004**, *125*, 133.

(191) Pal, A.; Shah, S.; Devi, S. *Aust. J. Chem.* **2008**, *61*, 66.

(192) Haiss, W.; Thanh, N. T. K.; Aveyard, J.; Fernig, D. G. *Anal. Chem.* **2007**, *79*, 4215.

(193) Patterson, A. *Phys. Rev.* **1939**, *56*, 978.

(194) Vegard, L. *Zeitschrift für Phys.* **1921**, *5*, 17.

(195) Srnova-Sloufova, I.; Lednicky, F.; Germperle, A.; Gemperlova, J. *Langmuir* **2000**, *16*, 9928.

(196) Brust, M.; Walker, M.; Bethell, D.; Schiffrin, D. J.; Whyman, R. *J. Chem. Soc.* **1994**, *7*, 801.

(197) Sajanlal, P. R.; Pradeep, T. *Langmuir* **2010**, *26*, 8901.

(198) Wagner, C. D.; Zatko, D. A.; Raymond, R. H. *J. Anal. Chem.* **1980**, *52*, 1445.

(199) Schoen, G. *Acta Chem. Scand.* **1973**, *27*, 2623.

(200) Fuggle, J. C.; Kallne, E.; Watson, L. M.; Fabian, D. J. *Phys. Rev. B* **1977**, *16*, 750.

(201) Kitagawa, H.; Kojima, N.; Nakajima, T. *Dalt. Trans.* **1991**, 3121.

(202) Pande, S. K.; Ghosh, S.; Praharaj, S.; Panigrahi, S.; Basu, S.; Jana, A.; Pal, T.; Tsukuda. *J. Phys. Chem. C* **2007**, *11*, 10806.

(203) Abid, J.; Girault, H. H.; Brevet, P. F. *Chem. Commun.* **2001**, 829.

(204) Mills, A.; Mcfarlane, M. *Catal. Today* **2007**, *129*, 22.

(205) Bergmann, K.; O'Konski, C. T. *J. Phys. Chem.* **1963**, *67*, 2169.

(206) Maenosono, S.; Lee, J.; Dao, A. T. N.; Mott, D. *Surf. Interface Anal.* **2012**, *44*, 1611.

(207) Nishimura, S.; Dao, A. T. N.; Mott, D.; Ebitani, K.; Maenosono, S. *J. Phys. Chem. C* **2012**, *116*, 4511.

(208) Mott, D. M.; Anh, D. T. N.; Singh, P.; Shankar, C.; Maenosono, S. *Adv. Colloid Interface Sci.* **2012**, *185-186*, 14.

(209) Rodríguez-González, B.; Burrows, A.; Watanabe, M.; Kiely, C. J.; Liz Marzán, L. M. *J. Mater. Chem.* **2005**, *15*, 1755.

(210) Liu, Y.; Male, K. B.; Bouvrette, P.; Luong, J. H. T. *Chem. Mater.* **2003**, *15*, 4172.

(211) Chen, D.-H.; Chen, C.-J. *J. Mater. Chem.* **2002**, *12*, 1557.

(212) Pastoriza-Santos, I.; Liz-Marzán, L. M. *Langmuir* **2002**, *18*, 2888.

(213) Velikov, K. P.; Zegers, G. E.; van Blaaderen, A. *Langmuir* **2003**, *19*, 1384.

(214) Ratto, F.; Matteini, P.; Rossi, F.; Pini, R. *J. Nanoparticle Res.* **2009**, *12*, 2029.

(215) Zhou, Y.-G.; Yang, S.; Qian, Q.-Y.; Xia, X.-H. *Electrochem. commun.* **2009**, *11*, 216.

(216) Park, H. J.; Ah, C. S.; Kim, W.-J.; Choi, I. S.; Lee, K.-P.; Yun, W. S. *J. Vac. Sci. Technol. A Vacuum, Surfaces, Film.* **2006**, *24*, 1323.

(217) Wang, W.; Yang, X.; Cui, H. *J. Phys. Chem. C* **2008**, *112*, 16348.

(218) Medina-Ramirez, I.; Bashir, S.; Luo, Z.; Liu, J. L. *Colloids Surf. B. Biointerfaces* **2009**, *73*, 185.

(219) Sajanlal, P. R.; Pradeep, T. *Langmuir* **2010**, *26*, 8901.

(220) Rai, A.; Chaudhary, M.; Ahmad, A.; Bhargava, S.; Sastry, M. *Mater. Res. Bull.* **2007**, *42*, 1212.

(221) Ma, Y.; Li, W.; Cho, E. C.; Li, Z.; Yu, T.; Zeng, J.; Xie, Z.; Xia, Y. *ACS Nano* **2010**, *4*, 6725.

(222) Yang, Z.; Chang, H.-T. *Nanotechnology* **2006**, *17*, 2304.

8. Appendix

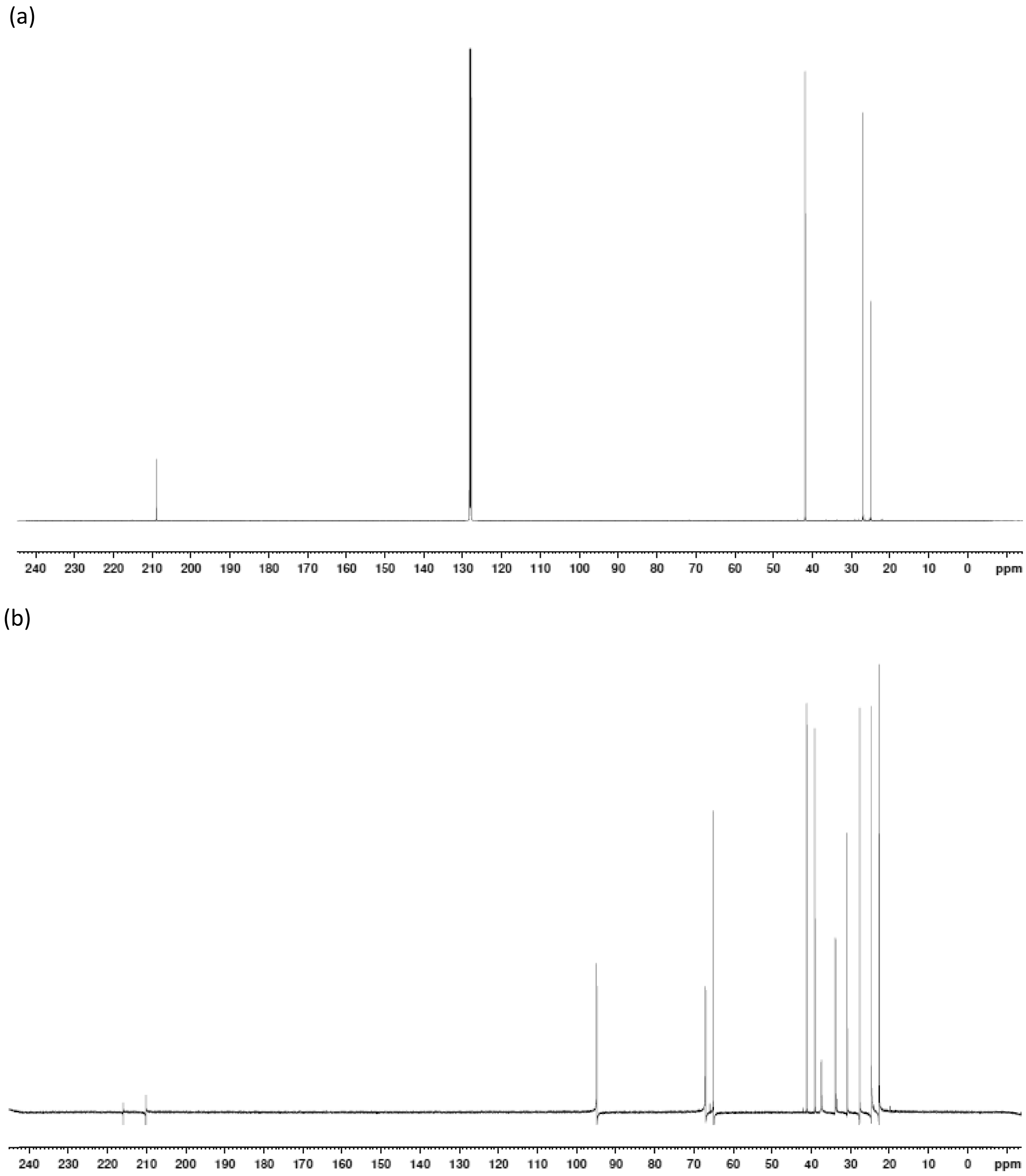

Appendix 1: ^{13}C NMR spectra of pure (a) cyclohexanone and (b) 2-chlorocyclohexanone (600 MHz, D_2O).

(a)

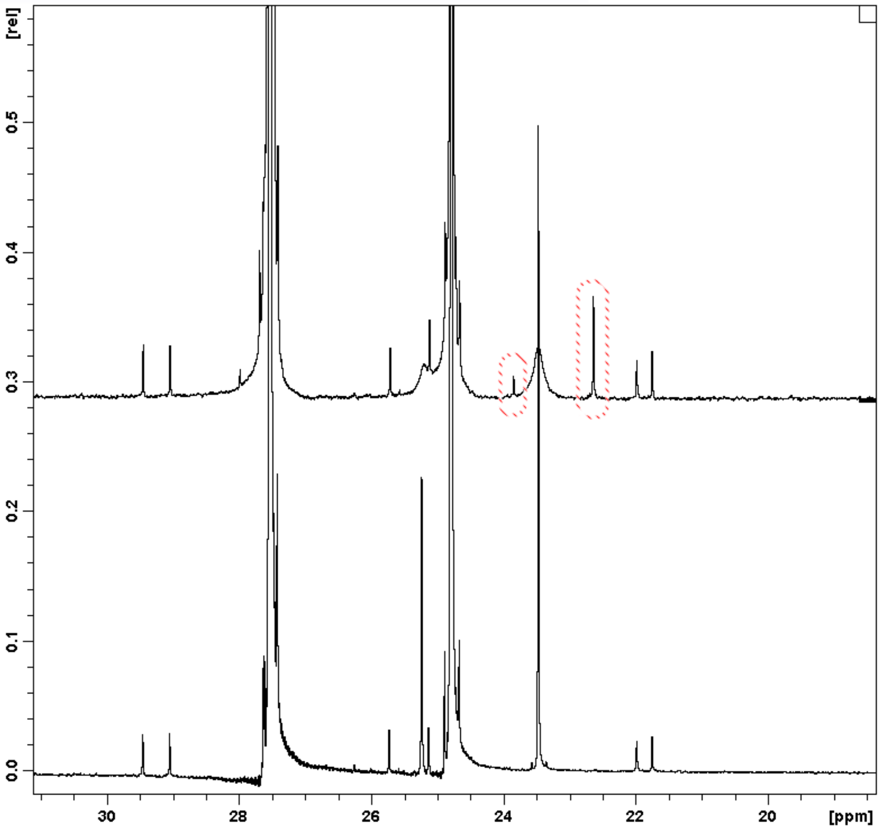
[rel]
0.0
0.1
0.2
0.3
0.4
0.5
30
28
26
24
22
20
[ppm]

(b)

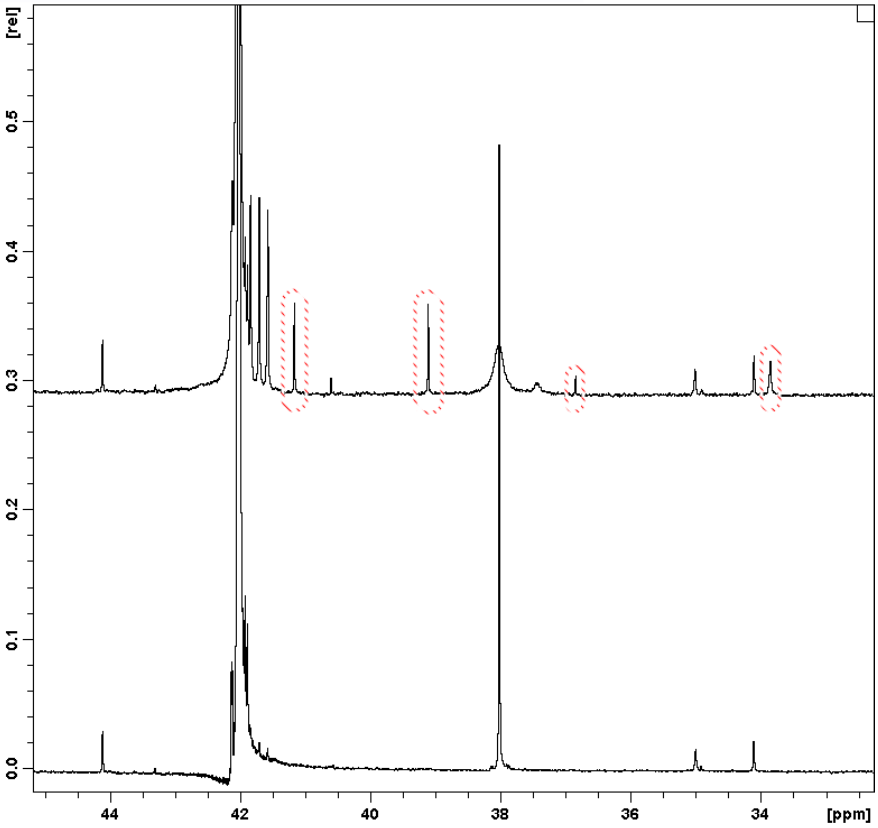
[rel]
0.0
0.1
0.2
0.3
0.4
0.5
44
42
40
38
36
34
[ppm]

(c)

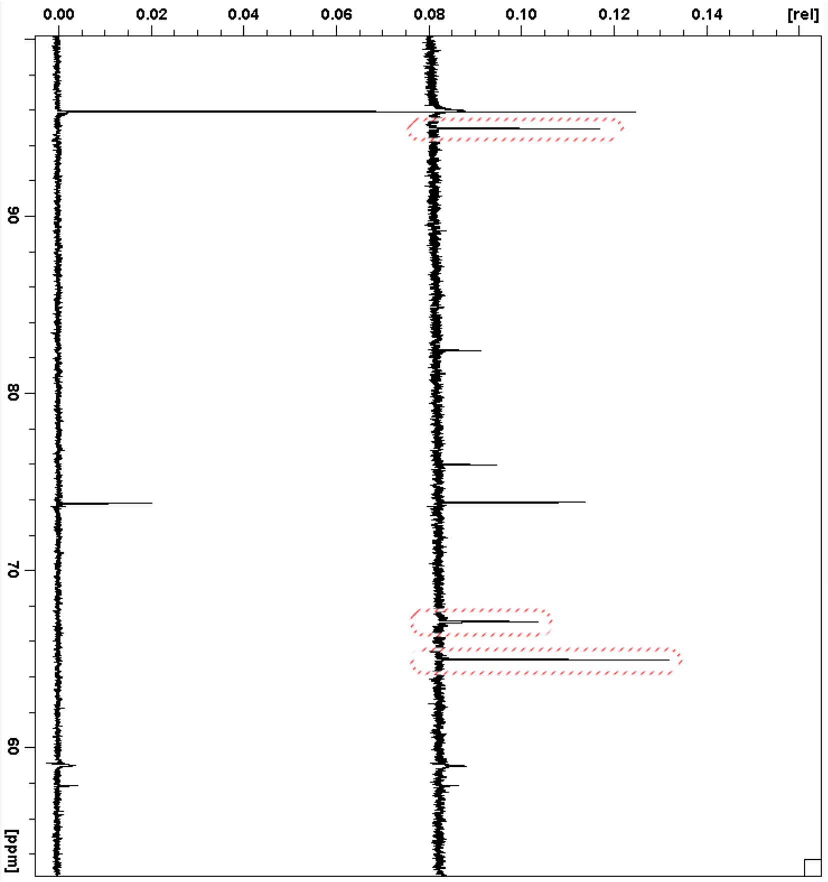

(d)

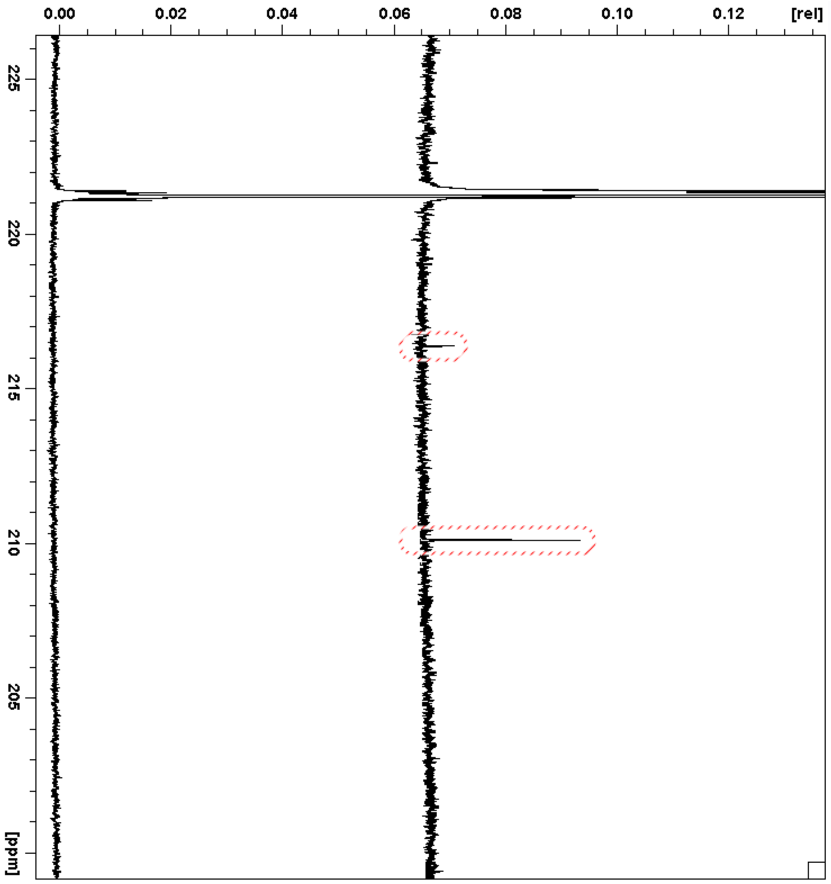

Appendix 2: Zoomed in ^{13}C NMR spectra (600 MHz, D_2O) across four key regions (a) 20 – 30, (b) 34 – 44, (c) 50 – 100 and (d) 200 – 225 δ ppm, where the top spectrum in the series is a gold nanoparticle solution (diluted by a factor of 100) formed from the reaction of auric acid (0.28 mM) and cyclohexanone (0.48 M) in D_2O at room temperature after 1 hr of reaction and the bottom spectrum in the series is cyclohexanone alone in D_2O (0.48 M). The peaks highlighted in dotted red relate were identified as 2-chlorocyclohexanone environments.